Quantum Computing and Information for Nuclear Physics

A Dissertation Presented for the

Doctor of Philosophy

Degree

The University of Tennessee, Knoxville

Chenyi Gu

August 2024

© by Chenyi Gu, 2024
All Rights Reserved.

Acknowledgments

I would like to express my sincere appreciation to my advisor and committee chair, Dr. Thomas Papenbrock, for his invaluable contributions to my research. His mentorship, unwavering support, patience, and the wealth of knowledge and academic experience he shared during my PhD studies have been instrumental in shaping my academic journey. His virtues of diligence, intellectual curiosity, respect, and cheerfulness are a beacon in my career and life.

I am profoundly thankful to my collaborators, Dr. Alessandro Baroni, Dr. Gaute Hagen, Dr. Alessandro Roggero, and Dr. Zhonghao Sun, for insightful discussions and immense help that have significantly enriched my research. I also extend my gratitude to Dr. Lawrence Heilbronn, Dr. Lucas Platter, and Dr. George Siopsis for serving on my PhD committee. I'd like to recognize the valuable help that I received from Dr. Joseph Carlson, Dr. Eugene F. Dumitrescu, and Dr. Titus D. Morris during my visits to National Laboratories.

I would like to express my heartfelt thanks to my office mates, Mohammad Al-Mamum, Jose Bonilla, Evan Combes, Jifeng Fan, Chinmay Mishra, Daniel Odell, and Zichao Yang. Their help and encouragement have been a source of strength and inspiration, and I will always cherish the joyful conversations and the delightful working environment we shared. I would also like to thank all staff members and professors in the Department of Physics and Astronomy for their efforts in making graduate study a pleasant experience.

I want to express my special thanks to my best friends, Runqin Bi and Zhen Gong, for being there for me and cheering me on. Finally, I am heartily grateful to my family for their unconditional love and support. Thank you for encouraging me through the storm and always believing in me. Thank you for being the constant in my life. Love you all!

Abstract

Quantum computation and quantum information, hot topics with immense potential, are making exciting strides in nuclear physics. The computational complexity of nuclear physics problems often surpasses the capabilities of classical computers, but quantum computing offers a promising solution. My research delves into the application of quantum computation and quantum information in nuclear physics.

I am curious about how to approach nuclear physics problems on a quantum computer. This dissertation studies how to prepare quantum states with quantum algorithms, as state preparation is a crucial initial step in studying nuclear dynamics. Two different quantum algorithms are studied: (i) the time-dependent method, which utilizes unitary evolution operator $\exp(-i\gamma\hat{O})$ for a relatively short time to approximate the target operator $\hat{O}$, and (ii) the Linear Combination of Unitaries (LCU) algorithm, which exactly conducts the action of target operator. A toy model for $n(p,d)\gamma$ reaction is studied using both techniques and implemented on simulated and real quantum devices. The results show the practicalness of both algorithms and show the LCU-based method is efficient even with noisy quantum computers nowadays.

Entanglement is viewed as a resource for many quantum processes and is essential for computational speed-up in quantum algorithms. Entanglement measurement and inspection of physics systems are vital. One would expect entanglement entropy to hold an area law (or with logarithmic correction) in lattice systems with local interactions. It is interesting to study if nuclear many-body systems agree with this statement. This dissertation uses the coupled-cluster method to study entanglement entropies between hole space (contains single-particle states below the Fermi level) and particle space (complement to the former) of nuclear many-body systems. The analytical results show that entanglement entropies

are proportional to particle number fluctuation and depletion number of hole space for sufficiently weak interactions, which indicates entanglement entropies in nuclear systems fulfill a volume law instead of an area law. These results are confirmed by computing entanglement entropies of the pairing model and neutron matter.

Keywords: quantum computing and quantum information, state preparation algorithm, many-body nuclear physics, coupled-cluster method, entanglement entropy

Table of Contents

1 Introduction **1**

1.1 Why Quantum Computing in Nuclear Physics? 1

1.2 Mapping Nuclear Physics Problems onto a Quantum Computer 5

1.3 Entanglement of Nuclear Many Body Systems 7

1.4 Scope of This Work and My Contributions 11

2 Excited States Preparation Algorithms for Nuclear Dynamics **13**

2.1 Introduction 13

2.2 Time-dependent Method 16

2.2.1 Fidelities and Success Probabilities Analysis 18

2.2.2 Imperfect Time Evolution 21

2.3 LCU-based Method 25

2.4 Circuit Implementation Details 27

2.4.1 Time-dependent Method 27

2.4.2 LCU-based Method 30

2.5 Results of a Simple Excitation Operator 36

2.5.1 Time-dependent Method 37

2.5.2 LCU-based Method 43

2.6 Results of $n(p,d)\gamma$ Reaction 47

2.6.1 Circuit Implementation Details 50

2.6.2 Results 57

2.7 Summary 60

3 Entanglement Entropy of Nuclear Systems **63**

3.1 Introduction . . . 64

3.1.1 Coupled-cluster Theory . . . 64

3.1.2 Subspace Structure and Entanglement Entropy . . . 70

3.2 Analytical Results Based on the Coupled-cluster Theory . . . 73

3.2.1 Approximate Entanglement Entropies . . . 75

3.2.2 Particle Numbers Fluctuation . . . 78

3.3 Entanglement in Nuclear Systems . . . 80

3.3.1 Pairing Model . . . 80

3.3.2 Neutron Matter . . . 85

3.4 Summary . . . 90

4 Summary and Outlook **94**

Bibliography **96**

Appendices **112**

A Convention of Gates . . . 113

B Error Mitigation . . . 116

Vita **118**

List of Tables

2.1 Quality metrics χ^2 and nssd for success probability P_s with (a) VM simulations and (b) QPU runs for the time-dependent method. The bare results (bare), results with read-out error correction (RO mit.), and results with full error mitigation (full mit.) are shown. 41

2.2 Quality metrics χ^2 and nssd for the transition probability obtained from (a) VM simulations and (b) QPU runs for time-dependent method. The bare results (bare), results with read-out error correction (RO mit.), and full error mitigation (full mit.) are shown. 42

2.3 Quality metrics χ^2 and nssd of the success probability obtained from (a) VM simulations and (b) QPU runs for the LCU-based method. The bare results (bare), results with read-out error correction (RO mit.), and full error mitigation (full mit.) are shown. 45

2.4 Quality metrics χ^2 and nssd of transition probabilities P_t^A and P_t^Bobtained from (a) VM simulations and (b) QPU runs for the LCU-based method. The bare results (bare), results with read-out error correction (RO mit.), and full error mitigation (full mit.) are shown. 46

2.5 Quality metrics χ^2 and nssd of ${}^1S_0 \rightarrow {}^3S_1$ transition probability for thermal neutron-proton using (a) the time-dependent (TD) method and (b) the LCU-based method. The bare results (bare), results with read-out error correction (RO mit.), and full error mitigation (full mit.) are shown. Results were obtained on the Vigo QPU (5qubit backed: IBM Q team, 2020). 59

2.6 Quality metrics χ^2 and nssd of success probability (a) and transition probability (b) for the excitation operator in Eq. (2.6.4) using the LCU-based method on the Vigo QPU 5qubit backed: IBM Q team (2020). The bare results (bare), results with read-out error correction (RO mit.), and full error mitigation (full mit.) are shown. 61

3.1 Numerical values for t^2 for different neutron matter models $N = 14$, 38, 54, 66, 114 with different basis size $N_{\max}$. 91

List of Figures

2.1 Qubits layout and connectivity of the IBM *Quantum* backend Vigo (5qubit backed: IBM Q team, 2020). The circles with number labels are the qubits, and the connection lines represent the connectivity between qubits. The figure is taken from Ref. (Roggero et al., 2020a), which I co-authored. 15

2.2 Estimated success probability P_s in subplot (a) and the allowed value for time steps γ in subplot (b) versus the target infidelity Δ_f. More details of success probability values for small infidelity are shown in the inset of the top panel; note the log scale here. The figure is taken from Ref. (Roggero et al., 2020a), which I co-authored. 20

2.3 Success probability P_s for the time-dependent method versus the parameter θ in excitation operator Eq. (2.5.1) with VM simulations (left panel) and QPU runs (right panel). Results are given with (red squares) and without (black circles) full mitigation and with exact analysis (green lines) from Eq. (2.2.8). The band gives the analyzed bound $9\% \geq P_s(0.3) \geq 8.46\%$. The figure is taken from Ref. (Roggero et al., 2020a), which I co-authored. 39

2.4 Transition probability P_t versus the parameter θ with VM simulations (left panel) and QPU runs (right panel) for the time-dependent method. Results are given with (red squares) and without (black circles) full mitigation and with exact analysis (green lines) from Eq. (2.5.8). The figure is taken from Ref. (Roggero et al., 2020a), which I co-authored. 41

2.5 Success probability P_s versus angle θ in operator Eq. (2.4.18), obtained from VM simulations (left panel) and QPU runs (right panel) for the LCU-based method. Results are given with (red squares) and without (black circles) full mitigation and with exact analysis (green lines) from Eq. (2.3.8). The figure is taken from Ref. (Roggero et al., 2020a), which I co-authored. 45

2.6 Results for the transition probabilities P_t^A (lower panel) and P_t^B (upper panel) versus the angle θ in excitation operator Eq. (2.4.18), obtained from VM simulations (left panel) and QPU runs (right panel) and exact analysis (green lines) for the LCU-based method. The figure is taken from Ref. (Roggero et al., 2020a), which I co-authored. 46

2.7 Success probability (left panel) and transition probability (right panels) for the excitation operator in Eq. (2.6.7) versus the angle θ, using both the time-dependent (TD) method and the LCU-based method. QPU results with [subplot (c)] and without [subplot (b)] error mitigation and with only read-out correction (red empty circles) are given. The figure is taken from Ref. (Roggero et al., 2020a), which I co-authored. 59

2.8 Transition probability P_t (a) and success probability P_s (b) and error of transition probability (c) for thermal neutron-proton capture as a function of angle θ. Results are obtained by using the LCU-based method on the Vigo QPU 5qubit backed: IBM Q team (2020). The figure is taken from Ref. (Roggero et al., 2020a), which I co-authored. 61

3.1 Schematic diagram of nuclear volume (light blue area) and its complement (gray area) for a finite spherical basis in position space. Red and black points represent localized hole and particle states, respectively. The figure is taken from Ref. (Gu et al., 2023), which I co-authored. 74

3.2 Von Neumann entropies S_1 (full markers) and Rényi entropies S_2 (hollow markers) of the reduced hole-space density matrix ρ_{H} versus the particle-number fluctuation $(\Delta N_{\mathrm{H}})^2$ of the hole space for the half-filled pairing model, with $\delta = 1.0$ and different couplings g as indicated. The dash-dotted and dashed lines show analytical results for $\alpha = 1$ and $\alpha = 2$, respectively, and they are valid for values of t^2 as indicated. The color and shape of the markers indicate the coupling strength, and for a given coupling, identical markers show the results for one to twelve pairs. The entropy increases with the number of pairs and with increasing coupling strength. The figure is taken from Ref. (Gu et al., 2023), which I co-authored. 82

3.3 Absolute differences between numerical and analytical Rényi entropies for S_1 (full markers) and S_2 (hollow markers), normalized by the numerical entropy, versus the particle-number fluctuation $(\Delta N_{\mathrm{H}})^2$ of the hole space for the half-filled pairing model, with $\delta = 1.0$ and different couplings g as indicated. The color and shape of the markers indicate the coupling strength, and for a given coupling, identical markers show the results for one to twelve pairs. The figure is taken from Ref. (Gu et al., 2023), which I co-authored. 83

3.4 Relative error of the approximated t^2 value as a function of the number of particles, with $\delta = 1.0$ and $g = 1e-4, 1e-3, 1e-2, 1e-1, 2e-1, 5e-1$. The figure is taken from Ref. (Gu et al., 2023), which I co-authored. 86

3.5 Correlation energy per neutron as a function of the neutron number $N =$ 14, 38, 54, 66, 114 with different basis sizes N_{max}. The figure is taken from Ref. (Gu et al., 2023), which I co-authored. 89

3.6 Entanglement entropy versus the neutron numbers $N = 14$ (triangle_up), $N = 38$ (circle), $N = 54$ (square), $N = 66$ (triangle_left), $N_{\mathrm{max}} = 5$ of momentum space. The figure is taken from Ref. (Gu et al., 2023), which I co-authored. 91

3.7 Entanglement entropy versus the particle number fluctuation with $N = 14$ (triangle up), $N = 38$ (circle), $N = 54$ (square), $N = 66$ (triangle left), $N_{\max} = 5$ of momentum space. The figure is taken from Ref. (Gu et al., 2023), which I co-authored. 92

Chapter 1

Introduction

1.1 Why Quantum Computing in Nuclear Physics?

Complex many-body systems at different energy scales are of interest in many-body nuclear physics, ranging from quark and gluon dynamics at the GeV scale to rotational bands of deformed nuclei at the keV scale. In principle, the starting point for all these rich phenomena can be the fundamental theory of quantum chromodynamics (QCD), while it is hard to exactly solve the Schrödinger equation $\hat{H}\,|\Psi\rangle = E\,|\Psi\rangle$ for a given description of the physics problem. Two challenges are confronted when calculating complex many-body problems using QCD. First, one needs to find out what the Hamiltonian $\hat{H}$ is since describing a nuclear system in terms of quarks and gluons is complex. Second, one needs to find efficient methods to solve the Schrödinger equation since the Hilbert space grows exponentially with an increasing number of nucleons.

The scope of this thesis is focused on the calculations on a low-energy scale, which means the calculations do not consider the details on a higher-energy scale, that one can build Hamiltonian with the help of renormalization group (RG) (Wilson, 1975; Lepage, 1997) ideas and effective field theory (EFT) (Georgi, 1993; Kaplan, 2005). To increase the efficiency of the calculation at low energy, we focus on the relevant degrees of freedom in low-energy many-body physics, construct and truncate Lagrangians at leading order (LO), next-to-leading order (NLO), etc., based on the expansion in Q/Λ with the help of the

power counting scheme introduced by Weinberg (Weinberg, 1979). Q is the energy scale of the system, and Λ is the breakdown scale of EFT.

Provided with the Hamiltonian, the question that arises is how to solve the Schrödinger equation to get the properties of the system. Over the past two decades, tremendous progress has been made in the *ab initio* methods of many-body nuclear theory thanks to the rapid development of computational resources. Ref. (Hergert, 2020) provides a review of *ab initio* nuclear many-body theory; it describes various *ab initio* methods and their applications. Methods like Quantum Monte Carlo (QMC) and full configuration interaction (FCI) can best describe the system with the slightest uncertainty while the Hilbert space grows exponentially with the system size. Methods like Coupled Cluster (CC) and in-medium Similarity Renormalization Group method (IMSRG) scale polynomially.

Despite the fast growth of the *ab initio* calculation methods, it is still a big challenge for today's classical computer to solve many-body nuclear problems. For instance, even though the calculation of heavy nuclei can be pushed to nucleon number $A \sim 140$, there are still huge blanks between magic number nuclei. Nuclei with magic numbers of nucleons $(2, 8, 20, 28, 50, 82, 126)$, or, say, closed-shell nuclei, are easy to describe because there is a relatively large gap between two different shells. Dynamical correlations need to be considered, and the CC method can efficiently solve closed-shell nuclei. However, the vast majority of nuclei are open-shell nuclei, as neither protons nor neutrons have a magic number; they are strongly correlated, and static correlations need to be accounted for. For these problems, we consider using FCI, which carries an expensive computation cost and is most likely to exceed classical computers' abilities. Note here that correlation is the same word as entanglement in the notation of quantum information.

The formal definition of static and dynamic correlations can be found in the paper (Benavides-Riveros et al., 2017). Static correlations usually refer to possible states that are nearly degenerate with the reference states. For example, open shell nuclei do not have well-defined Fermi surfaces, for there are multiple reference states that have similar energies. Dynamic correlations refer to situations where higher-order excited states need to be considered. For example, closed shell nuclei only need a single reference state, for there are relatively large gaps between two shells, and we only need to consider the excited states.

The above statements convey that it is hard to calculate nuclei, especially open-shell nuclei, on classical computers. Also, see the review (Carlson et al., 2022), which demonstrates the exascale computing requirements for diverse nuclear physics topics. The limitation of the classical computer's capability in nuclear physics is one of the reasons why people, including me, explore the computing power of a quantum computer. In 1981, Feynman (Feynman, 1982) proposed the idea of using quantum computers to simulate quantum systems, delivered the famous words: "Let the computer itself be built of quantum mechanical elements which obey quantum mechanical laws." This encourages scientists to study quantum simulators (Johnson et al., 2014), which are used to simulate a quantum system with quantum mechanical systems.

Two approaches of quantum simulators (Buluta and Nori, 2009) are analog quantum simulation and digital quantum simulation. An analog quantum simulator uses the dynamics of a quantum system to resemble the dynamics of another quantum system of interest. A digital quantum simulator (Abrams and Lloyd, 1997) is a gate-based universal quantum computer that translates evolutions in terms of elementary quantum gates implemented on qubits (quantum bits). This dissertation will focus on the gate model quantum computers.

The great power of quantum computers comes from the superposition and entanglement of qubits, which play central roles in quantum computation and allow qubits to encode exponentially more information than classical bits. For example, suppose one wants to simulate a n interacting spin system with the most general and highly entangled state, which can be expressed as

$$|\Psi\rangle = \sum_{i_1=0}^{1} \cdots \sum_{i_n=0}^{1} c_{i_1 \cdots i_n} |i_1\rangle \otimes \cdots \otimes |i_n\rangle \ , \tag{1.1.1}$$

where $|i\rangle$ can be states $|0\rangle$ or $|1\rangle$ in a two-dimensional Hilbert space. To express it, one needs 2^n complex numbers $c_{i_1 \cdots i_n}$ in classical computers and only requires n qubits in quantum computers due to entanglement. Let alone simulating the dynamics of a quantum system. This is one of the evidence shows that quantum computers hold huge potential in simulating nuclear physics problems and outperform the capabilities of classical computers.

The advantages of superposition and entanglement do not mean we can access all the information hidden in the quantum state. Holevo's theorem (Holevo, 1973) gives the upper bound to accessible information: given n qubits, we can only retrieve n classical bits of the information.

The quantum advantage in computation (Preskill, 2012; Bravyi et al., 2018; Maslov et al., 2021; Daley et al., 2022; Herrmann et al., 2023), or quantum computational supremacy (Harrow and Montanaro, 2017; Arute et al., 2019), attracts people to explore efficient quantum algorithms about how quantum states are prepared, evolved, and solved on a quantum computer. Even so, the scope of problems in which one has evidence for the exponential advantage of quantum computing is still a question (Lee et al., 2023). Even though we are now in the Noisy Intermediate-Scale Quantum Era (NISQ) (Preskill, 2018, 2021), we can not efficiently prepare such highly entangled quantum states and evolve complex systems. Noise and the limited number of qubits still limit the size of the quantum circuit and the performance of the near-term quantum processing units. People have optimistic expectations over the utilization of quantum computers in the future and have applied the NISQ quantum computers to nuclear physics (Zhang et al., 2021), quantum computational chemistry (O'Malley et al., 2016; McArdle et al., 2020; Cao et al., 2019; Kowalski and Bauman, 2023), condensed matter physics (Macridin et al., 2018; Backes et al., 2023), and so on (also see the Ref. (Dalzell et al., 2023) about a broader survey of application area).

The topic "quantum computing and simulation for nuclear physics" is a hot one, and many works have been tackled on quantum computers in recent years (Kaplan et al., 2017; Dumitrescu et al., 2018; Klco et al., 2018; Roggero and Carlson, 2019; Shehab et al., 2019; Lu et al., 2019; Holland et al., 2020; Roggero et al., 2020b; Stetcu et al., 2022; Kiss et al., 2022; Pérez-Obiol et al., 2023). This dissertation is about our projects (Roggero et al., 2020a; Gu et al., 2023), which contributed to this topic. Next, I will briefly introduce how to map nuclear physics problems onto a quantum computer.

1.2 Mapping Nuclear Physics Problems onto a Quantum Computer

This dissertation will not go into detail about basic knowledge of quantum computer concepts and quantum algorithms. For the introduction to quantum computation and information, I refer the readers to the textbook by Nielsen and Chuang (Nielsen and Chuang, 2010).

As introduced by Ref. (Deutsch, 1989), 'the universal quantum gate, together with quantum "unit wires", is adequate for constructing networks with any possible quantum computational property.' Since the evolution of quantum systems is unitary, all quantum gates are unitary. As described in Ref. (Deutsch et al., 1995; Barenco et al., 1995), all unitary operations on arbitrarily many bits $n(\mathrm{U}(2^n))$ can be expressed as compositions of elementary operations, and those elementary operations include all one-bit quantum gates ($\mathrm{U}(2)$) and the two-bit exclusive-or gate.

For gate-based quantum computers, the physics systems should be expressed in terms of quantum gates. A series of unitary gates should be applied to a quantum register, a system comprising multiple qubits. Intuitively, the circuit model of a quantum computer resembles that of a classical computer. Similar to a classical computer, there are two states of a qubit, $|\uparrow\rangle$ and $|\downarrow\rangle$ in a two-dimensional Hilbert space. A single qubit state is described as

$$|\phi\rangle = \alpha|\uparrow\rangle + \beta|\downarrow\rangle \ ,$$

where $|\alpha|^2 + |\beta|^2 = 1$, and thought as a spin-1/2 state.

In nuclear physics, physicists usually start with a second-quantized Hamiltonian, written as products of fermionic creation and annihilation operators. Quantum computers require us to map fermionic creation and annihilation operators onto spin lowering and raising operators (Pauli algebra) of qubits. The Jordan-Wigner (Jordan and Wigner, 1928) or Bravyi-Kitaev (Bravyi and Kitaev, 2002) transformations are the most common ones. I refer the readers to the Ref. (Whitfield et al., 2016; Setia et al., 2019; Steudtner and Wehner, 2019; Derby and Klassen, 2020) for other recent mappings.

In nuclear physics, a spin-up (down) state corresponds to an $|0\rangle$ ($|1\rangle$) state. For a chain of spins in one dimension, the Jordan-Wigner mapping is described as,

$$\begin{aligned} f_n^\dagger &\to \frac{1}{2}\left[\prod_{j=0}^{n-1} -Z_j\right](X_n - iY_n) \ , \\ f_n &\to \frac{1}{2}\left[\prod_{j=0}^{n-1} -Z_j\right](X_n + iY_n) \ . \end{aligned} \tag{1.2.1}$$

Here $f_n^\dagger$ and f_n are fermionic creation and annihilation operators for state $|n\rangle$, and X_n, Y_n, Z_n denote the corresponding Pauli matrix acting on qubit n. The phase $\prod_{j=0}^{n-1} -Z_j$ accounts for the number of occupied fermionic modes for modes $j < n$ to satisfy the fermion anti-commutation relations. We have the number operator

$$n_j \equiv f_j^\dagger f_j = \frac{1 - Z_j}{2} \ . \tag{1.2.2}$$

The bilinear operator is expressed as

$$f_q^\dagger f_p + f_p^\dagger f_q = \frac{1}{2}\left[\prod_{j=q+1}^{p-1} -Z_j\right](X_q X_p + Y_q Y_p) \ . \tag{1.2.3}$$

It is assumed that $p > q$. Therefore, the second quantized Hamiltonians can be expressed as the linear combination of Pauli operator strings. For higher dimension spin-fermionic mapping, see Ref. (Fradkin, 1989; Huerta and Zanelli, 1993), and see also Ref. (Ovrum and Hjorth-Jensen, 2007; Coleman, 2015) for detailed Jordan-Wigner mapping for spin $S = 1/2$, Ref. (Batista and Ortiz, 2001) for generalized Jordan-Wigner transformation for arbitrarily spin S.

With these mappings, any unitary evolution can be represented as the products of one and two-qubit operations, and quantum states can be represented as the states of n qubits. After mapping, the simulation procedures are usually separated into three steps: initial state preparation, evolution simulation over the initial states, and measurement via projections. I refer readers to references (Ortiz et al., 2001; Somma et al., 2002) for details of the quantum simulation procedures.

Also, the next Chapter 2, in which I discuss two different algorithms for the excited state preparation and show the detailed transformation of a nuclear physics problem into quantum circuits, can be regarded as a prototypical example of quantum simulation in nuclear physics. It is also an example that shows how to utilize Qiskit (Qiskit contributors, 2023), work with quantum circuits on a quantum device, and apply error correction and mitigation procedures. Error mitigations (Temme et al., 2017; Li and Benjamin, 2017; Endo et al., 2021) are needed to obtain more reliable results since we are in the stage of NISQ.

1.3 Entanglement of Nuclear Many Body Systems

Quantum information science, which is a field that combines quantum mechanics with information theory, ignites the "second quantum revolution" (Dowling and Milburn, 2003; Atzori and Sessoli, 2019; Deutsch, 2020), in which stage the use of quantum physics principles helps people to develop new quantum technologies.

Quantum information science is a vast field; one of the key concepts is entanglement. Entanglement was first recognized by Einstein, Podolsky, and Rosen (EPR) (Einstein et al., 1935) and Schrödinger (Schrödinger, 1935), it describes the phenomenon: the quantum state $|\Psi\rangle$ of a composite system, which can be separated into two subsystems A and B, can not be factored as a product of subsystems' states

$$|\Psi\rangle = |\phi_A\rangle\,|\psi_B\rangle \ ,$$

which implies that even with a complete knowledge of the system, one may not understand its parts. Quantum states described as this are called entangled states or separable states otherwise.

Quantum entanglement (Horodecki et al., 2009) is considered a resource for many quantum processes, such as quantum teleportation and quantum cryptography. Entanglement can help with quantum error correction (Brun et al., 2006), which is essential to fault-tolerant quantum computers.

The power of quantum computation derives from entanglement; it plays an essential role in computational speed-up in quantum algorithms (Ekert and Jozsa, 1998; Jozsa and Linden, 2003). For more information, see Ref. (Jozsa, 2006; Van den Nest et al., 2007), which discusses the range of quantum states and quantum circuits that can be efficiently classically simulated. One needs a sufficient amount of entanglement for this speed-up (Vidal, 2003), and universal quantum computation can be achieved with small entanglement (Van den Nest, 2013). A randomly chosen state, like the state described in Eq. (1.1.1), can be too entangled (Gross et al., 2009; Bremner et al., 2009) to be useful in measurement-based quantum computation. Therefore, an entangled but not too entangled quantum state is needed, in which sense, entanglement measurement and inspection of physics systems are vital. An in-depth analysis can provide a new perspective on the nature of entanglement in nuclear systems.

In a quantum context, Von Neumann entropy usually quantifies the quantum entanglement. We assume that the Hilbert space $\mathcal{H}$ is decomposed as $\mathcal{H} = \mathcal{H}_A \otimes \mathcal{H}_B$ in terms of the Hilbert spaces of two subsystems A and B. The density matrix of the ground state $|\Phi\rangle$ is $\rho_{AB} = |\Phi\rangle\langle\Phi|$, and the reduced density matrix of the subsystem A is obtained by tracing over the subsystem B, i.e. $\rho_A = \mathrm{Tr}_B\, \rho_{AB}$. The density matrices ρ_A and ρ_{AB} are Hermitian, non-negative (i.e., they have non-negative eigenvalues), and fulfill $\mathrm{Tr}\, \rho = 1$. The von Neumann entropy is given by

$$S = -\,\mathrm{Tr}(\rho_A \ln \rho_A)\ . \tag{1.3.1}$$

The state ρ_A is entangled when it can not be represented by a pure state, i.e., $\mathrm{Tr}\, \rho_A^2 < 1$. Also, the non-zero von Neumann entropy indicates the existence of entanglement. The von Neumann mutual information is defined as

$$I(A:B) = S(\rho_A) + S(\rho_B) - S(\rho_{AB})\ , \tag{1.3.2}$$

which is usually used to measure the total correlations between the two subsystems of a bipartite quantum system (Henderson and Vedral, 2001; Modi et al., 2010).

In this dissertation, the more general Rényi entropy (Rényi, 1961) is considered as well, which compacts a one–parametric family of entanglement entropies with the parameter $\alpha \in (0,1) \cup (1,\infty)$, and is defined as

$$S_\alpha = \frac{1}{1-\alpha} \ln \operatorname{Tr} \rho_A^\alpha \ . \tag{1.3.3}$$

S_0, S_2, and S_∞ are usually known as max-entropy, collision entropy, and min-entropy. The von Neumann entropy arises as a limiting case of the Rényi entropy for $\alpha \to 1$, and it is denoted as S_1:

$$S_1 = \lim_{\alpha \to 1} S_\alpha = -\operatorname{Tr}(\rho_A \ln \rho_A) \ , \tag{1.3.4}$$

in this dissertation. When the parameter α gets larger, the Rényi entropy is more determined by the events with higher probabilities (Müller-Lennert et al., 2013). The Rényi entropies are monotonically decreasing for increasing α.

Entanglement is widely studied in different areas of quantum physics like quantum chemistry (Eisert et al., 2010), condensed matter (Zeng et al., 2015; Laflorencie, 2016), and entanglement is usually viewed as a tool to investigate wave function correlation properties. In quantum chemistry, orbital entanglement and its application (Boguslawski et al., 2012; Boguslawski and Tecmer, 2014; Stein and Reiher, 2017) help the measurement of single- and multi-reference characters and dissect chemical reactions (Duperrouzel et al., 2015). Entanglement helps the choice of orbitals (Szalay et al., 2015; Krumnow et al., 2016) in tensor network states and active space optimization (Stein and Reiher, 2016; Ding et al., 2023) by optimizing the entanglement structures.

In nuclear physics, expressions such as "wave-function correlations" or "fluctuations" are often synonyms for entanglement and refer to strong or weak correlations in nuclear systems. Recently, advances in quantum information science and quantum computing also renewed interest in exploring entanglement in nuclear systems (Beane et al., 2019; Kruppa et al., 2021, 2022; Bai and Ren, 2022; Lacroix et al., 2022; Bulgac et al., 2022; Johnson and Gorton, 2022). A better understanding of entanglement could thus benefit both classical and quantum computations of atomic nuclei. In shell-model calculations, understanding entanglement helps when applying the density-matrix renormalization group (Legeza et al.,

2015; Tichai et al., 2022). In Ref. (Robin et al., 2021), single-orbital entanglement entropy and two-orbital mutual information were studied. They are found to be helpful in analyzing the structure of nuclear wave functions and the choice of base states. In Ref. (Faba et al., 2021), entanglement entropy is viewed as a metric for correlation.

Entanglement is necessary for non-locality (Buscemi, 2012) and essential in studying the locality of interactions. The scaling law of entanglement entropy can be viewed as an indicator of the locality. In lattice systems with local interactions, one often finds that the entanglement entropy grows proportional with the area (times some logarithmic corrections) when the system is partitioned into two subsystems (Eisert et al., 2010), and this leads to an area law for entanglement entropy.

For the short-range interaction system, one would expect entanglement entropy S or particle number fluctuation $(\Delta N)^2$ of subsystem would obey area law L^{d-1}, i.e., the boundary area of the subspace, where d is the dimension of the subsystem, and L is a linear dimension of the subsystem. Works done in Ref. (Gioev and Klich, 2006) show a logarithmic correction to the scaling $S \sim L^{d-1}\log(L)$ for free fermions systems. Reference (Gioev and Klich, 2006; Klich, 2006) show $(\Delta N)^2$ as upper and lower bound of S,

$$4(\Delta N)^2 \leq S \leq \mathcal{O}(\log L)(\Delta N)^2\,. \tag{1.3.5}$$

Reference (Leschke et al., 2014) conveys a rigorous proof about the scaling of Rényi entanglement entropies S_α for the free fermi-gas ground state, which shows a logarithmically enhanced area law as well. Entanglement entropies beyond the free case are studied (Barthel et al., 2006a,b). Area law holds in work (Plenio et al., 2005). Logarithmic correction is introduced in work (Wolf, 2006), which studied the fermionic tight-binding Hamiltonians.

The question arises whether area law (or with logarithmic correction) holds in nuclear systems. The Ref. (Masanes, 2009) pointed out two conditions the system with finite range interactions might hold to have (at most) an area law (with the logarithmic correction): "(i) the state has sufficient decay of correlations and (ii) the number of eigenstates with vanishing energy density is not exponential in the volume." While the first condition is expected to be

fulfilled for atomic nuclei, the second seems not. After all, nuclei are open quantum systems, and resonant and scattering states are abundant.

On the first view, area laws should also be held in nuclear physics because the interaction is short-ranged. However, some evidence shows entanglement entropies in nuclear systems fulfill a volume law (Pazy, 2023). Also, for a more detailed discussion, see the Sec. II of Ref. (Gu et al., 2023). This question is one of the main topics of this dissertation and will be discussed in Chapter 3.

1.4 Scope of This Work and My Contributions

As discussed in Sec. 1.1, nuclear physics problems are hard to solve with classical computers, and quantum computing holds much promise for low-energy nuclear theory. My research topic is seeking the application of quantum computation and quantum information in nuclear physics, and this dissertation is based on the published works (Roggero et al., 2020a; Gu et al., 2023), which I co-authored.

Specifically, in the first project (Roggero et al., 2020a), my collaborators and I studied excited states preparation algorithms involving (i) the time-dependent method, which uses unitary evolution for a short time to approximate the action of an excitation operator, and (ii) the Linear Combination of Unitaries (LCU) algorithm. These two techniques were benchmarked on emulated and real quantum devices, using a toy model for thermal neutron-proton capture. My contributions include designing and optimizing quantum circuits, writing *Qiskit* codes, implementing jobs on quantum devices, analyzing read-out results and error extrapolation, analyzing algorithm efficiency, and others.

Specifically, in the second project (Gu et al., 2023), my collaborators and I studied entanglement entropies between the single-particle states of the hole space and its complement in nuclear systems. We calculated the analytical results of entanglement entropies based on the coupled-cluster method. We found they were proportional to the particle number fluctuation and the depletion number of the hole space for sufficiently weak interactions. This indicated a volume law instead of an area law. We tested and confirmed these results by computing entanglement entropies of the pairing model, neutron matter, and the depletion number of

finite nuclei. My contributions include analytical derivation of results based on the coupled-cluster method, numerical entanglement entropy calculation of the pairing model and the neutron matter, analysis of results, and some others.

This dissertation is organized as follows. In Chapter 2, two excited states preparation algorithms are presented, including the time-dependent method in Sec. 2.2, the LCU-based method in Sec. 2.3, and their circuit implication details in Sec. 2.4. Section 2.5 and Sec. 2.6 provide the results for both methods on a simple excitation operator and on the $n(p,d)\gamma$ reaction operator, respectively.

In Chapter 3, the entanglement entropies of nuclear physics systems are studied. Sec. 3.1 briefly introduces the background of nuclear physics and the concepts of quantum information, which are necessary for this dissertation. In Sec. 3.2, I present analytical results for the entanglement entropy in finite systems based on coupled-cluster theory. Sec. 3.3 provides the calculation results of the pairing model and the neutron matter.

Chapter 2

Excited States Preparation Algorithms for Nuclear Dynamics

This chapter is based on the published paper (Roggero et al., 2020a), which I co-authored. My collaborators and I studied the quantum algorithms of excited states preparation, a necessary step in studying quantum dynamics problems on a quantum computer.

In this chapter, I describe two different excited state preparation strategies. The first strategy, which is denoted as the time-dependent method, approximates the Hermitian excitation operator $\hat{O}$ by $\sin(\gamma\hat{O})/\gamma$, valid for small time parameter γ, using the time evolution operator and one additional qubit. The second strategy, which is denoted as the LCU-based method, performs the excitation operation in an exact way using the linear combination of unitary (LCU) algorithm. These two strategies are applied to a toy version of the thermal neutron-proton capture on emulated and real quantum devices, and results will be shown.

2.1 Introduction

As discussed in Chapter 1, quantum computing holds a huge promise in nuclear physics calculation. It is interesting to explore how to prepare, evolve, and solve for quantum states on quantum computers. Inspired by the works of studying linear response function on a quantum computer (Roggero and Carlson, 2019), I am interested in exploring the quantum

algorithms to efficiently apply the excitation operators to an initial state on a quantum register, namely the preparation of excited states. Preparing the excited state is an essential subroutine in most questions and is critical for the performance of quantum computation. Usually, as the first step of a quantum problem, the effort used on the state preparation quantum algorithms must be exponentially less than that used on the classical algorithms to meet the exponential quantum advantage.

Given a Hermitian excitation operator $\hat{O}$ and an initial state of the quantum system as $|\Psi_0\rangle$, I want to find a protocol to prepare the normalized excited state

$$|\Phi_E\rangle = \frac{1}{\eta}\hat{O}\,|\Psi_0\rangle \quad \text{with} \quad \eta = \left\|\hat{O}\,|\Psi_0\rangle\right\| \ . \tag{2.1.1}$$

Here, the norm η is the vector 2-norm.

As described in Ref. (Barenco et al., 1995), all unitary operations on arbitrarily many qubits $n(\mathrm{U}(2^n))$ can be expressed as compositions of elementary operations. Quantum computers can apply a series of unitary gates to the quantum registers. Things become more complicated for non-unitary operations (Terashima and Ueda, 2005) since, unlike unitary operations, quantum computers can not directly apply non-unitary gates to the quantum registers. The technique employed involves embedding non-unitary operations into unitary operations, a process that allows us to produce a state $|\Phi_A\rangle$ to approximate the exact excited state $|\Phi_E\rangle$ with a guaranteed fidelity $F = |\langle\Phi_E|\Phi_A\rangle|^2$ and a success probability P_s. This chapter discusses two strategies for approaching this question.

Throughout this chapter, I use Qiskit (Qiskit contributors, 2023) and first implement the relevant quantum circuits on the virtual machine (VM) QasmSimulator, which is a noisy quantum circuit simulator backend, with the noise model, basis gates, and coupling map mimicking an IBM *Quantum* (IBM Q) backend, a quantum cloud service released by IBM. As well, I implement the circuit on the quantum processor unit (QPU) provided by IBM Q. The QPU used in this chapter is the IBM Q backend Vigo (5qubit backed: IBM Q team, 2020), and its layout and connectivity are shown in Fig. 2.1.

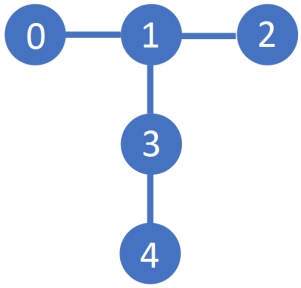


Figure 2.1: Qubits layout and connectivity of the IBM *Quantum* backend Vigo (5qubit backed: IBM Q team, 2020). The circles with number labels are the qubits, and the connection lines represent the connectivity between qubits. The figure is taken from Ref. (Roggero et al., 2020a), which I co-authored.

2.2 Time-dependent Method

This section introduces the time-dependent method, which uses a unitary evolution

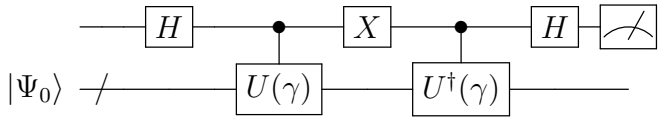
$$\hat{U}(\gamma) = \exp\left(-i\gamma\hat{O}\right) = \cos\left(\gamma\hat{O}\right) - i\sin\left(\gamma\hat{O}\right) \ , \tag{2.2.1}$$

for a short enough time to approximate the associated excitation operator $\hat{O}$. The "time" parameter γ is a positive number. The outcome of this algorithm is producing the approximate state

$$|\Psi_A(\gamma)\rangle \propto \sin\left(\gamma\hat{O}\right)|\Psi_0\rangle = |\Phi_E\rangle + \mathcal{O}(\gamma^2) \ , \tag{2.2.2}$$

to the target state $|\Phi_E\rangle$, described in Eq. (2.1.1).

The quantum procedure can be represented with the quantum circuit as

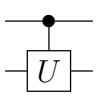


(2.2.3)

The first line is for the auxiliary qubit, or the "ancilla" register, and the second line is for the target qubits or the quantum register. The slash on the second line represents a line containing multiple qubits. The meter at the end represents a projective measurement.

Here and in what follows, the gates X, Y and Z represent the Pauli matrices $\hat{\sigma}_x$, $\hat{\sigma}_y$ and $\hat{\sigma}_z$, and gate H is the Hadamard gate, see Appendix A for the explicit definition. No initial state is specified on the left-hand side of the ancilla register. Usually, without losing generality, the ancilla qubit is prepared to be in state $|0\rangle$ or $|1\rangle$. The target qubits are initialized to be in state $|\Psi_0\rangle$, which could be the ground state of a many-body Hamiltonian.

The main part is the controlled-U ($U^\dagger$) gate, a unitary gate controlled by the status of the ancilla qubit. Equivalently in matrix representation, controlled-U is defined as



$$= \begin{pmatrix} \mathbb{I} & 0 \\ 0 & U \end{pmatrix} . \tag{2.2.4}$$

where the Hilbert space is spanned by $|0\rangle\otimes|\Psi_0\rangle$ and $|1\rangle\otimes|\Psi_0\rangle$. Here and in what follows, the operator $\mathbb{I}$ represents the identity operator. The black solid point represents the controlled-U

applies the unitary operation $\hat{U}$ to the target qubits when the ancilla qubit is in state $|1\rangle$, and does nothing when the ancilla qubit is in state $|0\rangle$.

To be more clear, the unitary operation corresponding to the circuit (2.2.3) (apart from the measurement) can be written as

$$V(\gamma) = \begin{pmatrix} \cos\left(\gamma\hat{O}\right) & i\sin\left(\gamma\hat{O}\right) \\ -i\sin\left(\gamma\hat{O}\right) & -\cos\left(\gamma\hat{O}\right) \end{pmatrix} \ . \tag{2.2.5}$$

If the ancilla qubit is prepared in the state $|0\rangle$, the circuit produces the final state (before the measurement) as follows:

$$\begin{aligned} |\Omega(\gamma)\rangle &= V(\gamma)\,|0\rangle\otimes|\Psi_0\rangle \\ &= |0\rangle\otimes\cos\left(\gamma\hat{O}\right)|\Psi_0\rangle - i\,|1\rangle\otimes\sin\left(\gamma\hat{O}\right)|\Psi_0\rangle \ . \end{aligned} \tag{2.2.6}$$

The part of interest, $\sin\left(\gamma\hat{O}\right)$, is embedded in the second component. The technique is postselecting those measurements when the ancilla qubit in the state $|1\rangle$, then the quantum register will turn out to be in the state

$$|\Psi_A(\gamma)\rangle = \frac{-i}{\sqrt{\left\langle\Psi_0\left|\sin^2(\gamma\hat{O})\right|\Psi_0\right\rangle}}\sin(\gamma\hat{O})\,|\Psi_0\rangle \ . \tag{2.2.7}$$

To summarize, the function of the whole circuit (2.2.3) contains two parts: (i) the unitary operation part (2.2.5), and (ii) the postselection part, which is denoted as the meter at the end of the circuit (2.2.3). And due to its inherently stochastic measurements, it does not promise us to obtain the final state (2.2.7) every measurement, but with a success probability as

$$P_s = \langle\Psi_0|\sin^2(\gamma\hat{O})\,|\Psi_0\rangle = \mathcal{O}\left(\gamma^2\right) \ , \tag{2.2.8}$$

and thus at least one needs measurements of order $\mathcal{O}\left(1/\gamma^2\right)$ to obtain the state of interest.

To guarantee relatively large fidelity, it is required that the time parameter γ be small, while small γ leads to a small success probability of postselection. It is necessary to consider

the tradeoff between high fidelity and success probability of the final state, which is discussed in the following subsection 2.2.1.

2.2.1 Fidelities and Success Probabilities Analysis

To quantify fidelities and success probabilities, I decompose the excitation operator $\hat{O}$ as:

$$\hat{O} = \sum_{k=0}^{L} \lambda_k \hat{U}_k \quad \lambda_k > 0 \,, \tag{2.2.9}$$

and denote the 1-norm of the coefficient vector as

$$\Lambda = \sum_{k=0}^{L} \lambda_k \geq \|\hat{O}\| \,, \tag{2.2.10}$$

with $\|\cdot\|$ the operator spectral norm.

The bounds for the success probability Eq. (2.2.8) is derived as:

$$\min\left[\sin^2(\gamma\Lambda)\,, \gamma^2\eta^2\right] \geq P_s \geq \gamma^2\eta^2\left(1 - \frac{\gamma^2\Lambda^2}{3}\right) \,. \tag{2.2.11}$$

Remember here that η is defined in Eq. (2.1.1) as the vector 2-norm of exact excited state $|\Psi_E\rangle$. The lower bound for the state fidelity is derived as

$$\begin{aligned} F(\gamma) = |\langle\Psi_E \mid \Psi_A\rangle|^2 &= \frac{1}{\eta^2}\frac{|\langle\Psi_0|O\sin(\gamma O)|\Psi_0\rangle|^2}{\left\langle\Psi_0\left|\sin^2(\gamma O)\right|\Psi_0\right\rangle} \\ &\geq \frac{1}{\eta^2\gamma^2}\langle\Psi_0|O\sin(\gamma O)|\Psi_0\rangle \\ &\geq \left(1 - \frac{\gamma^2\Lambda^2}{6}\right) . \end{aligned} \tag{2.2.12}$$

For the details of the derivation, I refer the readers to Appendix A in Ref. (Roggero et al., 2020a), in which the upper and lower bounds for expectations $\langle\sin(X)^2\rangle$ and $\langle X\sin(X)\rangle$ are shown. Here, $\|X\| \leq \pi/2$, and this requirement constrains the time parameter to a small value $\gamma \in [0, \pi/2\Lambda]$.

If guaranteeing a minimum fidelity of the approximated state as

$$F_{\min} \geq (1 - \pi^2/24) \approx 0.59 \ ,$$

where the value is obtained when $\gamma = \pi/2\Lambda$, the parameter γ should fulfill the limit

$$\gamma \leq \frac{\sqrt{6\,(1 - F_{\min})}}{\Lambda} \ . \tag{2.2.13}$$

The corresponding success probability is bounded by

$$\frac{\eta^2}{\Lambda^2}\,(2F_{\min} - 1) \leq P_s \leq \sin^2\left(\sqrt{6\,(1 - F_{\min})}\right) \ . \tag{2.2.14}$$

When the infidelity $\Delta_f = 1 - F_{\min}$ is small, The upper bound of success probability can be simplified as $P_s \leq 6\Delta_f$. The lower bound of success probability guarantees its minimum value as $0.18\eta^2/\Lambda^2$.

To clarify the analysis of fidelities and success probabilities, I show detailed calculations based on an example of the simple operator

$$\hat{O}(\theta) = \cos(\theta)X + \sin(\theta)\mathbb{I} \ , \tag{2.2.15}$$

with $\theta \in [0, \pi]$. The excited state vector 2-norm is $\eta = 1$ for any angle. The 1-norm of this operator has a simple upper bound as

$$\Lambda(\theta) = |\sin(\theta)| + |\cos(\theta)| \leq \sqrt{2} \equiv \Lambda_{\max} \ . \tag{2.2.16}$$

For simplification, the bound $\Lambda_{\max}$ is used in the following analysis instead of $\Lambda(\theta)$. Therefore, the constrain of time parameter is obtained from Eq. (2.2.13) as $\gamma \leq \sqrt{3\Delta_f}$, and the corresponding allowed values of γ is depicted in the lower panel of Fig. 2.2 as the gray region.

The top panel of Fig. 2.2 gives estimated upper and lower bounds for the success probability P_s, Eq. (2.2.11), versus the target infidelity Δ_f. The upper-bound B is provided

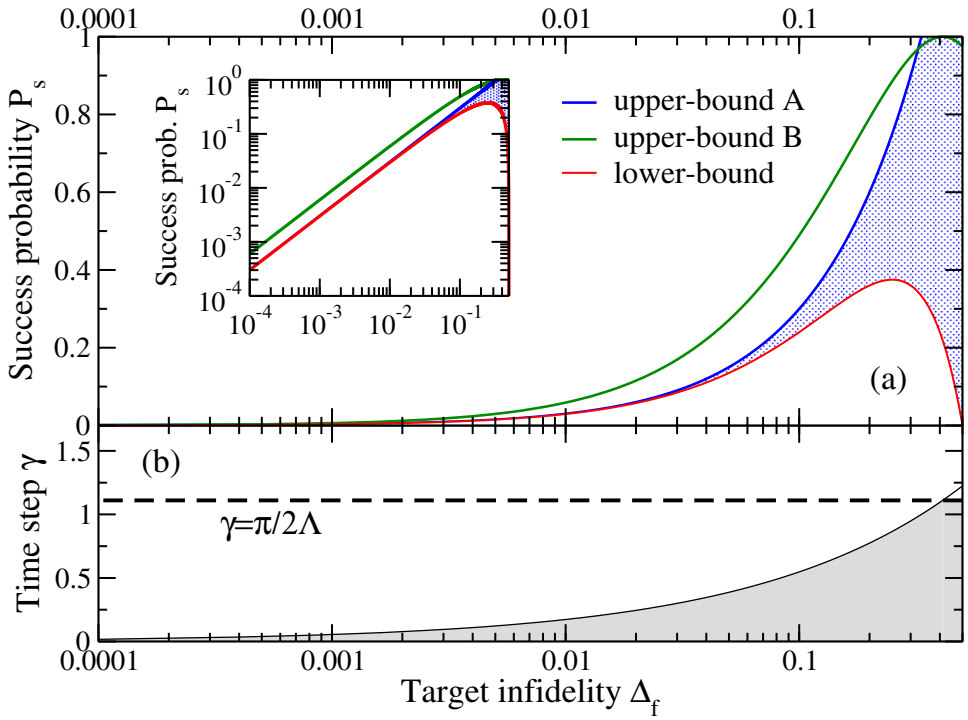


Figure 2.2: Estimated success probability P_s in subplot (a) and the allowed value for time steps γ in subplot (b) versus the target infidelity Δ_f. More details of success probability values for small infidelity are shown in the inset of the top panel; note the log scale here. The figure is taken from Ref. (Roggero et al., 2020a), which I co-authored.

by the bound $\gamma^2\eta^2$, and the upper-bound A is provided by the bound $\sin^2(\gamma\Lambda)$, which is smaller for most values of infidelity. To achieve large fidelity as well as sufficiently large success probability, one can set $\gamma = 0.3$, which gives a high fidelity

$$F(0.3) \geq 97\% \ ,$$

and a relatively large success probability as

$$9\% \geq P_s(0.3) \geq 8.46\% \ .$$

A better analysis could be obtained using the tighter bound $\Lambda(\theta)$ instead of $\Lambda_{\max}$.

2.2.2 Imperfect Time Evolution

This subsection discusses the influence of the fact that the unitary gates $U(\gamma)$ can not be exactly implemented in practice and considers the situation only an approximated unitary operation $\widetilde{U}(\gamma)$ with some additive error δ_U can be obtained, and shows how this modification will change the efficiency of this method. The derivation details are also shown in Appendix B in Ref. (Roggero et al., 2020a).

With this approximated unitary operation $\widetilde{U}(\gamma)$, the function of circuit (2.2.3) is written as $\widetilde{V}(\gamma)$, instead of $V(\gamma)$. The difference between these two unitaries is denoted as

$$\left\| \widetilde{V}(\gamma) - V(\gamma) \right\| \leq \delta_V \ , \tag{2.2.17}$$

with a total error $\delta_V \leq 2\delta_U$. After implementation of $\widetilde{V}(\gamma)$, the state is obtained as

$$\begin{aligned} \left| \widetilde{\Omega}(\gamma) \right\rangle &= \widetilde{V}(\gamma) \left| 0 \right\rangle \otimes \left| \Psi_0 \right\rangle \\ &= \cos(\alpha) \left| \Omega(\gamma) \right\rangle + \sin(\alpha) \left| \xi(\gamma) \right\rangle \ . \end{aligned} \tag{2.2.18}$$

Here, the normalized state $|\xi(\gamma)\rangle$ is introduced to depict the orthogonal states to the error-free vector $|\Omega(\gamma)\rangle$, given in Eq. (2.2.6). The difference is defined as

$$|E\rangle = |\Omega(\gamma)\rangle - \left|\widetilde{\Omega}(\gamma)\right\rangle \ ,$$

and the bound for its norm is given as

$$\begin{aligned} \| \, |E\rangle \, \|^2 &= \langle i| \left(\widetilde{V}^\dagger - V^\dagger\right) \left(\widetilde{V} - V\right) |i\rangle \\ &\leq \max_{\lambda \in \sigma[\left(\widetilde{V}^\dagger - V^\dagger\right)\left(\widetilde{V} - V\right)]} \lambda \\ &\equiv \max_{s_i \in \{\text{singular values of } \widetilde{V} - V\}} s_i^2 \\ &\equiv \|\widetilde{V} - V\|^2 \leq \delta_V^2 \end{aligned}$$

here the initial state is written as $|i\rangle = |0\rangle \otimes |\Psi_0\rangle$. The spectrum of the corresponding operator is denoted as $\sigma[\cdot]$. Also, the norm of this difference is written as

$$\begin{aligned} \| |E\rangle \|^2 &= \| (\cos(\alpha) - 1) \, |\Omega(\gamma)\rangle + \sin(\alpha) \, |\xi\rangle \|^2 \\ &= (\cos(\alpha) - 1)^2 + \sin(\alpha)^2 \\ &= 2 \, |1 - \cos(\alpha)| \ . \end{aligned}$$

Combining two results gives the lower bound for overlap as

$$\begin{aligned} \cos(\alpha) &\geq 1 - \frac{\delta_V^2}{2} \ , \\ \sin(\alpha) &\leq \delta_V \sqrt{1 - \frac{\delta_V^2}{4}} \ . \end{aligned} \tag{2.2.19}$$

The postselected state (after selecting ancilla qubit being in the state $|1\rangle$) with faulty implementation is

$$\left|\widetilde{\Phi}_A\right\rangle = |1\rangle \otimes \left|\widetilde{\Psi}_A\right\rangle = \frac{\Pi_1}{\sqrt{\widetilde{P}_s}} \left|\widetilde{\Omega}(\gamma)\right\rangle \ , \tag{2.2.20}$$

where $\Pi_1 = |1\rangle\langle 1| \otimes \mathbb{I}$ is the projector projects ancilla qubit onto state $|1\rangle$, and the difference between the modified success probability $\widetilde{P}_s$ and the success probability P_s is defined as

$$\begin{aligned}\left|\widetilde{P_s} - P_s\right| &= \left|\left\langle\widetilde{\Omega}(\gamma)\right| \Pi_1 \left|\widetilde{\Omega}(\gamma)\right\rangle - \langle\Omega(\gamma)| \Pi_1 |\Omega(\gamma)\rangle\right| \\ &= |\mathrm{Tr}(\Pi_1\rho) - \mathrm{Tr}(\Pi_1\sigma)| \\ &= |\mathrm{Tr}\left(\Pi(\rho-\sigma)\right)| \\ &\leq D(\rho,\sigma) = \frac{1}{2}\,\mathrm{Tr}\,|\rho-\sigma| = |\sin(\theta)| \ .\end{aligned}$$

Here, $\rho = |\widetilde{\Omega}\rangle\langle\widetilde{\Omega}|$ and $\sigma = |\Omega\rangle\langle\Omega|$ are the density matrices, $D(\rho,\sigma)$ is the trace distance. Therefore, with Eq. (2.2.19), the modified success probability $\widetilde{P}_s$ is constrained closely to P_s, and is written as

$$P_s - \delta_V\sqrt{1-\frac{\delta_V^2}{4}} \leq \widetilde{P_s} \leq P_s + \delta_V\sqrt{1-\frac{\delta_V^2}{4}} \ . \tag{2.2.21}$$

The modified fidelity $\widetilde{F}$ is given by

$$\widetilde{F} = \left|\left\langle\Psi_E|\widetilde{\Psi}_A\right\rangle\right|^2 = \frac{\left|\left\langle\Psi_E\left|\Pi_1\right|\widetilde{\Omega}(\gamma)\right\rangle\right|^2}{\widetilde{P}_s} \ .$$

After a similar process of analyzing the bound for $\widetilde{F}$, one get

$$\begin{aligned}\left|\widetilde{P}_s\widetilde{F} - P_sF\right| &= \left|\left\langle\widetilde{\Omega}\right| \Pi \left|\widetilde{\Omega}\right\rangle - \langle\Omega| \Pi |\Omega\rangle\right| \\ &\leq \delta\sqrt{1-\delta^2/4} \ ,\end{aligned}$$

where $\Pi = |1\rangle\langle 1| \otimes |\Psi_E\rangle\langle\Psi_E|$. Therefore, combining with results Eq. (2.2.11) and Eq. (2.2.12), the bound for the fidelity is written as

$$\begin{aligned}\widetilde{F} &\geq \frac{P_sF - \delta\sqrt{1-\delta^2/4}}{\widetilde{P_s}} \\ &\geq \frac{\gamma^2\eta^2(1-\frac{\gamma^2\Lambda^2}{3})F - \delta\sqrt{1-\delta^2/4}}{\gamma^2\eta^2 + \delta\sqrt{1-\delta^2/4}} \\ &\geq \left(1-\frac{\gamma^2\Lambda^2}{2}\right) - \left(2-\frac{\gamma^2\Lambda^2}{3}\right)\frac{\delta}{\gamma^2\eta^2} \ .\end{aligned}$$

Taylor expansion with respect to $\delta\sqrt{1-\delta^2/4}$ is applied in the third line.

To guarantee a fidelity of at least $\widetilde{F}_{\min}$, let us take

$$\gamma \leq \frac{\sqrt{1-F_{\min}}}{\Lambda} \ . \tag{2.2.22}$$

This ensures that the approximation error induced by the approximate time evolution is bounded by

$$\delta_V \leq \frac{\eta^2}{4}\gamma^4\eta^2\Lambda^2 \leq \frac{\eta^2}{2\Lambda^2}\left(1-F_{\min}\right)^2 \ . \tag{2.2.23}$$

The error δ_U for the time-evolution unitary is

$$\delta_U(\gamma) \leq \frac{\eta^2}{8}\gamma^4\eta^2\Lambda^2 \leq \frac{\eta^2}{4\Lambda^2}\left(1-F_{\min}\right)^2 \ . \tag{2.2.24}$$

To make the imperfect time evolution analysis clear, I use the operator $\hat{O}(\theta) = \cos(\theta)X + \sin(\theta)\mathbb{I}$ as an example (actually this example can be exactly implemented). The fidelity F and success probability P_s are calculated in Sec. 2.2.1. The bound $\Lambda_{\max} = \sqrt{2}$ is used in the following analysis. If we choose $\gamma = 0.3$, based on Eq. (2.2.23), we get

$$\delta_V(0.3) \leq 0.405\% \ ,$$

and it is small that we ignore those higher order of δ_V in Eq. (2.2.21), i.e., $\widetilde{P_s}(0.3)$ is a little bit more loosely bounded than $P_s(0.3)$ by 0.405%. While the new fidelity is guaranteed as

$$\widetilde{F}(0.3) \geq 82\% \ ,$$

which is less than the 97%. We can see that even for a small time interval γ, the time-dependent method quickly becomes inefficient due to the imperfect implementation of quantum gates.

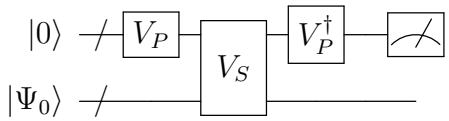
2.3 LCU-based Method

In this section, the LCU-based method is introduced. Performing the non-unitary operation in Eq. (2.1.1) can be done non-deterministically in an exact way using the linear combination of unitaries (LCU) technique in Ref. (Childs and Wiebe, 2012) whenever we can decompose the excitation operator $\hat{O}$ as

$$\hat{O} = \sum_{k=0}^{L} \lambda_k \hat{U}_k \quad \lambda_k > 0 \ , \tag{2.3.1}$$

provided each U_k can be implemented efficiently on a quantum computer. The total number of terms, $L+1$, grows as a low-order polynomial of the system size.

The quantum procedure of the LCU-based method can be depicted as follows:



, (2.3.2)

the first line represents the ancilla register, and the second line represents the quantum register. Unlike the time-dependent method, which only needs one ancilla qubit, the LCU-based method requires many more ancilla qubits. The size of ancilla register is denoted as M, and it depends on the number of unitaries $L+1$, with the relation as $M = \lceil \log_2(L+1) \rceil$. Here, the ancilla registers are initialized in the state $|0\rangle^{\otimes M}$ (written as $|0\rangle$ for simplification), and the quantum registers are initialized in the state $|\Psi_0\rangle$.

The circuit requires the implementation of two unitary gates. First, the *prepare* unitary gate V_P, which only acts on the ancilla register, is defined as

$$V_P|0\rangle = \sum_{k=0}^{L} \sqrt{\frac{\lambda_k}{\Lambda}} |k\rangle \ , \tag{2.3.3}$$

and second the *select* unitary gate V_S is defined as

$$V_S = \sum_{k=0}^{L} |k\rangle\langle k| \otimes U_k \ . \tag{2.3.4}$$

Here $|k\rangle\langle k|$ projects ancilla qubits into state $|k\rangle$.

The function of the circuit (2.3.2) (before the measurement) is denoted as the operator W, and the state after implementation of W is decomposed as (see, e.g., Refs. (Childs and Wiebe, 2012; Childs et al., 2017))

$$|\Omega\rangle = W|0\rangle \otimes |\Psi_0\rangle = \frac{1}{\Lambda}|0\rangle \otimes \hat{O}\,|\Psi_0\rangle + \left|\Phi^{\perp}\right\rangle \ . \tag{2.3.5}$$

Here $\left|\Phi^{\perp}\right\rangle$ is introduced to depict the orthogonal states of $|0\rangle$, i.e.,

$$(|0\rangle\langle 0| \otimes \mathbb{I})\left|\Phi^{\perp}\right\rangle = 0 \ . \tag{2.3.6}$$

Then, after postselecting the measurements, of which the ancilla registers are in state $|0\rangle$, the final state (not normalized) is obtained as

$$(|0\rangle\langle 0| \otimes \mathbb{I})\,|\Omega\rangle = \frac{1}{\Lambda}\,|0\rangle \otimes \hat{O}\,|\Psi_0\rangle = \frac{\eta}{\Lambda}\,|0\rangle \otimes |\Phi_E\rangle \ . \tag{2.3.7}$$

The fidelity of the LCU-based method is

$$F^{\mathrm{LCU}} = 1 \ ,$$

and the success probability is

$$P_s^{\mathrm{LCU}} = \frac{\eta^2}{\Lambda^2} \ . \tag{2.3.8}$$

We have two methods at our disposal to obtain the normalized $|\Phi_E\rangle$. The first involves rescaling with the known norm Λ, which effectively mitigates the influence of statistical fluctuations. The second method utilizes the empirical success probability to achieve the same result. The latter one is more practical from an operational standpoint. Thus, we first estimate empirically the success probability P_s^{LCU}, and then compute the estimator

$$\langle\Phi_E|A|\Phi_E\rangle = \frac{\langle\Omega|\mathbb{I} \otimes A|\Omega\rangle}{P_s^{\mathrm{LCU}}} \ . \tag{2.3.9}$$

Comparing the success probability presented in Eq. (2.3.8) with the success probability bounds [see Eqs. (2.2.11) and (2.2.13)] for the time-dependent method, we can see that the

LCU-based method has a higher success probability whenever the target infidelity satisfies $\Delta_f \leq 1/6$.

2.4 Circuit Implementation Details

This section derives and presents the circuit implementation details for the time-dependent method and the LCU-based method.

2.4.1 Time-dependent Method

Before delving into the details of circuit implementation, I will discuss the Euler decomposition of a generic 2×2 unitary. Provided with a generic hermitian 2×2 matrix, which is written as

$$\begin{aligned} \hat{O} &= \frac{\alpha+\gamma}{2}\mathbb{I} + \beta_1 X + \beta_2 Y + \frac{\alpha-\gamma}{2} Z \\ &= \begin{pmatrix} \alpha & \beta_1 - i\beta_2 \\ \beta_1 + i\beta_2 & \gamma \end{pmatrix} . \end{aligned} \tag{2.4.1}$$

In this dissertation, only excitation operators with real matrix elements are tested, i.e., $\beta_2 = 0$, but the more generic case is considered in this discussion. The corresponding time evolution can be written as

$$\begin{aligned} e^{-it\hat{O}} &= e^{-it\frac{\alpha+\gamma}{2}} e^{-i\theta\hat{\theta}\cdot\boldsymbol{\sigma}} \\ &= e^{-it\frac{\alpha+\gamma}{2}} \left(\mathbb{I}\cos(\theta) - i\hat{\theta}\cdot\boldsymbol{\sigma}\sin(\theta) \right) , \end{aligned} \tag{2.4.2}$$

where

$$\begin{aligned} \vec{\theta} &= \left(t\beta_1,\, t\beta_2,\, t\frac{\alpha-\gamma}{2} \right) , \\ \theta &= \frac{t}{2}\sqrt{4\beta_1^2 + 4\beta_2^2 + (\alpha-\gamma)^2} , \\ \hat{\theta} &= \vec{\theta}/\theta = \left(\hat{\theta}_x,\, \hat{\theta}_y,\, \hat{\theta}_z \right) . \end{aligned}$$

Using the Euler decomposition, the propagator can be expressed by using three angles and a phase parameter written as

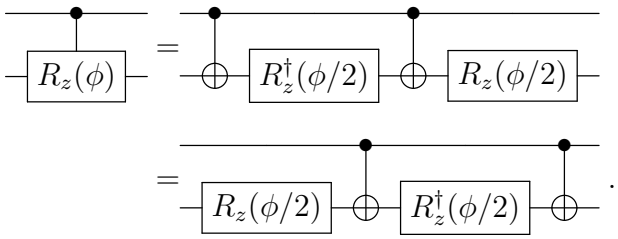
$$e^{-it\hat{O}} = e^{-i\delta} R_z(x_1) R_y(x_2) R_z(x_3)\,, \tag{2.4.3}$$

with $\delta = \frac{\alpha+\gamma}{2}t$. Matching the coefficients, the parameters x_1, x_3 can be obtained via equations

$$\begin{aligned} \hat{\theta}_z \tan\theta &= \tan\tfrac{x_1+x_3}{2}\,, \\ \frac{\hat{\theta}_x}{\hat{\theta}_y} &= -\tan\tfrac{x_1-x_3}{2}\,, \end{aligned}$$

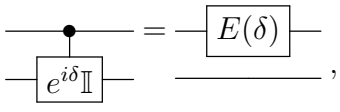
and x_2 can be therefore obtained.

Next, I present in detail how to decompose and implement the quantum circuits (2.2.3) using the excitation operator $\hat{O}$ (2.4.1), which is a general 2×2 operator. After decomposing the unitary as Eq. (2.4.3) into Euler rotation operators, with three angles x_1, x_2, x_3 and a phase parameter δ, the controlled unitary can be implemented using three controlled one-qubit rotation gates and one controlled phase gate. A controlled R_z gate can be written as



(2.4.4)

A controlled R_y gate can be written similarly to Eq. (2.4.4) by replacing R_z rotations with R_y rotations. A controlled phase gate can be written as



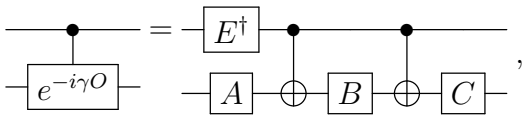
(2.4.5)

with

$$E(\delta) = \begin{pmatrix} 1 & 0 \\ 0 & e^{i\delta} \end{pmatrix}. \tag{2.4.6}$$

The gate $E(\delta)$ is equivalent to the $R_z(\delta)$ gate as in Eq. (A.1), up to an overall phase. Therefore, the controlled time-evolution operator is decomposed into one-qubit gates and CNOTs.

A more efficient approach to decomposing controlled unitary is described in Ref. (Barenco et al., 1995)(Lemma 5.1 and Lemma 5.2),



(2.4.7)

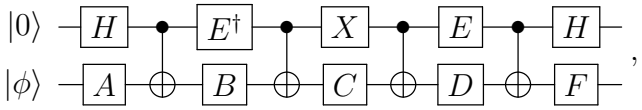
with

$$
\begin{aligned}
A &= \mathrm{R_z}\left(\frac{x_3 - x_1}{2}\right), \\
B &= \mathrm{R_y}\left(-\frac{x_2}{2}\right) \cdot \mathrm{R_z}\left(-\frac{x_1 + x_3}{2}\right), \\
C &= \mathrm{R}_z(x_1) \cdot \mathrm{R_y}\left(\frac{x_2}{2}\right).
\end{aligned}
\tag{2.4.8}
$$

Use the same decomposition approach to deal with controlled-$U^\dagger$, with the Euler decomposition of $U^\dagger$ as

$$
e^{i\gamma\hat{O}} = e^{i\delta} R_z(-x_1) R_y(x_2) R_z(-x_3), \tag{2.4.9}
$$

the final circuit as circuit (2.4.10) is shown as



(2.4.10)

where

$$
\begin{aligned}
C &= \mathrm{R_z}\left(\frac{x_1 - x_3}{2}\right) \cdot \mathrm{R_z}(x_1) \cdot \mathrm{R_y}\left(\frac{x_2}{2}\right), \\
D &= \mathrm{R_y}\left(-\frac{x_2}{2}\right) \cdot \mathrm{R_z}\left(\frac{x_1 + x_3}{2}\right), \\
F &= \mathrm{R_z}\left(-x_1\right) \cdot \mathrm{R_y}\left(\frac{x_2}{2}\right).
\end{aligned}
\tag{2.4.11}
$$

Here gate A and B are given in circuit (2.4.7), gate E is given in Eq. (2.4.6).

Implementing the circuit (2.4.10) requires at most 4 CNOTs, which could be more optimal. The optimal quantum circuit for a general two-qubit gate has been studied that only requires at most 3 CNOT gates and 15 elementary one-qubit gates; see, for example, Theorem 5 in Ref. (Vatan and Williams, 2004).

2.4.2 LCU-based Method

This subsection provides a representative simple example of creating circuits with the LCU-based method, using a simple operator introduced in Eq. (2.2.15). A similar procedure can be generated for more complicated excitation operators. For a detailed description of Hamiltonian simulation using the LCU-based method, I refer the readers to Ref. (Childs and Wiebe, 2012).

The operator is a sum of two unitaries. Thus, we need one ancilla qubit and one qubit for the target qubit. Examining how the circuit (2.3.2) works with this operator is simple, and this will be shown as a demonstration. The *prepare* unitary from Eq. (2.3.3) can be implemented using a single rotation R_y, i.e., $V_P = R_y(\phi_1)$, which gives the result as

$$|\Phi_1\rangle_a = R_y(\phi_1)\,|0\rangle_a = \cos\frac{\phi_1}{2}\,|0\rangle_a + \sin\frac{\phi_1}{2}\,|1\rangle_a \ ,$$

with the subscript a denotes ancilla qubit. Then the implementation of the *select* unitary Eq. (2.3.4) onto the system gives the resulting state as

$$V_s\left(|\Phi_1\rangle_a \otimes |\Psi_0\rangle\right) = \cos\frac{\phi_1}{2}\,|0\rangle_a \otimes U_0\,|\Psi_0\rangle + \sin\frac{\phi_1}{2}\,|1\rangle_a \otimes U_1\,|\Psi_0\rangle \ .$$

Assume that the quantum register is initialized in state $|\Psi_0\rangle$, which is not specified. Then the implementation of the inverse of *prepare* unitary $V_P^\dagger = R_y(-\phi_1)$ gives the final state as

$$\begin{aligned}
&R_y(-\phi_1)\cos\frac{\phi_1}{2}\,|0\rangle_a \otimes U_0\,|\Psi_0\rangle + R_y(-\phi_1)\sin\frac{\phi_1}{2}\,|1\rangle_a \otimes U_1\,|\Psi_0\rangle \\
=&\cos^2\frac{\phi_1}{2}\,|0\rangle_a \otimes U_0\,|\Psi_0\rangle - \sin\frac{\phi_1}{2}\cos\frac{\phi_1}{2}\,|1\rangle_a \otimes U_0\,|\Psi_0\rangle + \\
&\sin^2\frac{\phi_1}{2}\,|0\rangle_a \otimes U_1\,|\Psi_0\rangle + \cos\frac{\phi_1}{2}\sin\frac{\phi_1}{2}\,|1\rangle_a \otimes U_0\,|\Psi_0\rangle \ .
\end{aligned}$$

After postselecting those measurements in which the ancilla qubit in state $|0\rangle_a$, the resulting state of the whole circuit (2.3.2) is obtained as

$$\left|\tilde{f}\right\rangle = \cos^2\frac{\phi_1}{2}\,|0\rangle_a \otimes U_0\,|\Psi_0\rangle + \sin^2\frac{\phi_1}{2}\,|0\rangle_a \otimes U_1\,|\Psi_0\rangle \ ,$$

up to some normalization coefficient. Comparing with the wanted resulting state $|f\rangle = |0\rangle_a \otimes O\,|\Psi_0\rangle$, we choose $U_0 = \mathbb{I}$, $U_1 = X$ and the angle

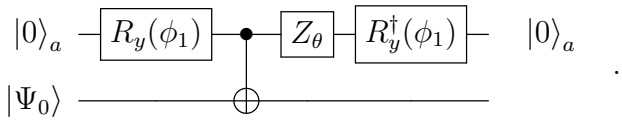
$$\phi_1 = 2\arcsin\left(\sqrt{\frac{|\cos(\theta)|}{|\cos(\theta)| + \sin(\theta)}}\right) \ . \tag{2.4.12}$$

Then, the final state is written as

$$\left|\tilde{f}\right\rangle = \frac{\sin(\theta)}{|\cos(\theta)| + \sin(\theta)}\,|0\rangle_a \otimes |\Psi_0\rangle + \frac{|\cos(\theta)|}{|\cos(\theta)| + \sin(\theta)}\,|0\rangle_a \otimes X\,|\Psi_0\rangle \ , \tag{2.4.13}$$

up to some normalization coefficient.

Therefore, the complete state preparation circuit, in summary, is depicted as

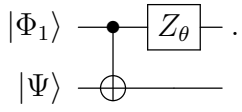


. (2.4.14)

Here, the additional Z_θ is necessary to account for the sign of the cosine for $\theta > \pi/2$, its matrix representation is

$$\begin{aligned} Z_\theta &\equiv \begin{cases} \mathbb{I} & \text{for} \quad \theta \in [0, \pi/2] \\ Z & \text{for} \quad \theta \in [\pi/2, \pi] \end{cases} \\ &= \begin{pmatrix} 1 & 0 \\ 0 & 1 - 2H(\theta - \pi/2) \end{pmatrix} \ . \end{aligned} \tag{2.4.15}$$

Here $H(x)$ is the Heaviside step function. More clearly, the *select* unitary is depicted as



.

Next, I provide the circuit details for the excitation operator Eq. (2.2.15) in a second quantized form, which is the operator used in Subsec. 2.5.2

$$\widetilde{O}(\theta) = \sin(\theta)(c_1^\dagger c_1 + c_0^\dagger c_0) + \cos(\theta)(c_0^\dagger c_1 + c_1^\dagger c_0) \,, \tag{2.4.16}$$

which requires two qubits for the system register.

Beased the Jordan-Wigner transformation (Eq. (1.2.2) and Eq. (1.2.3)), we have

$$c_k = \frac{X_k - iY_k}{2} \quad , \quad c_k^\dagger = \frac{X_k + iY_k}{2} \,. \tag{2.4.17}$$

The operator in terms of Pauli matrices is given as

$$\widetilde{O}(\theta) = \frac{\cos(\theta)}{2}\left(X_0X_1 + Y_0Y_1\right) + \sin(\theta)\mathbb{I} \,. \tag{2.4.18}$$

Here $\mathbb{I}$ denotes the 4×4 identity. The implementation needs two qubits for the quantum register and two qubits for the ancilla register.

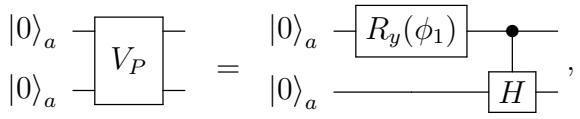
I use the following mapping for *select* unitary

$$|00\rangle_a \to \mathbb{I} \,, \quad |10\rangle_a \to X_0X_1 \,, \quad |11\rangle_a \to Y_0Y_1 \,. \tag{2.4.19}$$

A more intuitive way to express the *select* unitary is

$$V_s = |00\rangle_a \langle 00|_a \otimes \mathbb{I} + |10\rangle_a \langle 10|_a \otimes X_0X_1 + |11\rangle_a \langle 11|_a \otimes Y_0Y_1 \,. \tag{2.4.20}$$

The *prepare* unitary is depicted as



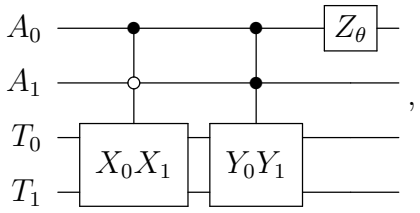
, (2.4.21)

which gives the state

$$|\Phi_2\rangle = \cos(\phi_1)\,|00\rangle + \sin(\phi_1)\,|1\rangle \otimes \frac{|0\rangle + |1\rangle}{\sqrt{2}} \,. \tag{2.4.22}$$

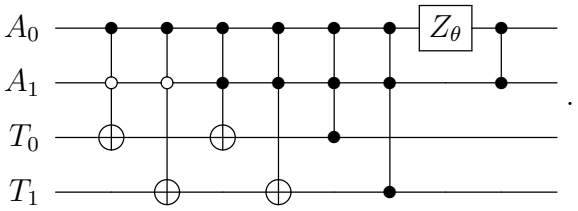
Note that the angle ϕ_1 entering Eq. (2.4.22) coincides with Eq. (2.4.12).

With the select mapping (2.4.19), the corresponding circuit to the *select* unitary is displayed as



(2.4.23)

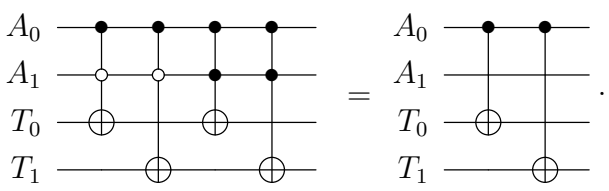
where A_0 and A_1 represent the first and second ancilla qubit and T_0 and T_1 represent the target qubits. Here, Z_θ (defined in Eq. (2.4.15)) accounts for the sign of the cosine for $\theta > \pi/2$. To simplify, we use the identity $X_0Z_0X_1Z_1 = -Y_0Y_1$, and obtain the *select* circuit as



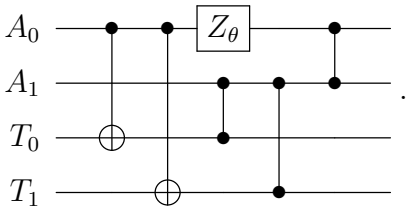
(2.4.24)

The last CZ gate (defined in Eq. (A.6)) is used to correct the sign of the Y_0Y_1 term.

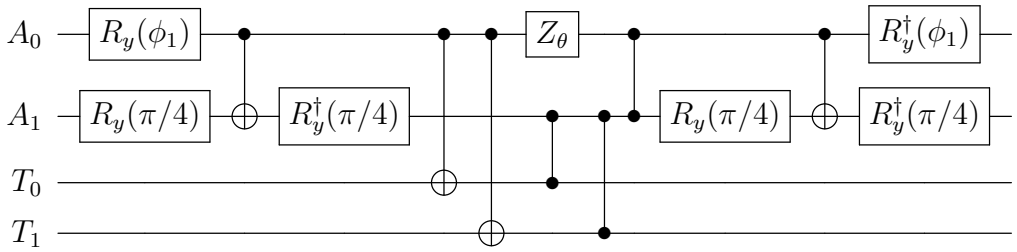
After the decomposition of this circuit, according to the optimal decomposition presented in Ref. (Shende and Markov, 2009), six CNOT gates per Toffoli are required. This is not optimal that we can manually simplify the circuit. Notice that the state $|01\rangle_a$ in the mapping Eq. (2.4.19) is not in use, that the state $|11\rangle_a$ can be recognized by only recognizing A_1 to be $|1\rangle_a$. Thus, the implementation of two CCZ gates is reduced to two CZ gates (remove the controls on the first ancilla qubit) for the fifth and sixth gates. Furthermore, the second and third gates in Circuit (2.4.24) commute. This gives us



Then the resulting circuit for *select* becomes

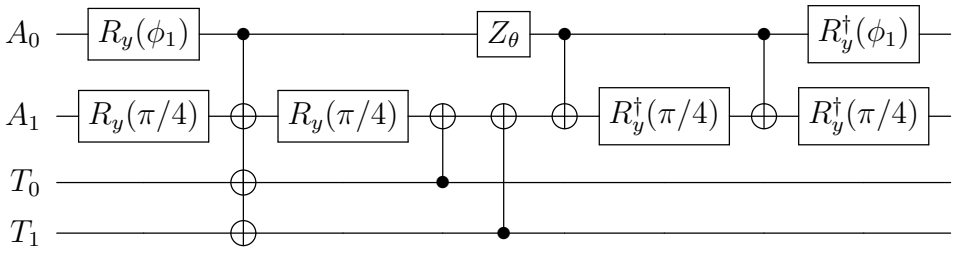


In summary, the full circuit needed for the LCU implementation of the operator in Eq. (2.4.16) is as circuit (2.4.25)



(2.4.25)

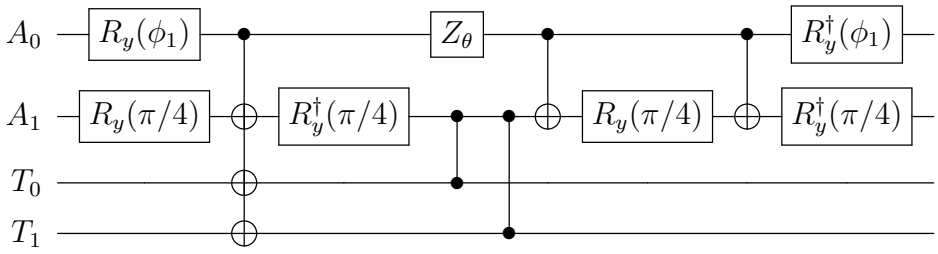
I use the identity Eq. (A.4) to decompose the two CH gates in *prepare* unitary and inverse of *prepare* unitary. To change the implementation with CZ gates to the implementation with CNOT gates, I use the identity (see circuit (A.7)) three times. The first line of circuit (A.7) can be the target qubit T_0 and T_1 and ancilla qubit A_0. Then, the simplified circuit is shown as follows:



(2.4.26)

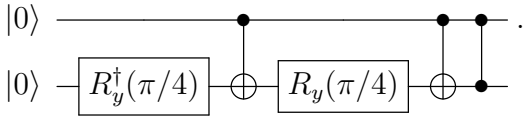
In total, the circuit (2.4.26) needs 7 CNOT gates and 7 rotations. Furthermore, I can reduce one additional CNOT with another decomposition of the CH gate (second line of

circuit (A.8)) and take the inverse. The full circuit is depicted as follows



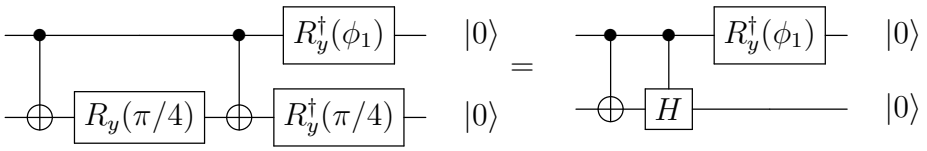
(2.4.27)

The fourth CNOT gate can be eliminated. Let us look into the second line of circuit (A.8), i.e., the circuit as follows



Notice that after applying the circuit, the second qubit is in an eigenstate of the Pauli X operator when the first qubit is in state $|1\rangle$. This implies that adding another CNOT (to cancel the second CNOT gate) is just changing a global irrelevant phase. The same is true if one measures the projector in the second ancilla qubit state $|0\rangle$ instead.

To be more clear, let us look at the last part of circuit (2.4.27).

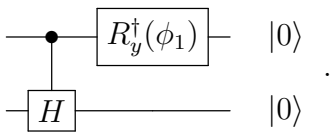


(2.4.28)

The $|0\rangle$ state on the right-hand side means postselecting the state being in state $|0\rangle$. If one applies this circuit onto a state $a|00\rangle + b|01\rangle + c|10\rangle + d|11\rangle$, the result is

$$R_y^\dagger|0\rangle\left(a|0\rangle + b|1\rangle\right) + R_y^\dagger|1\rangle\left(\frac{c+d}{2}|0\rangle + \frac{-c+d}{2}|1\rangle\right).$$

If omitting the first CNOT, the circuit becomes

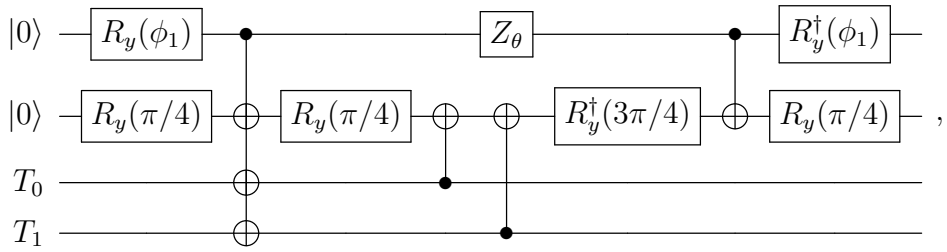


(2.4.29)

The result becomes

$$R_y^\dagger |0\rangle (a|0\rangle + b|1\rangle) + R_y^\dagger |1\rangle \left(\frac{c+d}{2}|0\rangle + \frac{c-d}{2}|1\rangle \right) .$$

For the reason that the measurement is postselecting the ancilla qubit being in the $|00\rangle$, the minus sign can be ignored for the second ancilla qubit when it is in state $|1\rangle$. Finally, the circuit is shown as follows



(2.4.30)

which requires 6 CNOTs and 7 rotation gates.

2.5 Results of a Simple Excitation Operator

This section provides the implementation of both the time-dependent method and the LCU-based method by using the simple excitation operator

$$\hat{O}(\theta) = \cos(\theta)X + \sin(\theta)\mathbb{I} . \tag{2.5.1}$$

Two different metrics are introduced to analyze the performance. Let us consider a set of N_O independent observables. The first metric is the chi squared, denoted as

$$\chi^2 = \sum_{k=1}^{N_O} \frac{\left(v_k^{(e)} - v_k^{(t)}\right)^2}{\left(\varepsilon_k^{(e)}\right)^2} , \tag{2.5.2}$$

where $v_k^{(t)}$ and $v_k^{(e)}$ are the theoretical and experimental value for the kth observable, and $\varepsilon_k^{(e)}$ is the estimated error of computation models. We expect χ^2 to be close to one to indicate the experimental results are compatible with theoretical results within the estimated error.

The second metric is the normalized sum of squared deviations (nssd),

$$\text{nssd}(r) = \sqrt{\frac{\sum_{k=1}^{N_O}\left(v_k^{(e)} - v_k^{(t)}\right)^2}{\sum_{k=1}^{N_O}\left(r v_k^{(t)}\right)^2}}\,, \tag{2.5.3}$$

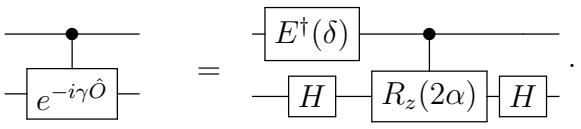
quantifies the accuracy of the calculation. The parameter r is tuned to control the percentage of expected values as the reference, and in this dissertation, $r = 0.1$ is used, and nssd $\equiv$ nssd(0.1) is used for simplicity. For good results, nssd is expected to be close to zero, which indicates that the relative error is much smaller than 10% of the theoretical values. To summarize, the χ^2 and nnsd are used to evaluate the variability and accuracy of the results with respect to the expected result.

2.5.1 Time-dependent Method

This subsection presents the results for state preparation of a simple excitation operator, introduced as Eq. (2.5.1), with the time-dependent method. The time evolution operator is defined as

$$\begin{aligned} e^{-i\gamma\hat{O}} &= e^{-i\gamma(\cos(\theta)X + \sin(\theta)\mathbb{I})} \\ &= e^{-i\gamma\sin(\theta)} R_x\left[2\gamma\cos(\theta)\right]\,. \end{aligned} \tag{2.5.4}$$

This time evolution operator can be implemented exactly on a quantum computer, and I use the first method introduced in Sec. 2.4.1, i.e., the controlled time-evolution operator is implemented by successive controlled rotation operators. Therefore, the controlled unitary is expressed as

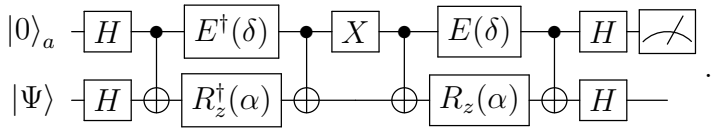


(2.5.5)

Here $\delta = \gamma\sin\theta$, and $\alpha = \gamma\cos\theta$. Here the identity $R_x(\theta) = HR_z(\theta)H$ is used to transform implementation of R_x to R_z. Also, the controlled-H is ignored and replaced with gate H since if the ancilla qubit is in state $|0\rangle_a$, then gates $HH = \mathbb{I}$ will be applied on the target

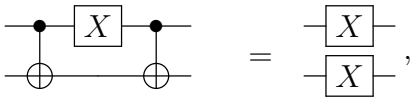
qubit; and if the ancilla qubit is in state $|1\rangle_a$, then gates $HR_z(2\alpha)H = R_x(2\alpha)$ will be applied, which works the same as controlled-R_x gate. This technique will be applied later frequently. Here, the subscript a denotes ancilla qubits to avoid confusion with states of target qubits.

Then we use the simplification (2.4.4) for controlled-R_z gate, and get the complete circuit



(2.5.6)

Looking into this circuit, we could find the simplification that



(2.5.7)

and simplify $R_z X R_z^\dagger$ into two one-qubit gates, the same for $EXE^\dagger$, then the implementation only needs two CNOTs and eight one-qubit gates. This simplification is not presented in the Ref. (Roggero et al., 2020a), so the results in the main text are given with circuit (2.5.6) only. Therefore, the full state preparation circuit (2.5.6) is implemented using four CNOT gates, four Z-rotations, and five additional single-qubit gates.

In Sec. 2.2.1, I discussed the fidelity and success probability for this excitation operator. Setting the time parameter as $\gamma = 0.3$, the corresponding fidelity and success probabilities analysis is depicted in Fig. 2.2 and the bounds are obtained as $9\% \geq P_s(0.3) \geq 8.46\%$ and $F(0.3) \geq 97\%$, and this is a relatively good balance between the success probability and fidelity tradeoffs. Therefore, $\gamma = 0.3$ is used in the implementation.

The implementation of the circuit requires two qubits, and qubits 1 and 2 of Vigo (which have full connectivity) are chosen; see the layout of the IBM *Quantum* backend Vigo in Fig. 2.1. The computations are executed on both VM and QPU, and the results of success probabilities P_s are given in Fig. 2.3. The green line denotes the exact results obtained from Eq. (2.2.8), and the band represents the analyzed upper and lower bound for success probability. The black circles and red squares represent the results with and without error mitigation procedures, respectively.

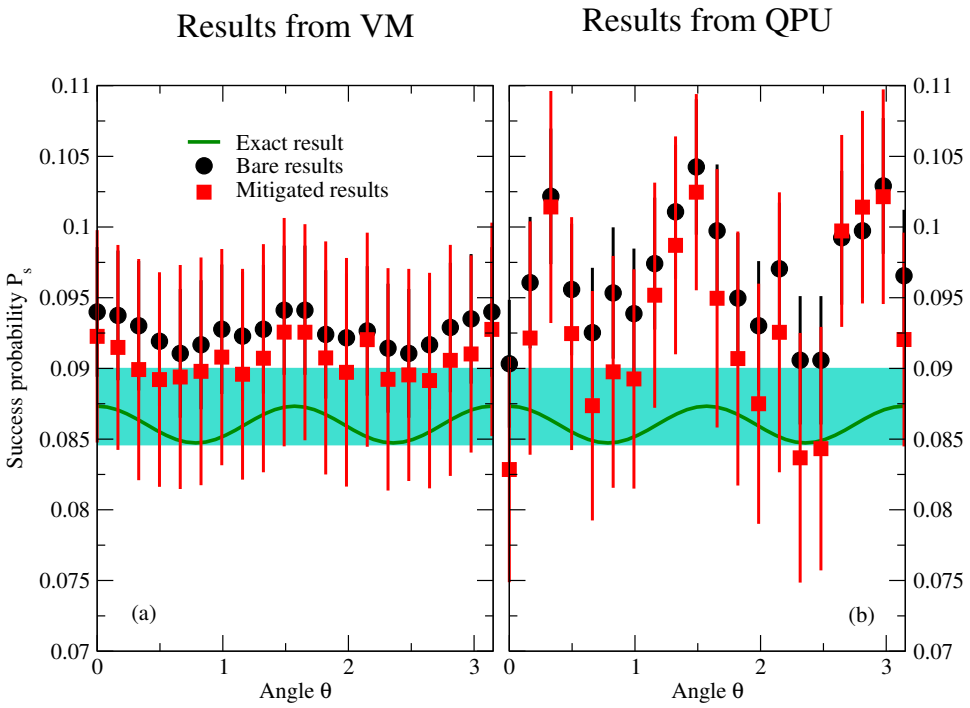


Figure 2.3: Success probability P_s for the time-dependent method versus the parameter θ in excitation operator Eq. (2.5.1) with VM simulations (left panel) and QPU runs (right panel). Results are given with (red squares) and without (black circles) full mitigation and with exact analysis (green lines) from Eq. (2.2.8). The band gives the analyzed bound $9\% \geq P_s(0.3) \geq 8.46\%$. The figure is taken from Ref. (Roggero et al., 2020a), which I co-authored.

The errors in the VM results are not random, and mitigation procedures help reduce them. For the QPU results, the noise is significant, and mitigation procedures do not help much. Quality metrics help show these more clearly. Tab. 2.1 gives the quality metrics for the results on the success probability. Here, "bare" represents the result directly from runs, "RO mit." represents read-out (RO) error mitigated results (using readout correction), and "full mit." represents fully mitigated results (using readout correction and error extrapolation).

We see that VM results are improved by the error mitigation methods, both readout correction and error extrapolation. For QPU results, the nssd results approximate 1, which indicates that the QPU results differ from the exact results by 10%, with or without the mitigation procedure. Error mitigation cannot improve the accuracy of results. Notice that χ^2 of those error mitigated values for the QPU calculation is reduced, which means the read-out error correction and error extrapolation procedures help reduce the variability of results.

To investigate the fidelity of the algorithm, an estimator is used, written as

$$\begin{aligned} P_t &\equiv |\langle \Psi_A|1\rangle|^2 \\ &= \frac{|\langle 00|V(\gamma)|11\rangle|^2}{|\langle 00|V(\gamma)|11\rangle|^2 + |\langle 00|V(\gamma)|01\rangle|^2} \\ &= \frac{|\langle 00|V(\gamma)|11\rangle|^2}{P_s(\gamma)} \,, \end{aligned} \tag{2.5.8}$$

which is the transition probability of initial state $|0\rangle$ onto final state $|1\rangle$. The unitary $V(\gamma)$ is given in Eq. (2.2.5), $P_s(\gamma)$ is the empirical success probability. The state $|n_1 n_2\rangle$ is a simplified form of $|n_1\rangle_a \otimes |n_2\rangle$, with the first digit representing the state for the ancilla qubit and the second representing the target qubit. With this estimator, we can study the fidelity of the prepared state $|\Psi_A\rangle$ from Eq. (2.2.7). This ratio estimator for transition probabilities is more error resilient to depolarizing noise (explained in Appendix G in Ref. (Roggero et al., 2020a)).

The results of transition probability P_t with VM simulations and QPU runs are shown in the left and right panels of Fig. 2.4, respectively. The quality metrics χ^2 and nssd are shown in Tab. 2.2. The exact results, denoted with green lines, are calculated from Eq. (2.5.8).

Table 2.1: Quality metrics χ^2 and nssd for success probability P_s with (a) VM simulations and (b) QPU runs for the time-dependent method. The bare results (bare), results with read-out error correction (RO mit.), and results with full error mitigation (full mit.) are shown.

(a) VM

	χ^2	nssd
bare	2.08	0.765
RO mit.	1.46	0.656
full mit.	0.37	0.539

(b) QPU

	χ^2	nssd
bare	5.64	1.299
RO mit.	3.00	1.004
full mit.	1.47	1.052

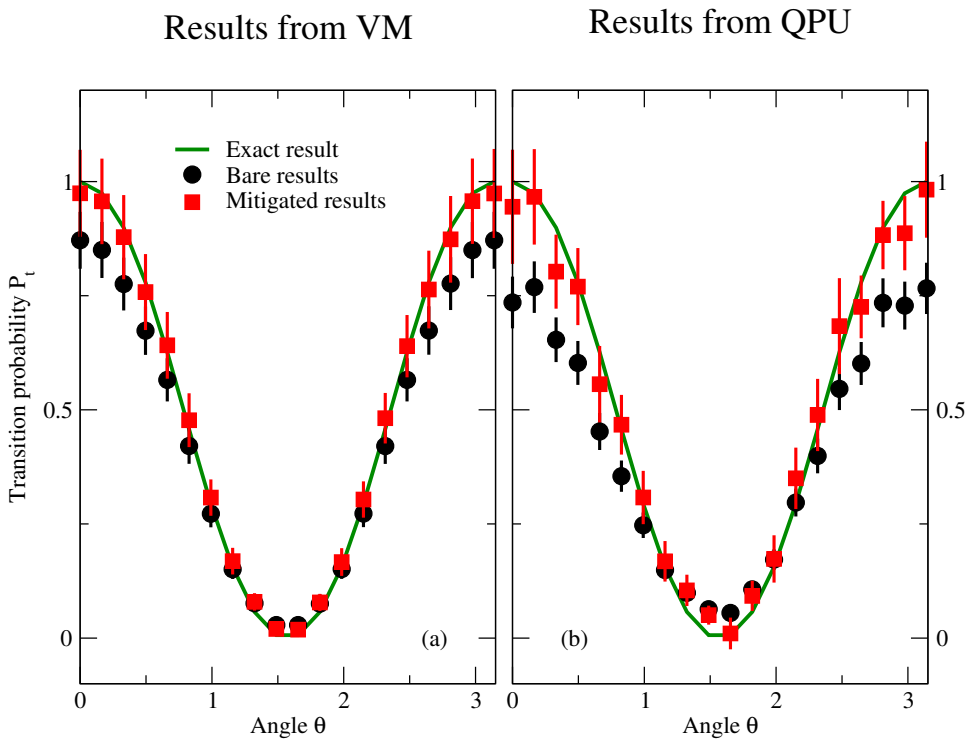


Figure 2.4: Transition probability P_t versus the parameter θ with VM simulations (left panel) and QPU runs (right panel) for the time-dependent method. Results are given with (red squares) and without (black circles) full mitigation and with exact analysis (green lines) from Eq. (2.5.8). The figure is taken from Ref. (Roggero et al., 2020a), which I co-authored.

Table 2.2: Quality metrics χ^2 and nssd for the transition probability obtained from (a) VM simulations and (b) QPU runs for time-dependent method. The bare results (bare), results with read-out error correction (RO mit.), and full error mitigation (full mit.) are shown.

(a) VM

	χ^2	nssd
bare	2.80	1.259
RO mit.	0.87	0.757
full mit.	0.39	0.386

(b) QPU

	χ^2	nssd
bare	11.27	2.324
RO mit.	3.19	1.059
full mit.	0.65	0.718

The black circles and red squares represent the results with and without error mitigation procedures, respectively.

For QPU results, nssd ≈ 0.7 indicates mitigated results differ from the exact ones by 7%, and χ^2 drops and close to 1 indicates the mitigated results become more compatible with the exact result within the estimated error. The mitigation procedures help improve the accuracy and variability of QPU results. Overall, by combining the analysis of success probability, we can see that the time-dependent method runs on QPU with reasonable efficiency.

2.5.2 LCU-based Method

For the simple excitation operator, Eq. (2.5.1), the state preparation procedure can easily be implemented with the LCU-based method; see the circuit (2.4.14). This circuit is too simple to evaluate the performance of the LCU-based method that an alternative excitation operator is considered

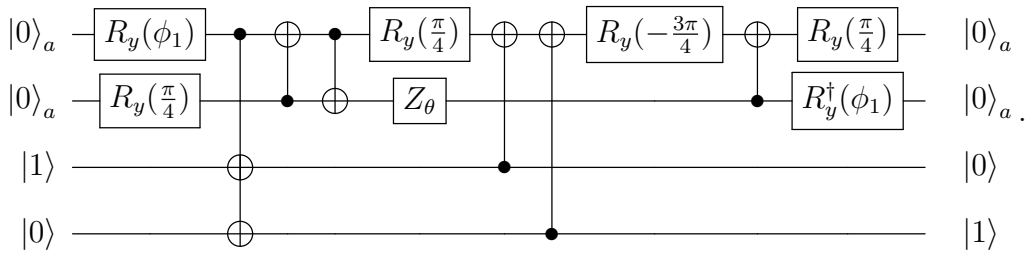
$$\widetilde{O}(\theta) = \sin(\theta)(c_1^\dagger c_1 + c_0^\dagger c_0) + \cos(\theta)(c_0^\dagger c_1 + c_1^\dagger c_0) \ , \tag{2.5.9}$$

which is the second quantization form of Eq. (2.5.1). After the Jordan-Wigner transformation, with Eq. (2.4.17), the second quantized operator is mapped to Pauli matrices as Eq. (2.4.18).

The state preparation for this operator is implemented with circuit (2.4.30) (see in Sec. 2.4.2 for a full derivation). Here, the ancilla qubits are initialized in state $|0\rangle_a \equiv |00\rangle$ and postselected onto finial state $|0\rangle_a$. For practice, the quantum register is prepared in the initial state of the quantum system, $|10\rangle$, and is mapped to the final state of the quantum system, $|01\rangle$.

It is important to note the full connectivity of those four qubits in circuit (2.4.30). If we assume an all-to-all connectivity quantum device, the implementation of the entire circuit requires only six CNOT gates and seven single qubit gates. While the quantum device Vigo (5qubit backed: IBM Q team, 2020) has limited connections, the implementation requires SWAP gates (see Appendix A for definition) to interchange two qubits that make the connectivity established. Apply a SWAP gate between the A_0 ancilla qubit and the A_1

ancilla qubit, the circuit (2.5.2) with right connectivity is obtained, shown as follows



Then Vigo's qubits 1, 0, 3, and 2 are used to execute the ancilla register A_0, A_1, and quantum register T_0, T_1, respectively.

The results of success probability P_s obtained from VM simulations and QPU runs are shown in the left and right panel in Fig. 2.5, and the quality metrics χ^2 and nssd are shown in Tab. 2.3. The comparison with Fig. 2.3 indicates that the LCU-based method has a much higher success probability than the time-dependent method. For QPU results, error mitigation significantly improves the variability of results, which reduces the χ^2 by two orders of magnitude.

Two estimators are designed for the transition probability P_t. The first estimator $P_t^A(\theta)$ is,

$$P_t^A(\theta) = \Lambda^2(\theta)\,\mathrm{Tr}\left[|\Omega\rangle\langle\Omega|\Pi_0\otimes|\psi_f\rangle\langle\psi_f|\right] \ , \tag{2.5.10}$$

which is the transition probability onto final state $|\psi_f\rangle = |01\rangle$. Here, the state $|\Omega\rangle \equiv |\Omega(\theta)\rangle$ is given in Eq. (2.3.5), $\Pi_0 \equiv |0\rangle_a \langle 0|_a$ is the projector operator for ancilar register. $\Lambda(\theta)$ is the success probability as $\eta = 1$ in the success probability (see Eq. (2.3.8)). The second estimator $P_t^B(\theta)$ is given as

$$P_t^B(\theta) \equiv \frac{\mathrm{Tr}\left[|\Omega\rangle\langle\Omega|\Pi_0\otimes|\psi_f\rangle\langle\psi_f|\right]}{\mathrm{Tr}\left[|\Omega\rangle\langle\Omega|\Pi_0\otimes\mathbb{I}\right]} \ . \tag{2.5.11}$$

Instead of rescaling with the theoretical success probability as in P_t^A, P_t^B is rescaled with $\mathrm{Tr}\left[|\Omega\rangle\langle\Omega|\Pi_0\otimes\mathbb{I}\right]$, i.e., the empirical success probability. If there are no systematic errors, P_t^A should be equivalent to P_t^B.

The results of transition probability P_t^A and P_t^B are presented in the lower panel and upper panel of Fig. 2.6. And quality metrics χ^2 and nssd are shown in Tab. 2.4. Comparing

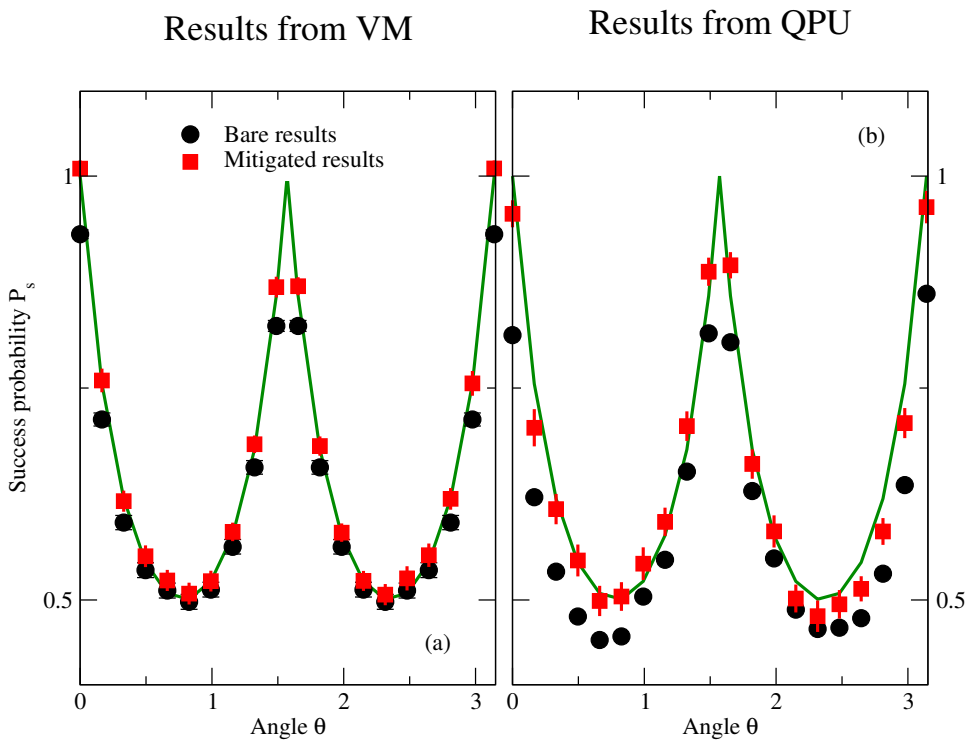


Figure 2.5: Success probability P_s versus angle θ in operator Eq. (2.4.18), obtained from VM simulations (left panel) and QPU runs (right panel) for the LCU-based method. Results are given with (red squares) and without (black circles) full mitigation and with exact analysis (green lines) from Eq. (2.3.8). The figure is taken from Ref. (Roggero et al., 2020a), which I co-authored.

Table 2.3: Quality metrics χ^2 and nssd of the success probability obtained from (a) VM simulations and (b) QPU runs for the LCU-based method. The bare results (bare), results with read-out error correction (RO mit.), and full error mitigation (full mit.) are shown.

(a) VM

	χ^2	nssd
bare	26.52	0.453
RO mit.	3.63	0.211
full mit.	0.44	0.118

(b) QPU

	χ^2	nssd
bare	112.56	1.190
RO mit.	70.17	1.085
full mit.	2.61	0.415

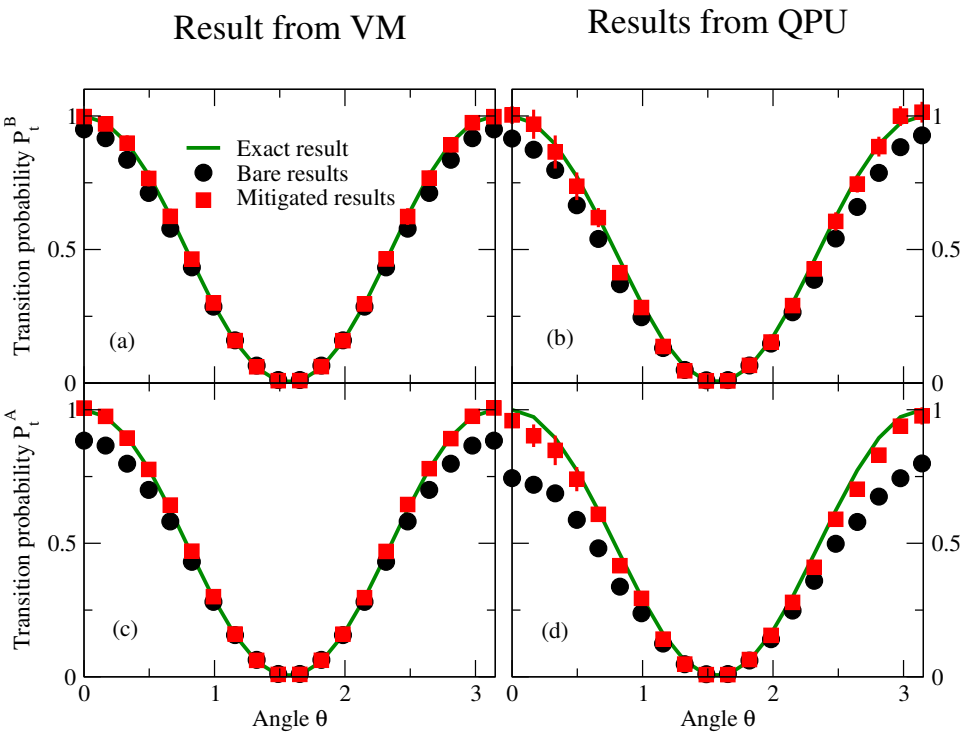


Figure 2.6: Results for the transition probabilities P_t^A (lower panel) and P_t^B (upper panel) versus the angle θ in excitation operator Eq. (2.4.18), obtained from VM simulations (left panel) and QPU runs (right panel) and exact analysis (green lines) for the LCU-based method. The figure is taken from Ref. (Roggero et al., 2020a), which I co-authored.

Table 2.4: Quality metrics χ^2 and nssd of transition probabilities P_t^A and P_t^Bobtained from (a) VM simulations and (b) QPU runs for the LCU-based method. The bare results (bare), results with read-out error correction (RO mit.), and full error mitigation (full mit.) are shown.

(a) VM

	$\chi^2(P_t^A)$	$\chi^2(P_t^B)$	nssd(P_t^A)	nssd(P_t^B)
bare	76.20	10.09	1.022	0.623
RO mit.	6.57	0.29	0.321	0.106
full mit.	0.29	0.12	0.129	0.053

(b) QPU

	$\chi^2(P_t^A)$	$\chi^2(P_t^B)$	nssd(P_t^A)	nssd(P_t^B)
bare	251.70	23.00	2.367	1.151
RO mit.	109.78	4.51	1.661	0.487
full mit.	2.48	1.13	0.580	0.326

these two estimators, P_t^B has much better bare results, with smaller χ^2 and nssd. This indicates that the ratio estimator P_t^B is more resilient to depolarizing noise (explained in Appendix G in Ref. (Roggero et al., 2020a)). Also, error mitigation works significantly well, especially for estimator P_t^A. The bare QPU results are off by about 24% (nssd ≈ 2.4) but full mitigation procedures bring the error to around 6% (nssd ≈ 0.6). Also, χ^2 is reduced by two orders of magnitude for the P_t^A and down to values around one for the P_t^B. As seen in Fig. 2.6, the bare result at $\theta \approx 0$ and $\theta \approx \pi$ are evidently improved by the error mitigation procedures.

In this section, both the time-dependent method and the LCU-based methods are utilized to execute excited state preparation for the first (Eq. (2.5.1)) and second quantization (Eq. (2.4.18)) form of the simple excitation operator. The jobs are run on both VM simulators and real quantum devices, and the results show that both techniques are efficient and useful for state preparation. The LCU-based method is more efficient and resilient to error if we use ratio estimators like Eq. (2.5.11).

2.6 Results of $n(p,d)\gamma$ Reaction

This section shows the application of state preparation algorithms to a simple model for $n(p,d)\gamma$ reaction, which describes a process in which a proton captures a neutron to form a deuteron and emits a photon. It is one of the most important nuclear syntheses and is a key step in big-bang nucleosynthesis (Adelberger et al., 2011). The dominant process for this reaction is from the continuum ${}^1S_0$ state (with spin isospin $T = 1$, $T_z = 0$) to the deuteron bound state (only consider the leading order as state ${}^3S_1$ with spin isospin $T = T_z = 0$). Thus, the electromagnetic transition is of $M1$ multipole order, and the excitation operator [for the detailed explanation of operator construction, I refer readers to Appendix C in Ref. (Roggero et al., 2020a)] is defined as

$$O(\theta') = \alpha\mathbb{I} + \beta X + \gamma Z = \begin{pmatrix} \alpha+\gamma & \beta \\ \beta & \alpha-\gamma \end{pmatrix}, \tag{2.6.1}$$

which is in the basis of the state ${}^1S_0$ (represented by state $|0\rangle$) and the state ${}^3S_1$ (represented by state $|1\rangle$). The three real constants are given by

$$\begin{aligned}
\alpha &= \sin(\theta')\frac{g_p + g_n}{4}\mu_N \ , \\
\beta &= \frac{\mu_N}{2\sqrt{2}}(g_p - g_n)\cos(\theta') \ , \\
\gamma &= -\sin(\theta')\frac{g_p + g_n}{4}\mu_N \ .
\end{aligned}$$

The nuclear magneton μ_N is set as $\mu_N = 1$ in the dissertation since the operator can be rescaled with any constant. $g_p = 5.586$ and $g_n = -3.826$ denote the proton and neutron g factors, respectively. Noted that

$$\alpha = -\gamma \geq 0$$

and

$$\beta \begin{cases} \geq 0 & \text{if } \theta' \in [0, \pi/2] \\ < 0 & \text{if } \theta' \in (\pi/2, \pi] \end{cases} .$$

The second quantized form of Eq. (2.6.1) (use the face $\alpha + \gamma = 0$) is given as

$$\widetilde{O} = 2\alpha c_1^\dagger c_1 + \beta(c_0^\dagger c_1 + c_1^\dagger c_0) \ . \tag{2.6.2}$$

The creation (annihilation) operator $c_0^\dagger$ (c_0) creates (annihilates) the angular momentum state ${}^1S_0$. The creation (annihilation) operator $c_1^\dagger$ (c_1) creates (annihilates) the angular momentum state ${}^3S_1$. In this basis, the initial state of the nuclear system is $|10\rangle$, and the final state is $|01\rangle$. After the Jordan-Wigner transformation Eq. (2.4.17), the operator is transformed as a sum of Pauli strings, written as:

$$\begin{aligned}
\widetilde{O} &= \alpha\mathbb{I} + \frac{\beta}{2}(X_0X_1 + Y_0Y_1) + \alpha Z_1 \\
&= \begin{pmatrix} 2\alpha & 0 & 0 & 0 \\ 0 & 0 & \beta & 0 \\ 0 & \beta & 2\alpha & 0 \\ 0 & 0 & 0 & 0 \end{pmatrix} .
\end{aligned} \tag{2.6.3}$$

Note that another form is available

$$\begin{aligned}\overline{O} &= \alpha\mathbb{I} + \frac{\beta}{2}(X_0X_1 + Y_0Y_1) - \frac{\alpha}{2}(Z_0 - Z_1) \\ &= \begin{pmatrix} \alpha & 0 & 0 & 0 \\ 0 & 0 & \beta & 0 \\ 0 & \beta & 2\alpha & 0 \\ 0 & 0 & 0 & \alpha \end{pmatrix} ,\end{aligned} \tag{2.6.4}$$

where we use the second quantization operator as $\widetilde{O} = \alpha\mathbb{I} + \beta(c_0^\dagger c_1 + c_1^\dagger c_0) + \gamma(c_0^\dagger c_0 - c_1^\dagger c_1)$, then use the fact $\alpha + \gamma = 0$. The *seclect* operator for Eq. (2.6.3) needs two ancilla qubits and three ancilla qubits for Eq. (2.6.4). The reason we introduce (2.6.4) is that additional ancilla qubits can help reduce the length of the circuit, and this will be discussed at the end of Subsec. 2.6.1.

To increase the density of points in the region around $\pi/2$ where the cross section drops to zero, we chose to implement instead the simpler operator

$$\begin{aligned}\overline{O}_M(\theta) = \sin(\theta)\mathbb{I} &+ \frac{\cos(\theta)}{2}(X_0X_1 + Y_0Y_1) \\ &- \frac{\sin(\theta)}{2}(Z_0 - Z_1) ,\end{aligned} \tag{2.6.5}$$

for uniformly spaced values of the angle θ. The original excitation operator is then obtained as

$$\overline{O} = \sqrt{\alpha^2 + \beta^2}\, \overline{O}_M(\phi_{\alpha\beta}) \quad \phi_{\alpha\beta} = \arctan\left(\frac{\alpha}{\beta}\right) . \tag{2.6.6}$$

Note that since every observable we compute is independent on a global scale factor like $\sqrt{\alpha^2 + \beta^2}$, we only need to perform the change of variables in the angle.

The applications of the excitation operators with both the first quantization form and the second quantization form (more scalable in a nuclear system) are considered. Next, I show the circuit details for both quantization forms with the time-dependent method and the LCU-based method.

2.6.1 Circuit Implementation Details

This subsection provides the circuit implementation details for the nuclear excitation operator in the first quantized form for both the time-depend method and the LCU-based method, and the circuit implementation details for the second quantized form [$\overline{O}_M(\theta)$ in Eq.(2.6.5)] for the LCU-based method.

First Quantized Case

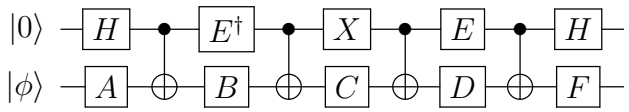
First, consider using the time-depend method to approximate the action of the first quantized operator

$$O(\theta) = \alpha\mathbb{I} + \beta X - \alpha Z \ . \tag{2.6.7}$$

The corresponding time evolution operator and its Euler decomposition are given as

$$e^{-i\gamma O} = e^{-i\delta} R_z(x_1) R_y(x_2) R_z(x_3) \ .$$

The three angles x_1, x_2, and x_3, and phase δ are introduced in Sec. 2.4.1. I use the general state preparation circuit (2.4.10),



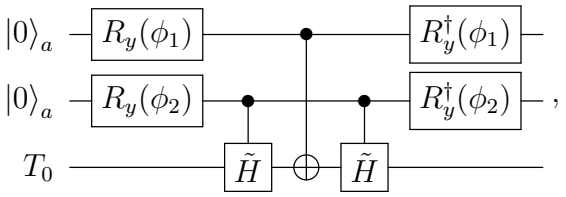
. (2.6.8)

Gate A and B are defined in Eq. (2.4.8). Gate C, D and F are defined in Eq. (2.4.11). And gate E is defined in Eq. (2.4.6). Therefore, the circuit needs four CNOTs and ten additional single qubit rotations.

Then, I show the circuit implementation details for Eq. (2.6.7) by using the LCU-based method. The mapping for *select* unitary is shown as follows

$$|00\rangle_a \to \mathbb{I} \quad |01\rangle_a \to \mathbb{I} \quad |10\rangle_a \to X \quad |11\rangle_a \to -Z \ . \tag{2.6.9}$$

For the case $\beta \geq 0$, the full circuit is given as,

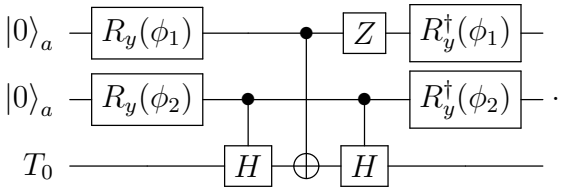


(2.6.10)

where $\tilde{H} = R_y^\dagger(3\pi/4)XR_y(3\pi/4)$. The identity $\tilde{H}X\tilde{H} = -Z$ is used in the third line. The angles are

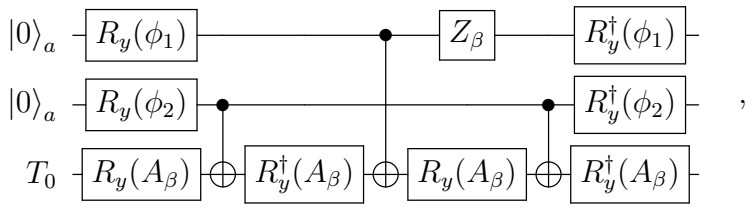
$$\begin{aligned} \phi_1 &= 2\arcsin\left(\sqrt{\frac{\alpha+|\beta|}{2\alpha+|\beta|}}\right), \\ \phi_2 &= 2\arcsin\left(\sqrt{\frac{\alpha}{\alpha+|\beta|}}\right). \end{aligned} \tag{2.6.11}$$

For the case $\beta \leq 0$, the full circuit is given as



(2.6.12)

the Hadamard gate H (modulo a phase) is defined as $H = R_y(3\pi/4)XR_y^\dagger(3\pi/4)$, and the identity $HXH = Z$ is used. The gate Z is introduced to make up the negative sign in Eq. (2.6.7). Combine both cases, and the final circuit is shown in the circuit (2.6.13),



(2.6.13)

where similarly to Eq. (2.4.15) we use

$$Z_\beta \equiv \begin{cases} \mathbb{I} & \text{for} \quad \beta \geq 0 \\ Z & \text{for} \quad \beta < 0 \end{cases}, \tag{2.6.14}$$

and

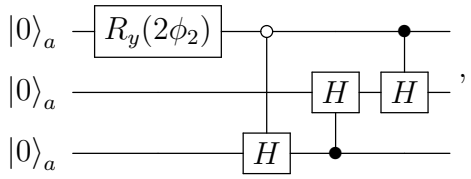
$$A_\beta = \begin{cases} \frac{3\pi}{4} & \text{for} \quad \beta \geq 0 \\ \frac{-3\pi}{4} & \text{for} \quad \beta < 0 \end{cases} . \tag{2.6.15}$$

Second Quantized Case

First, the detailed circuit implementation for the second quantized nuclear excitation operator $\overline{O}_M(\theta)$, introduced in Eq.(2.6.5), with the LCU-based method is conveyed. As $\overline{O}_M(\theta)$ is a summation of $L = 5$ unitaries, we need three ancilla qubits, and the corresponding mapping is

$$\begin{gathered} |000\rangle_a \to \mathbb{I} \quad |001\rangle_a \to Z_1 \quad |011\rangle_a \to -Z_0 \\ |100\rangle_a \to X_0X_1 \quad |110\rangle_a \to Y_0Y_1 \ . \end{gathered} \tag{2.6.16}$$

The number subscript of unitaries denotes the qubit they work on. The circuit of *prepare* unitary is depicted in circuit (2.6.17)



, (2.6.17)

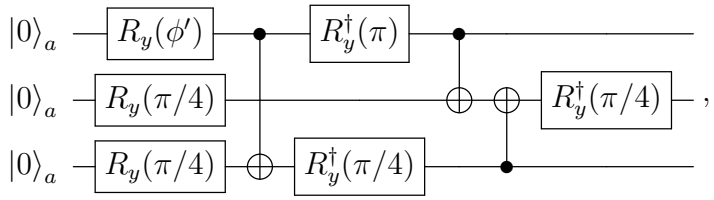
with the angle

$$\phi_2 = \arcsin\left(\sqrt{\frac{|\cos(\theta)|}{2\sin(\theta) + |\cos(\theta)|}}\right) . \tag{2.6.18}$$

This circuit produces a state as

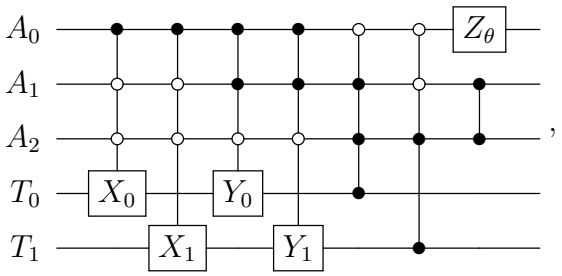
$$\begin{aligned} |\Phi_3\rangle = &\frac{\cos(\phi_2)}{\sqrt{2}}\left(|000\rangle + \frac{|001\rangle + |011\rangle}{\sqrt{2}}\right) \\ &+ \frac{\sin(\phi_2)}{\sqrt{2}}\left(|100\rangle + |110\rangle\right) \ . \end{aligned} \tag{2.6.19}$$

After decomposing into rotation gates and CNOTs, an explicit implementation of the circuit is depicted as



where $\phi' = 2\phi_2 + \pi$.

The *select* unitary corresponding to the mapping in Eq. (2.6.16) is depicted as



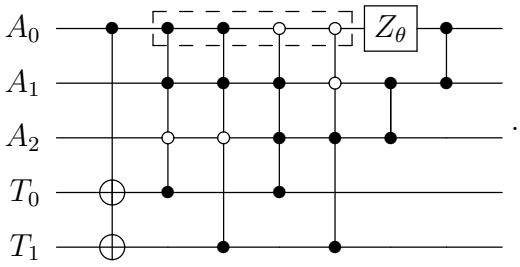
(2.6.20)

with gate Z_θ defined in Eq. (2.4.15) and used to account for the sign associated with $\cos(\theta)$ when $\theta \in [\pi/2, \pi]$, and to recover the relative sign difference between Z_0 and Z_1 in Eq. (2.6.5).

According to Ref. (Barenco et al., 1995), one triple controlled-NOT gate can be decomposed into six CNOTs and seven controlled-unitary gates (which is not an optimally efficient decomposition), one can look into other ways to simplify the circuit implementation manually. Note that in Eq. (2.6.16), three states are not used, and this fact provides us the potential to simplify this circuit further.

First, I use the identity $X_0 Z_0 X_1 Z_1 = -Y_0 Y_1$, transforming those triple controlled-Y gates (the third and fourth gate) into triple controlled-X gates and triple controlled-Z gates. Then, I combine four triple controlled-NOT gates into two CNOTs since we notice that we could recognize states $|100\rangle_a$ and $|110\rangle_a$ by only recognizing the ancilla qubit A_0 being in state

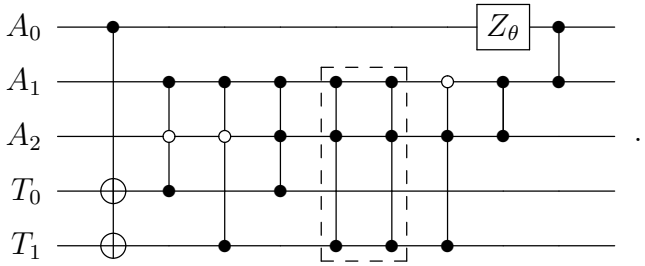
$|1\rangle_a$, and obtain the *select* unitary as



(2.6.21)

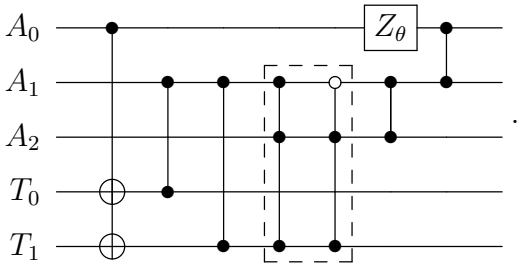
The last CZ gate in circuit (2.6.21) accounts for the minus sign in the identity $X_0Z_0X_1Z_1 = -Y_0Y_1$. A suitable choice of select state could efficiently reduce the number of quantum gates.

The same trick can be used for gates in the dashed box in circuit (2.6.21), i.e., we recognize those controlling states with ancilla qubits A_1 and A_2 only, then the circuit is given as



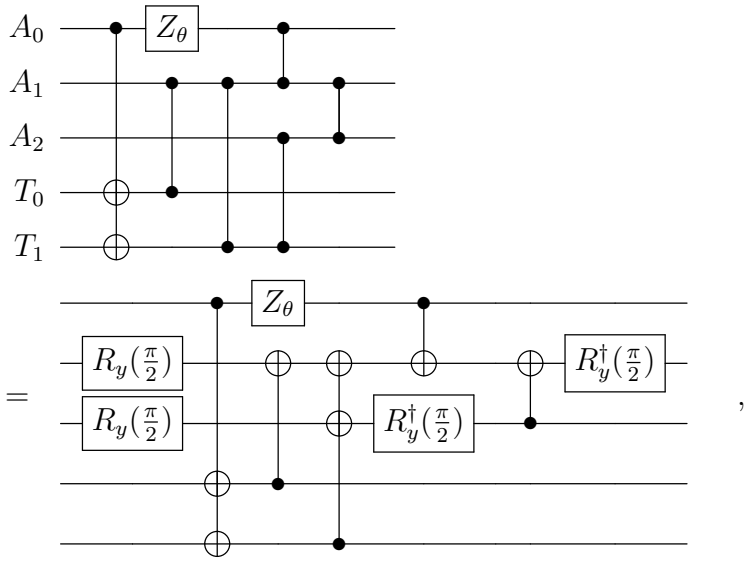
(2.6.22)

I add two redundant CCZ gates in the circuit (2.6.22), shown in the dashed box. Then, the first four CCZ gates in circuit (2.6.22) can be simplified into two CZ gates. The *select* circuit is obtained as



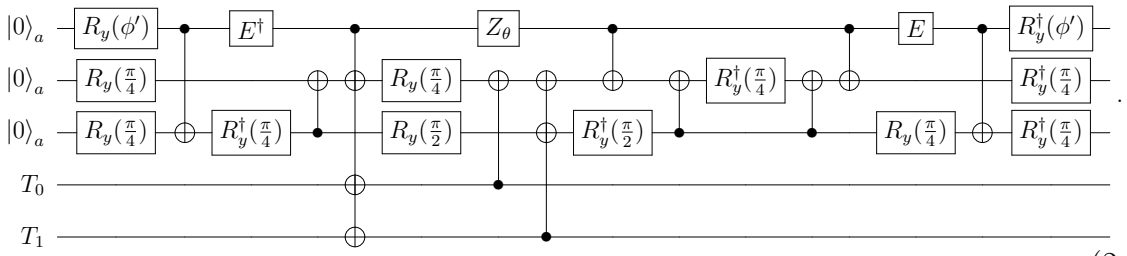
(2.6.23)

Furthermore, the two CCZ gates in dashed box of circuit (2.6.23) can be simplify into CZ gate, which gives circuit (2.6.24)



(2.6.24)

where I use the identity (A.7) to decompose CZs to CNOTs and single-qubit gates. The complete circuit is depicted as circuit (2.6.25), which only needs thirteen CNOT gates,

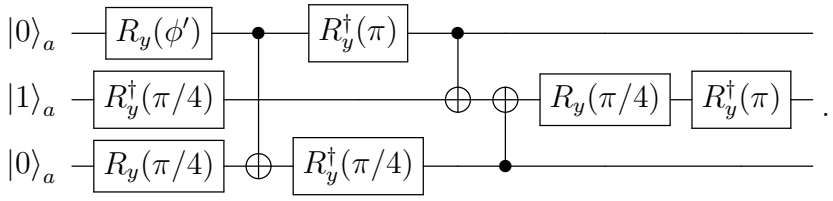


(2.6.25)

This circuit (2.6.25) can be further simplified. Two of the controlled-Z operations can be absorbed by unpreparing the following flag state (slightly different from the previously prepared state)

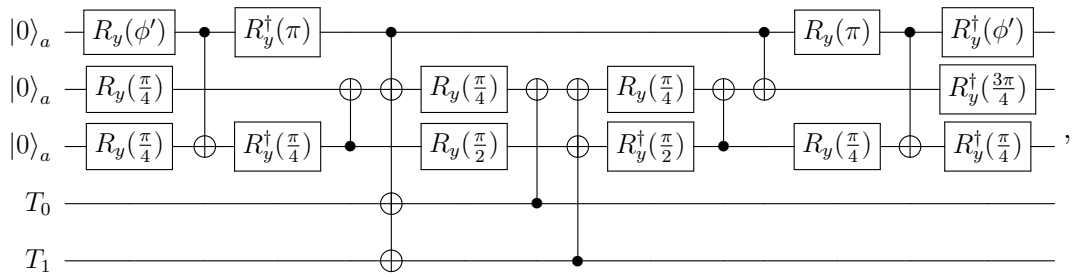
$$\begin{aligned}\left|\widetilde{\Phi}_3\right\rangle = &\frac{\cos(\phi_2)}{\sqrt{2}}\left(|000\rangle_a + \frac{|001\rangle_a - |011\rangle_a}{\sqrt{2}}\right) \\ &+ \frac{\sin(\phi_2)}{\sqrt{2}}\left(|100\rangle_a - |110\rangle_a\right) \ .\end{aligned} \tag{2.6.26}$$

Compared with the former flag state Eq. (2.6.19), applying Z gate to the ancilla qubit A_1 is the only difference. This flag state (2.6.26) can be produced by the circuit



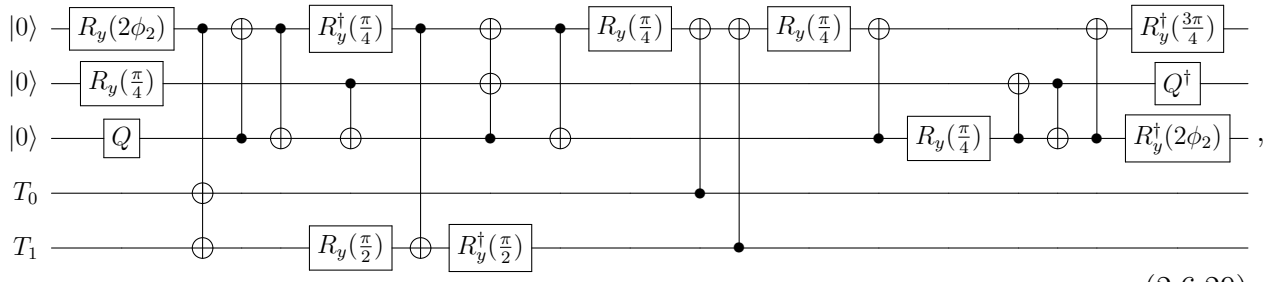
(2.6.27)

Here, the ancilla register A_1 is initialized in $|1\rangle_a$. This scheme is very similar in spirit to the asymmetric qubitization introduced in (Babbush et al., 2019). The total circuit is now given as circuit (2.6.28)



(2.6.28)

which only needs eleven CNOTs. To meet the connectivity requirements for qubits, after applying SWAP gates, the final circuit (2.6.29) is depicted as



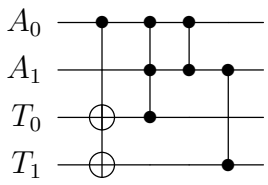
(2.6.29)

which needs fourteen CNOT gates. Here, $Q = R_y(\pi/4)X$.

As I have discussed, the second quantized nuclear operator has another similar form as Eq. (2.6.3), a linear combination of four terms that we need two ancilla qubits. Using the following mapping for the *select* operation:

$$|00\rangle \to \mathbb{I}, \quad |01\rangle \to Z_1, \quad |10\rangle \to X_0X_1, \quad |11\rangle \to Y_0Y_1 \,.$$

After the circuit simplification, the circuit for the *select* is obtained as:



.

Therefore, the circuit only needs six CNOTs (for the simplification of the Toffoli gate) plus four CNOTs, i.e., ten CNOTs in total. The *select* gate only needs seven CNOTs for operator (2.6.5), which indicates that we can use additional qubits for less depth.

2.6.2 Results

Results for First Quantized Case

This section shows the results for the nuclear excitation operator in the first quantized form Eq. (2.6.7) using both the time-dependent method with circuit (2.6.8) and the LCU-based method with circuit (2.6.13). The circuit implementation details are provided in Subsec. 2.6.1.

First, the necessary fidelity and success probability analyses of both methods will be discussed. For the time-dependent method, like the procedure introduced in Sec. 2.5.1. We use the upper and lower bound for success probability, shown in Eq. (2.2.11), and the lower bound for fidelity, shown in Eq. (2.2.12), to carefully choose the time parameter as $\gamma = 0.3$ and obtain

$$\begin{aligned} F(0.3) &\geq 98.8\% \ , \\ 73.8\% \geq P_s(0.3) &\geq 4.5\% \ . \end{aligned} \tag{2.6.30}$$

This is quite a reasonable value for parameter γ as it guarantees high fidelity and relatively high success probability. For the LCU-based method, the fidelity is always 1, and the success probability, shown in Eq. (2.3.8), is guaranteed to be

$$P_s^{\mathrm{LCU}} = \frac{\langle 1|O^2(\theta)|1\rangle}{\Lambda^2} = \frac{\beta^2 + 4\alpha^2}{4\alpha^2 + \beta^2 + 4\alpha|\beta|} \geq 0.5 \ . \tag{2.6.31}$$

Both algorithms were executed on the Vigo QPU (5qubit backed: IBM Q team, 2020) using physical qubits $(1, 2)$ (ancilla in 1 and system in 2) for the time-dependent method and qubits $(2, 3, 1)$ for the LCU-based method. In the latter case, qubits $(2, 3)$ represented ancilla qubits, and qubit 1 was the system. VM simulators are not in use because they are not realistic enough to estimate real quantum devices, as shown in the previous section's results.

The results of success probability and the ${}^1S_0 \to {}^3S_1$ transition probability are presented in the left panel and right panels of Fig. 2.7, and quality metrics χ^2 and nssd for transition probability are shown in Tab. 2.5. The red empty circles in Fig. 2.7 denote those results without self-consistent error extrapolation, and only read-out error correction is executed. Note that this is the only situation in this work where this problem was present; this could be either due to difficulties in executing our specific implementation or could simply be an effect coming from the calibration of the device (the data for the time-dependent method was collected on July 20, 2020, while the LCU data was generated on August 27, 2020). As we can see from the plot, this flagged point does not show any discernible systematic error, and it could also be possible that our flagging procedure is too conservative.

As shown in Fig. 2.7, the success probability for the LCU method is larger than the success probability for the time-dependent method, which satisfies the result in Eq. (2.6.30) and Eq. (2.6.31). The success probability of an algorithm influences the number of statistical samples one can use in calculating the observables. In the region around $\theta = \pi/2$ where success probabilities are close to zero for the time-dependent method, the bare time-dependent results for the transition probability are off by a factor of about 3, and the mitigated results for the transition probability show larger fluctuations. While the LCU-based method has more stable and accurate results for the transition probability, and this is also indicated by Tab. 2.5, the metric nssd for the LCU-based method has a smaller value.

Results for Second Quantized Case

This section shows the results for the nuclear excitation operator in the second quantized form as Eq. (2.6.5), which provides results with higher density around $\theta = \pi/2$, using only the LCU-based method with circuit (2.6.29), which meets the connectivity constraints. The

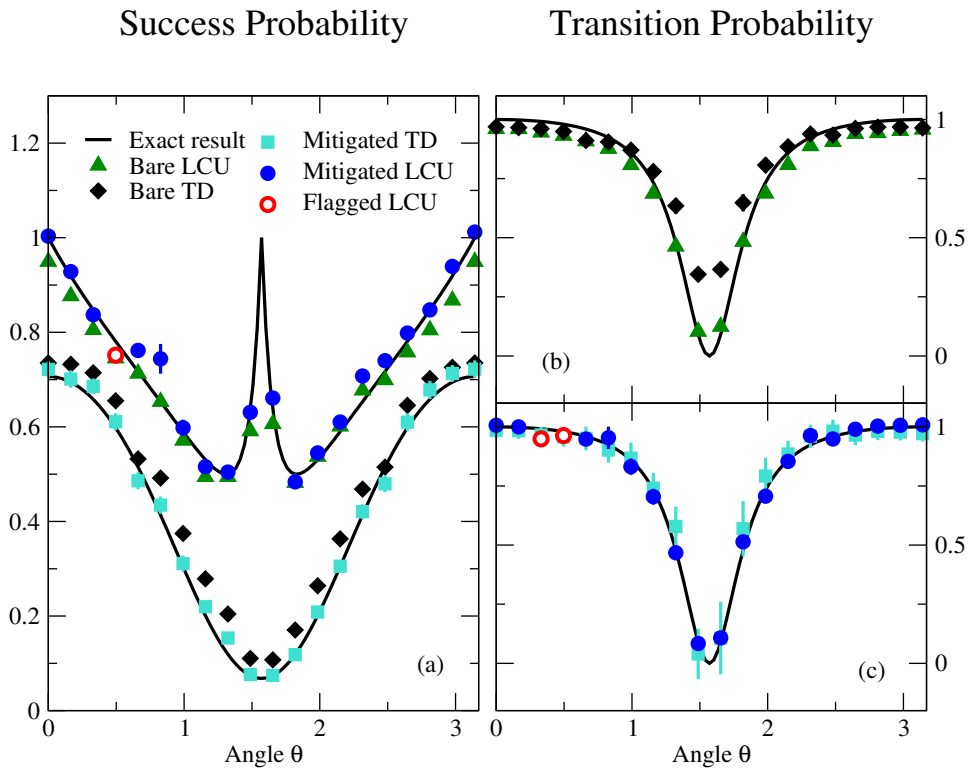


Figure 2.7: Success probability (left panel) and transition probability (right panels) for the excitation operator in Eq. (2.6.7) versus the angle θ, using both the time-dependent (TD) method and the LCU-based method. QPU results with [subplot (c)] and without [subplot (b)] error mitigation and with only read-out correction (red empty circles) are given. The figure is taken from Ref. (Roggero et al., 2020a), which I co-authored.

Table 2.5: Quality metrics χ^2 and nssd of ${}^1S_0 \to {}^3S_1$ transition probability for thermal neutron-proton using (a) the time-dependent (TD) method and (b) the LCU-based method. The bare results (bare), results with read-out error correction (RO mit.), and full error mitigation (full mit.) are shown. Results were obtained on the Vigo QPU (5qubit backed: IBM Q team, 2020).

(a) TD

	χ^2	nssd
bare	11.77	1.198
RO mit.	6.04	1.013
full mit.	0.31	0.436

(b) LCU

	χ^2	nssd
bare	13.62	0.494
RO mit.	1.41	0.173
full mit.	2.19	0.253

circuit implementation details are provided in Subsec. 2.6.1. The calculation was executed on the Vigo QPU (5qubit backed: IBM Q team, 2020), and qubits 1, 4, and 3 are executed for the ancilla qubits A_0, A_1 and A_2, and qubits 0 and 2 are executed for the target qubits T_0, T_1 respectively.

Note that the second quantized form contains non-commuting operators. To implement the time-dependent method, one needs to implement an approximation of the evolution operator instead of exact execution. The time-dependent method becomes relatively inefficient due to the imperfect implementation, as shown in Subsec. 2.2.2. Therefore, only the LCU-based method is used.

The results of success probability, transition probability, and error of transition probability are given in panel (a), panel (b), and panel (c) (note the uniformly spaced index for angle) of Fig. 2.8, respectively. And quality metrics χ^2 and nssd for success probability and transition probability are shown in Tab. 2.6. Black lines represent the exact results for success probability, shown in Eq. (2.3.8), and transition probability in Eq. (2.5.11) (only the ratio estimator considered since its big advantage). QPU results with (green squares) and without (red circles) full mitigation procedures are shown.

From Fig. 2.8, we see that the transition probability has bare results with better quality than the success probability because the ratio estimator applied. This is evidently shown at $\theta = \pi$, even the error of success probability bare result is more than 25%, the error of transition probability bare result is only around 8%. In panel (c), around the angle index as 10 (angle $\theta = \pi/2$), bare results of transition probability show better quality than those mitigated results, and full mitigation procedures fail. In Tab. 2.6, we see that error extrapolation provides less help for transition probability than for success probability (reduced by 2 orders of magnitude in metric χ^2). This behavior is understood as the benefit of utilizing a ratio estimator: the observables are less sensitive to noise.

2.7 Summary

This chapter shows the time-dependent and LCU-based methods, their success probability and fidelity analysis, and the circuit implementation details. Both methods are applied

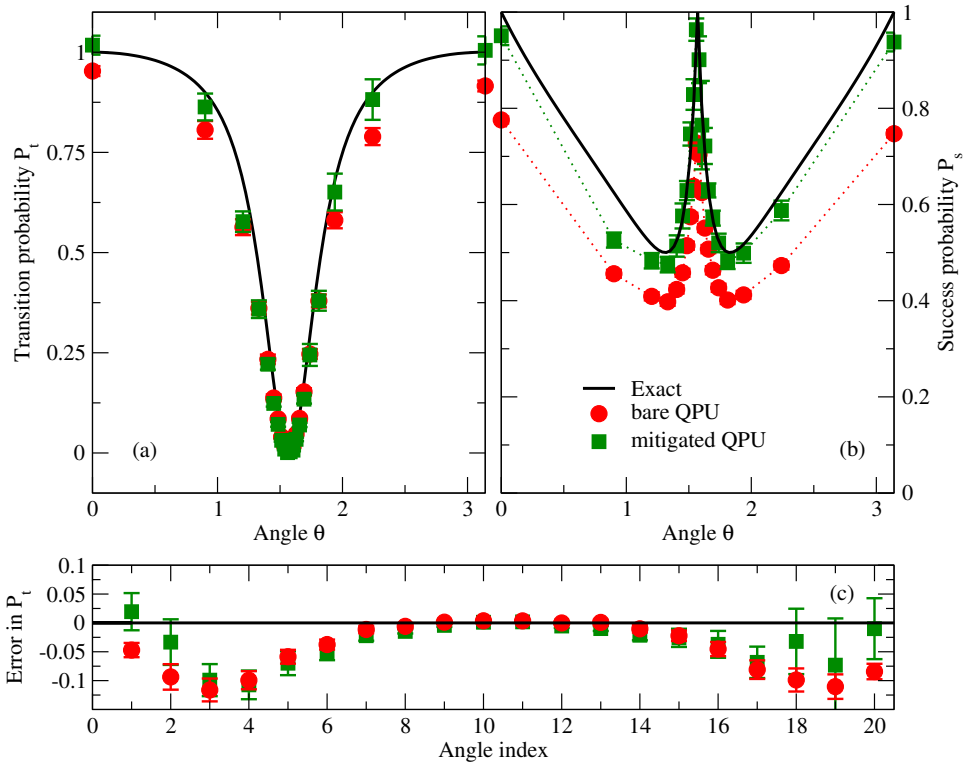


Figure 2.8: Transition probability P_t (a) and success probability P_s (b) and error of transition probability (c) for thermal neutron-proton capture as a function of angle θ. Results are obtained by using the LCU-based method on the Vigo QPU 5qubit backed: IBM Q team (2020). The figure is taken from Ref. (Roggero et al., 2020a), which I co-authored.

Table 2.6: Quality metrics χ^2 and nssd of success probability (a) and transition probability (b) for the excitation operator in Eq. (2.6.4) using the LCU-based method on the Vigo QPU 5qubit backed: IBM Q team (2020). The bare results (bare), results with read-out error correction (RO mit.), and full error mitigation (full mit.) are shown.

(a) Success Probability

	χ^2	nssd
bare	372.01	2.18
RO mit.	250.72	2.04
full mit.	3.81	0.52

(b) Transition Probability

	χ^2	nssd
bare	15.4	1.219
RO mit.	8.0	0.835
full mit.	5.8	0.928

to prepare excited states on virtual machines and real quantum devices, using a simple excitation operator (2.5.1) and a simple model for thermal neutron-proton capture to analyze their accuracy and efficiency. The error mitigation procedures (both read-out correction and error extrapolation) are utilized to reduce the read-out error and infidelity of gate performance.

The results demonstrate that both methods are practicable and efficient for preparing excited states and accurate for producing transition matrix elements. The LCU-based method is better than the time-dependent method as it is more efficient and has a much larger success probability. In contrast, the time-dependent method faces the tradeoff between relatively large success probability and good fidelity. The LCU-based method is also more resilient to depolarizing noise by utilizing ratio estimators, as ratio estimators could exponentially suppress the relative error with the help of ancilla qubits.

Usually, when it is easy to add ancilla qubits, the LCU-based method is a better choice for the state preparation algorithm. In contrast, sometimes the time-dependent method would be better since it only needs one ancilla qubit. More qubits in use will need a higher standard for qubit connectivity and quantum device performance. Note that these considerations would change when considering fault-tolerant quantum devices that allow us to perform the calculation of arbitrary length: the success probability P_s of a quantum algorithm can be increased to 1 using $O(1/\sqrt{P_s})$ additional unitary gates using standard amplitude amplification techniques.

Chapter 3

Entanglement Entropy of Nuclear Systems

This chapter is based on the paper (Gu et al., 2023), which I co-authored. My collaborators and I are inspired by the fact that for a short-ranged correlated fermion system, the entanglement entropy of the subsystems often grows proportional with the area (sometimes times logarithmic corrections) (Eisert et al., 2010) when the system is partitioned into two subsystems. And we are curious about how the entanglement entropy scales in a nuclear many-body system. Because of the short-range interaction, one might expect that the entanglement of nuclear many-body systems should also fulfill area laws. To examine whether this is true, my collaborators and I separate the system into the hole space and the particle space and study the entanglement entropy of subsystems. The analytical results demonstrate that entanglement entropies are proportional to the particle number fluctuation and the depletion of the hole space for sufficiently weak interactions, which indicates a volume law instead of an area law. The numerical calculation of the pairing model, neutron matter, and finite nuclei confirms these arguments.

This chapter provides a brief introduction to the coupled-cluster theory and partition methods in Sec. 3.1, analytical results of entanglement entropies based on the coupled-cluster method in Sec. 3.2, and numerical results of the pairing model and neutron matter in Sec. 3.3.

3.1 Introduction

This section briefly introduces the basic notions that are required in this chapter. Subsec. 3.1.1 discusses the coupled-cluster theory. Subsec. 3.1.2 discusses partitioning the Hilbert space when dealing with a finite system and the approach used in this dissertation. Also, it provides some arguments that the volume law is fulfilled in a nuclear system instead of an area law.

3.1.1 Coupled-cluster Theory

In 1960, Coester and Kümmel (Coester and Kümmel, 1960) first introduced cluster function to describe ground state wave functions of a closed shell nucleus. In the late 1960s, Čížek and Paldus (Čížek, 1966, 2007; Čížek and Paldus, 1971) introduced the coupled-cluster method to quantum chemistry. Since then, the coupled-cluster method has been widely used in solving many-body problems (Kümmel et al., 1978; Jansen et al., 2014; Sun et al., 2018), providing highly accurate and computationally affordable calculations for many-body systems. The standard coupled-cluster formulations (Shavitt and Bartlett, 2009; Bartlett and Musiał, 2007) and an overview of its applications in physics (Bishop, 1991), especially in nuclear physics (Hagen et al., 2014b) can be found.

Let us start with a Hamiltonian, which contains two-body interactions only, given as

$$\hat{H} = \hat{H}_0 + \hat{H}_I = \sum_{i=1}^{N} \hat{h}\left(r_i\right) + \sum_{i<j}^{N} \hat{v}\left(r_{ij}\right) \ . \tag{3.1.1}$$

Here, N is the total number of fermions. Operator $\hat{h}$ and $\hat{v}$ represent the one-body and two-body components of the Hamiltonian. A second quantized form is given as

$$\hat{H} = \sum_{pq} \varepsilon_q^p \hat{a}_p^\dagger \hat{a}_q + \frac{1}{4} \sum_{pqrs} \langle pq||rs\rangle \hat{a}_p^\dagger \hat{a}_q^\dagger \hat{a}_s \hat{a}_r \ , \tag{3.1.2}$$

with a set of single-particle states $\psi_p(x)$ obtained from the Hartree-Fock theory. The operator $\hat{a}_p^\dagger$ creats an particle on the p-th single-particle state $|\psi_p\rangle = \hat{a}_p^\dagger|0\rangle$. Here, $\varepsilon_q^p = \langle\psi_p|\hat{h}|\psi_q\rangle$ represents matrix elements for one-body component, and $\langle pq||rs\rangle = \langle\psi_p\psi_q|\hat{v}|\psi_r\psi_s\rangle -$

$\langle\psi_p\psi_q|\hat{v}|\psi_s\psi_r\rangle$ represents the anti-symmetrized matrix elements for two-body part. The ground state ansatz from the Hartree-Fock theory is given as

$$|\Phi\rangle = \prod_{i=1}^{N} \hat{a}_i^\dagger |0\rangle \ . \tag{3.1.3}$$

I introduce the reference state $|\Phi\rangle$ as the new vacuum and rewrite the Hamiltonian as its normal-ordered form, given as

$$\begin{aligned} \hat{H}_{\mathrm{N}} &= \sum_{pq} f_q^p \left\{\hat{a}_p^\dagger \hat{a}_q\right\} + \frac{1}{4}\sum_{pqrs}\langle pq||rs\rangle \left\{\hat{a}_p^\dagger \hat{a}_q^\dagger \hat{a}_s \hat{a}_r\right\} \\ &= F_{\mathrm{N}} + V_{\mathrm{N}} \ , \end{aligned} \tag{3.1.4}$$

with

$$f_q^p = \varepsilon_q^p + \sum_i \langle pi||qi\rangle \ .$$

Here, $\hat{H} = \hat{H}_{\mathrm{N}} + E_{\mathrm{ref}}$ with $E_{\mathrm{ref}} = \langle\Phi|\hat{H}|\Phi\rangle$ as the reference energy.

A coupled-cluster ansatz (exponential ansatz) for the ground state of a fermionic system is defined as

$$|\Psi\rangle = e^{\hat{T}}|\Phi\rangle \ , \tag{3.1.5}$$

with the cluster operator $\hat{T}$ defined as

$$\hat{T} = \hat{T}_1 + \hat{T}_2 + \cdots + \hat{T}_N \ , \tag{3.1.6}$$

where $\hat{T}_k$ is k-particle–k-hole excitation operator,

$$\hat{T}_k = \frac{1}{(k!)^2} \sum_{\substack{i_1,\ldots,i_k;\\ a_1,\ldots,a_k}} t_{i_1\ldots i_k}^{a_1\ldots a_k} \hat{a}_{a_1}^\dagger \ldots \hat{a}_{a_k}^\dagger \hat{a}_{i_k} \ldots \hat{a}_{i_1} \ . \tag{3.1.7}$$

The coupled-cluster amplitudes $t_{i_1\ldots i_k}^{a_1\ldots a_k}$ are left undetermined.

Based on the vacuum state $|\Phi\rangle$, the single-particle states are categorized into the particle states (denoted with indices $a, b, \cdots$) and the hole states (denoted with indices $i, j, \cdots$), based on whether they are unoccupied or occupied in the reference state. The whole Hilbert space

is partitioned into the hole space (containing hole states) and the particle space (containing particle states). This convention will be applied to the whole chapter. The operators $\hat{a}^\dagger_{a_k}$ and $\hat{a}_{i_k}$ create and annihilate a particle on the particle and hole states, respectively.

Each $\hat{T}_k$ excites k particles in the hole space into the particle space and creates a k-particle-k-hole excitation state, written as

$$\left|\Phi^{a_1\cdots a_2}_{i_1\cdots i_k}\right\rangle \equiv \hat{a}^\dagger_{a_1}\cdots\hat{a}^\dagger_{a_k}\hat{a}_{i_k}\cdots\hat{a}_{i_1}\left|\Phi\right\rangle \ . \tag{3.1.8}$$

It's notable that $e^{\hat{T}}$ is not unitary since generator $\hat{T}$ does not contain de-excitation terms, and the normalization coefficient in state $|\Psi\rangle$ is left out.

The exponential operator can be expanded into a power series

$$e^{\hat{T}} = 1 + \hat{T} + \frac{\hat{T}^2}{2!} + \frac{\hat{T}^3}{3!} + \cdots \ , \tag{3.1.9}$$

which contains all possible correlations of single-particle states. If one truncates the cluster operator, for example, to the order only containing single and double excitation operators, CC still includes higher order excitations since the power series of $\hat{T}$. Let us compare this exponential ansatz with the full configuration interaction (FCI) method, which is the most straightforward method to exactly solve many-body problems that diagonalizes the Hamiltonian on the basis of many-body states. The FCI state is written as

$$\begin{aligned}\left|\Psi_{CI}\right\rangle &= c_0\left|\Phi\right\rangle + \sum_{ai} c^{a_1}_{i_1}\left|\Phi^{a_1}_{i_1}\right\rangle + \sum_{a_1a_2i_1i_2} c^{a_1a_2}_{i_1i_2}\left|\Phi^{a_1a_2}_{i_1i_2}\right\rangle + \cdots \\ &= \left(c_0 + \hat{C}\right)\left|\Phi\right\rangle\end{aligned} \tag{3.1.10}$$

which is an exact ground state written as a superposition of all the possible configurations. The linear excitation operator is defined as

$$\hat{C} = \sum_{a_1i_1} c^{a_1}_{i_1}\hat{a}^\dagger_{a_1}\hat{a}_{i_1} + \sum_{a_1a_2i_1i_2} c^{a_1a_2}_{i_1i_2}\hat{a}^\dagger_{a_1}\hat{a}^\dagger_{a_2}\hat{a}_{i_2}\hat{a}_{i_1} + \ldots \ . \tag{3.1.11}$$

One can find a relationship between the amplitudes of FCI and CC (Cremer, 2013). Without truncation, both methods provide an exact ground state wavefunction.

For practical computation implementation, to obtain the coupled-cluster amplitudes $t_{i_1 \ldots i_k}^{a_1 \ldots a_k}$, we solve the amplitude equations

$$\left\langle \Phi_{i_1 i_2 \ldots}^{a_1 a_2 \cdots} | e^{-\hat{T}} \hat{H}_{\mathrm{N}} e^{\hat{T}} | \Phi \right\rangle = 0 \ . \tag{3.1.12}$$

Then, the energy is obtained via the energy equation

$$E = \left\langle \Phi | e^{-\hat{T}} \hat{H}_{\mathrm{N}} e^{\hat{T}} | \Phi \right\rangle \ . \tag{3.1.13}$$

Here, $\bar{H} = e^{-\hat{T}} \hat{H}_{\mathrm{N}} e^{\hat{T}}$ is the similarity transformed normal order Hamiltonian, which is named as the CC effective Hamiltonian. We can expand $\bar{H}$ based on Baker-Campbell-Hausdorff (BCH) expansion,

$$e^{-\hat{T}} \hat{H} e^{\hat{T}} = \hat{H} + \left[\hat{H}, \hat{T}\right] + \frac{1}{2!}\left[\left[\hat{H}, \hat{T}\right], \hat{T}\right] + \frac{1}{3!}\left[\left[\left[\hat{H}, \hat{T}\right], \hat{T}\right], \hat{T}\right] + \ldots \ , \tag{3.1.14}$$

which is called as Hausdorff expansion. The advantage of this form is a simplification would appear as an infinite series of nested commutators truncates naturally to a four-fold commutator (see Chapter 10 in Ref. (Shavitt and Bartlett, 2009)). Also, this form provides a more productive view of understanding CC theory as finding eigenstates of the effective Hamiltonian (similarity transformed, which is not Hermitian) that exhibits no excitation corrections on the left.

As mentioned in Ref. (Crawford and Schaefer, 2007), "the only nonzero terms in the Hausdorff expansion are those in which the Hamiltonian, $\hat{H}_{\mathrm{N}}$, has at least one contraction with every cluster operator, $\hat{T}_N$, on its right", Eq. (3.1.14) is further simplified as

$$\begin{aligned} \bar{H} &= \hat{H}_N + \left(\hat{H}_N \hat{T}\right)_c + \frac{1}{2}\left(\hat{H}_N \hat{T}^2\right)_c + \cdots \\ &= \left(\hat{H}_N e^{\hat{T}}\right)_c \ , \end{aligned} \tag{3.1.15}$$

generalized by Wick's theorem.

Coupled-cluster Double Approximation

In practical computation, the number of unknown amplitudes with full cluster operators grows exponentially, just like the FCI method. The number of all possible Slater determinants, as the dimension of Hilbert space, grows exponentially with the problem size. Think about having A neutrons distributing in N different single-particle states; one will have the number of possible configurations as

$$\begin{pmatrix} N \\ A \end{pmatrix} = \frac{N!}{(N-A)!A!} , \tag{3.1.16}$$

due to the fermionic property, only one particle occupies the state at a time.

To manage this, people often truncate the cluster operator to a specific order, a strategy that significantly reduces computational complexity. The simplest truncation is the coupled-cluster doubles (CCD) approximation, which only executes two-particle–two-hole excitations, i.e., $\hat{T} = \hat{T}_2$, then the ground state ansatz is written as

$$|\Psi_{\text{CCD}}\rangle = e^{\hat{T}_2}|\Phi\rangle \ . \tag{3.1.17}$$

The coupled-cluster singles approximation, i.e., $\hat{T} = \hat{T}_1$, is not considered as a valid approximation since $e^{\hat{T}_1}$ is just transforming the Slater determinant $|\Phi\rangle$ into another Slater determinants, based on Thouless Theorem; see Eq. (2) in Ref. (Thouless, 1960).

A further improvement of CCD is adding one-particle-one-hole excitations $\hat{T}_1$ and utilizing the coupled-cluster singles and doubles (CCSD) approximation, i.e., $\hat{T} = \hat{T}_1 + \hat{T}_2$, with the state ansatz as

$$|\Psi_{\text{CCSD}}\rangle = e^{\hat{T}_1+\hat{T}_2}|\Phi\rangle \ . \tag{3.1.18}$$

Here, the excitation operator $\hat{T}_1$ will generate higher order excitations, like $\hat{T}_1\hat{T}_2$ and $\hat{T}_1\hat{T}_1$.

Next, I provide a more detailed CCD calculation. The energy is given by

$$\begin{aligned} E_{\mathrm{CCD}} &= \left\langle \Phi \left| \left(\hat{H}_N e^{\hat{T}_2} \right)_c \right| \Phi \right\rangle \\ &= \left\langle \Phi \left| \hat{H}_N \left(1 + \hat{T}_2 \right) \right| \Phi \right\rangle \\ &= E_{\mathrm{ref}} + \frac{1}{4} \sum_{abij} \langle ij||ab\rangle t_{ij}^{ab} \\ &= E_{\mathrm{ref}} + \Delta E_{\mathrm{CCD}} \ , \end{aligned} \tag{3.1.19}$$

where ΔE_{CCD} is the CCD correlation energy. The amplitudes $t_{i_1 i_2}^{a_1 a_2}$ obtained by solving equations

$$\begin{aligned} 0 &= \left\langle \Phi_{i_1 i_2}^{a_1 a_2} \left| \left(\hat{H}_N e^{\hat{T}_2} \right)_c \right| \Phi \right\rangle \\ &= \left\langle \Phi_{i_1 i_2}^{a_1 a_2} \left| \hat{H}_N \left(1 + \hat{T}_2 + \frac{1}{2} \hat{T}_2^2 \right) \right| \Phi \right\rangle \ . \end{aligned} \tag{3.1.20}$$

The matrix element $\bar{H}_{ij}^{ab}$ is written as

$$\begin{aligned} \bar{H}_{ij}^{ab} &= \langle ab||ij\rangle + P(ab) \sum_c f_c^b t_{ij}^{ac} - P(ij) \sum_k f_j^k t_{ik}^{ab} \\ &+ \frac{1}{2} \sum_{cd} \langle ab||cd\rangle t_{ij}^{cd} + \frac{1}{2} \sum_{kl} \langle kl||ij\rangle t_{kl}^{ab} + P(ab)P(ij) \sum_{kc} \langle kb||cj\rangle t_{ik}^{ac} \\ &+ \frac{1}{2} P(ij)P(ab) \sum_{klcd} \langle kl||cd\rangle t_{ik}^{ac} t_{lj}^{db} + \frac{1}{2} P(ij) \sum_{klcd} \langle kl||cd\rangle t_{ik}^{cd} t_{lj}^{ab} \\ &+ \frac{1}{2} P(ab) \sum_{klcd} \langle kl||cd\rangle t_{kl}^{ac} t_{ij}^{db} + \frac{1}{4} \sum_{klcd} \langle kl||cd\rangle t_{ij}^{cd} t_{kl}^{ab}, \end{aligned} \tag{3.1.21}$$

and $\bar{H}_{ij}^{ab} = 0$ gives us amplitudes. Here $P(ab) = 1 - \hat{P}_{ab}$ is the permutation operator. For a more detailed derivation of Eq. (3.1.21) and derivation of CCSD amplitudes and energy equations, I refer readers to Ref. (Shavitt and Bartlett, 2009).

The standard method to calculate this CCD amplitude equation is using iteration,

$$t_{ij}^{ab} = t_{ij}^{ab} + \frac{\bar{H}_{ij}^{ab}}{\varepsilon_{ij}^{ab}} \ . \tag{3.1.22}$$

Here, $\varepsilon_{ij}^{ab} = \varepsilon_i + \varepsilon_j - \varepsilon_a - \varepsilon_b$ and $\varepsilon_p = \langle\psi_p|\hat{h}|\psi_p\rangle$. Then, one can obtain $t^{(n+1)} = f(t^{(n)})$ iteratively until the correlation energy converged. Here t is a shortening for t_{ij}^{ab}. The common initial guess of amplitudes is written as

$$t^{(0)} = \frac{\langle ab\|ij\rangle}{\varepsilon_{ij}^{ab}} , \tag{3.1.23}$$

which only contains the first term in Eq. (3.1.21), and this is related to the second-order many-body perturbation theory (MBPT2). For an introduction to MBPT and its connection to CC theory, I refer the readers to Ref. (Shavitt and Bartlett, 2009). The zeroth correlation energy is given as

$$\Delta E_{\mathrm{CCD}}^{(0)} = \frac{1}{4}\sum_{abij}\frac{\langle ij||ab\rangle\langle ab||ij\rangle}{\varepsilon_{ij}^{ab}} . \tag{3.1.24}$$

which is equal to second-order energy correction from MBPT2.

3.1.2 Subspace Structure and Entanglement Entropy

This subsection discusses different approaches to partitioning the Hilbert space when dealing with a finite system and the approach used in this dissertation.

Given a Hilbert space $\mathcal{H}$ which is decomposed as $\mathcal{H} = \mathcal{H}_A \otimes \mathcal{H}_B$ in terms of the Hilbert spaces of two subsystems A and B. Assume $|\Phi_{AB}\rangle \in \mathcal{H}$ is a pure state. The entanglement entropy is usually given with Von Neumann entropy as $S(\rho_A) = S(\rho_B)$.

In discussing the many-body quantum systems, mode entanglement is considered to quantify the entanglement between one single-particle state and the complement states. The one-mode entropy is given as Von Neumann entropy $S(\rho_k)$ where ρ_k is one-mode reduced density matrix, defined as

$$\rho_k \equiv \begin{pmatrix} \left\langle a_k^\dagger a_k \right\rangle & 0 \\ 0 & 1 - \left\langle a_k^\dagger a_k \right\rangle \end{pmatrix} ,$$

with $\left\langle a_k^\dagger a_k \right\rangle = \left\langle \Psi \left| a_k^\dagger a_k \right| \Psi \right\rangle$ denoting the occupation probability of a particle in single-particle state k. The summation over mode entropies $\sum_k S(\rho_k)$ gives the total correlation of the system corresponding to the single-particle basis (the value depends on the choice of

basis). The minimum of total entanglement is obtained in the natural basis (Gigena and Rossignoli, 2015), in which each single-particle states are disentangled.

In nuclear physics, mode entanglement is used. For example, the work (Legeza et al., 2015) calculated the one-orbital (mode) entropy and two-orbital mutual information (indicates how single-particle states are correlated) for ^{64}Ge by applying DMRG. They show that the entropy can indicate the importance of an orbital, in which sense, how much it contributes to the correlation energy. The work (Robin et al., 2021) calculated entanglement between single-particle states of ^{4}He and ^{6}He. They calculated the one-orbital and two-orbital entanglement entropy (obtained from Von Neumann entropy of two-orbital reduced density matrix, see Appendix B of Ref. (Robin et al., 2021)), two-orbital mutual information and negativity based on various bases and discussed their entanglement structures.

In this dissertation, instead of calculating mode entanglement between one or two single-particle states and the complement states, the entanglement is quantified by the entropy between hole space and particle space with the full fermionic many-body wave function. The hole space contains every single-particle state of the reference state, which is described in Eq. (3.1.3), obtained from the Hartree-Fock method. This is a good indicator of the correlation between reference states and other particle states, and it can showcase how those particle states can help improve the precision of the model.

Here, I provide details about how to get the reduced density matrix of hole space. Every configurations (3.1.8) are expressed as a product of hole space states $|i_1^{-1}i_2^{-1}\cdots\rangle$ and particle space states $|a_1a_2\cdots\rangle$,

$$\left|\Phi^{a_1a_2\cdots}_{i_1i_2\cdots}\right\rangle = |a_1a_2\cdots\rangle \otimes |i_1^{-1}i_2^{-1}\cdots\rangle \ . \tag{3.1.25}$$

An arbitrary normalized state $|\Psi\rangle$ can be written as the superposition of all configurations,

$$\begin{aligned} |\Psi\rangle &= C_0\,|\Phi\rangle + \sum_{a_1i_1} C^{a_1}_{i_1}\left|\Phi^{a_1}_{i_1}\right\rangle + \sum_{a_1a_2i_1i_2} C^{a_1a_2}_{i_1i_2}\left|\Phi^{a_1a_2}_{i_1i_2}\right\rangle + \cdots \\ &= \sum_{n=0}^{N}\sum_{\substack{i_1\ldots i_n\\ a_1\ldots a_n}} C^{a_1\cdots a_n}_{i_1\cdots i_n}\left|\Phi^{a_1\cdots a_n}_{i_1\cdots i_n}\right\rangle \ , \end{aligned} \tag{3.1.26}$$

with those coefficients undefined and can be obtained by the coupled-cluster method. n is the number of particles that are excited from hole states to particle states, and n runs over 0 to N, which is the total number of particles in the nuclear system. The reference state $|\Phi\rangle$ is obtained when $n = 0$.

The density matrix ρ associated with each state is denoted as

$$\begin{aligned}\hat{\rho} &= |\Psi\rangle\langle\Psi| \\ &= \sum_{n=0}^{N}\sum_{m=0}^{N}\sum_{\substack{i_1\ldots i_n\\ a_1\ldots a_n}}\sum_{\substack{j_1\ldots j_m\\ b_1\ldots b_m}} C_{i_1\cdots i_n}^{a_1\cdots a_n} C_{j_1\cdots j_m}^{b_1\cdots b_m} \left|\Phi_{i_1\cdots i_n}^{a_1\cdots a_n}\right\rangle \left\langle\Phi_{j_1\cdots j_m}^{b_1\cdots b_m}\right| \ .\end{aligned} \tag{3.1.27}$$

The hole space reduced density matrix $\hat{\rho}_{\mathrm{H}}$ is obtained by tracing over the particle space states and is defined as

$$\begin{aligned}\hat{\rho}_{\mathrm{H}} =& \mathrm{Tr}_{\mathrm{P}}\hat{\rho} \\ =& \sum_{n=0}^{N}\sum_{a_1<a_2<\cdots<a_n}\left(\hat{I}_{\mathrm{H}}\otimes\langle a_n\ldots a_1|\right)\hat{\rho}\left(\hat{I}_{\mathrm{H}}\otimes|a_1\ldots a_n\rangle\right) \\ =& \sum_{n=0}^{N}\sum_{\substack{a_1<a_2<\cdots<a_n\\ i_1<i_2<\cdots<i_n\\ j_1<j_2<\cdots<j_n}}\left\langle\Phi_{j_1\ldots j_n}^{a_1\ldots a_n}\right|\hat{\rho}\left|\Phi_{i_1\ldots i_n}^{a_1\ldots a_n}\right\rangle \\ &\times\left|j_1^{-1}\ldots j_n^{-1}\right\rangle\left\langle i_n^{-1}\ldots i_1^{-1}\right| \ ,\end{aligned} \tag{3.1.28}$$

where $\hat{I}_{\mathrm{H}}$ is the identity in hole space. We can check that Eq. (3.1.28) represents a density matrix.

Furthermore, the Rényi entropy Eq. (1.3.3) and von Neumann entropy Eq. (1.3.1) of $\hat{\rho}_{\mathrm{H}}$ are calculated to quantify the entanglement of the hole space.

I have mentioned in Chapt. 1.3 that for the short-range interaction system, one would expect entanglement entropy S or particle number fluctuation $(\Delta N)^2$ of subsystem would obey area laws L^{d-1} (times some logarithmic corrections $L^{d-1}\log(L)$) (Eisert et al., 2010). I have pointed out that area laws might no longer be held in nuclear physics.

For example, mode entanglement is used and modified in work (Pazy, 2023). It separated the long and short-ranged physics by Similarity Renormalization Group (SRG)

transformation, studied entanglement entropy in terms of the high momentum states, and showed the total SRC entanglement entropy as

$$S_A^{SRC} = -\frac{A}{2}\left[c\ln\left(\frac{c}{1-c}\right) + \ln(1-c)\right] , \tag{3.1.29}$$

which showcases that the entanglement entropy is proportional to nucleon number A, or, say, the nucleus volume. Here, c is related to the eigenvalue of the one-mode reduced density matrix.

Let's consider the entanglement between hole space and particle space. Fig. 3.1 gives a sketch of single-particle states in position space. The blue area represents the volume where hole states spread out. The grey area, together with the blue area, represents the single-particle space. The red points represent localized hole states with nearest neighbor distance as around π/k_F^{-1}. k_F is the Fermi momentum. The black points represent localized particle states with nearest neighbor distance as π/Λ^{-1}, where Λ^{-1} is the momentum cutoff. We can see that the particle states are more dense than the hole states and that every hole state is correlated with particle states. This indicates that the entanglement entropy fulfills a volume law instead of an area law.

In momentum space, unlike in Fig. 3.1, where particle and hole states spread out in the blue area, particle states only spread out in the grey area, and the blue area can represent the Fermi sphere instead. The scaling problem of the entanglement entropy in momentum space is more apparent. It is expected to fulfill a volume law since the interactions are long-ranged. Sec. II of Ref. (Gu et al., 2023) also provides the argument based on lattice calculation, suggesting a volume law.

3.2 Analytical Results Based on the Coupled-cluster Theory

This section provides the analytical results of the Rényi entropy in Subsec. 3.2.1, and the particle number fluctuation and depletion of the hole space, and their relation in Subsec. 3.2.2. The analytical results are obtained based on CCD approximation. In this

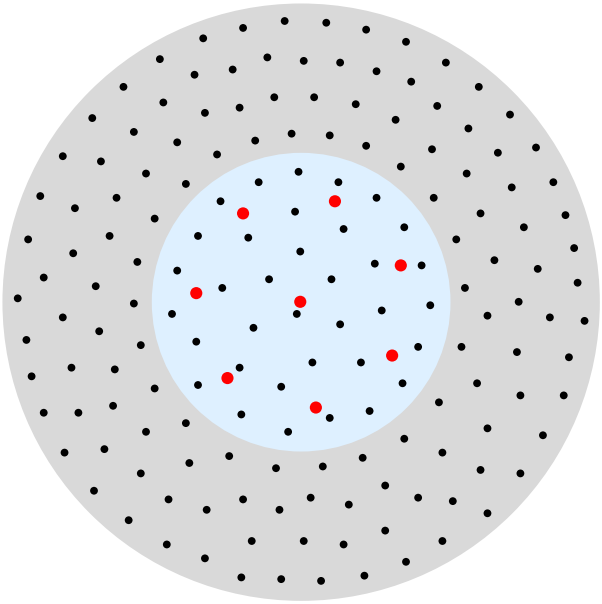


Figure 3.1: Schematic diagram of nuclear volume (light blue area) and its complement (gray area) for a finite spherical basis in position space. Red and black points represent localized hole and particle states, respectively. The figure is taken from Ref. (Gu et al., 2023), which I co-authored.

dissertation, I will provide the numerical results for the pairing model and the neutron matter and compare them with the analytical results in this section. The CCD ansatz (3.1.17) is a valid approximation for the pairing model and the neutron matter since the Hamiltonian of the pairing model only excites pairs of particles, and the momentum space is used in the neutron matter calculation that one-particle-one-hole excitations are not allowed since the conservation of momentum.

3.2.1 Approximate Entanglement Entropies

With the CCD ansatz (3.1.17), the density matrix is written as

$$\hat{\rho} = \frac{|\Psi_{\rm CCD}\rangle\langle\Psi_{\rm CCD}|}{\langle\Psi_{\rm CCD}|\Psi_{\rm CCD}\rangle} \ . \tag{3.2.1}$$

The hole-space reduced density matrix $\hat{\rho}_{\rm H}$ is obtained by tracing the density matrix $\hat{\rho}$ over the particle states $\hat{\rho}_{\rm H} = {\rm Tr}_{\rm P}\hat{\rho}$, the general form is given in Eq. (3.1.28). For clarity, the matrix elements of $\hat{\rho}_{\rm H}$ are expressed as following:

$$\begin{aligned}
\langle|\rho_{\rm H}|\rangle &= \langle\Phi|\hat{\rho}|\Phi\rangle \ , \\
\left\langle i_1^{-1} i_2^{-1}|\rho_{\rm H}|j_1^{-1} j_2^{-1}\right\rangle &= \sum_{a_1<a_2} \left\langle \Phi^{a_1 a_2}_{i_1 i_2}|\hat{\rho}|\Phi^{a_1 a_2}_{j_1 j_2}\right\rangle \ , \\
&\vdots \\
\left\langle i_1^{-1}\cdots i_N^{-1}|\rho_{\rm H}|j_1^{-1}\cdots j_N^{-1}\right\rangle &= \\
&\sum_{a_1<\cdots<a_N} \left\langle \Phi^{a_1\cdots a_N}_{i_1\cdots i_N}|\hat{\rho}|\Phi^{a_1\cdots a_N}_{j_1\cdots j_N}\right\rangle \ .
\end{aligned} \tag{3.2.2}$$

The first line in Eq. (3.2.2) is obtained by tracing over the vacuum state $|\Phi\rangle$, and here state $|\rangle$ denotes zero-hole states. The second line is obtained by tracing over two-particle states and so on. As the CCD approximation is in use, only those matrix elements related to even-numbered particle states exist; otherwise, the matrix element will vanish.

All matrix elements in Eq. (3.2.2) are needed to calculate the entanglement entropies, and the exact evaluation is challenging. We assume that $\hat{T}_2$ is small, and make the approximation

as following:

$$\begin{aligned} |\widetilde{\Psi_{\mathrm{CCD}}}\rangle &\approx \left(1+\hat{T}_2\right)|\Phi\rangle \\ &= |\Phi\rangle + \frac{1}{4}\sum_{abij} t_{ij}^{ab}|\Phi_{ij}^{ab}\rangle \ . \end{aligned} \tag{3.2.3}$$

Then, the density matrix is written as

$$\hat{\rho} = C^{-1}|\widetilde{\Psi_{\mathrm{CCD}}}\rangle\langle\widetilde{\Psi_{\mathrm{CCD}}}| \ , \tag{3.2.4}$$

with the normalization coefficient

$$\begin{aligned} C &\equiv \langle\widetilde{\Psi_{\mathrm{CCD}}}|\widetilde{\Psi_{\mathrm{CCD}}}\rangle \\ &= 1+t^2 \ , \end{aligned} \tag{3.2.5}$$

with

$$t^2 \equiv \frac{1}{4}\sum_{i_1 i_2 a_1 a_2} t_{i_1 i_2}^{a_1 a_2} t_{i_1 i_2}^{a_1 a_2} \ . \tag{3.2.6}$$

The approximation (3.2.3) is valid for $t^2 \ll 1$, and this quantifies in what sense $\hat{T}_2$ is small. The hole space reduced density matrix is written as

$$\begin{aligned} \hat{\rho_{\mathrm{H}}} &= \frac{1}{C}\left(|\rangle\langle| + \sum_{a<b} t_{ij}^{ab} t_{kl}^{ab} \left|k^{-1}l^{-1}\right\rangle \left\langle j^{-1}i^{-1}\right|\right) \\ &\doteq \frac{1}{1+t^2}\begin{bmatrix} 1 & 0 \\ 0 & \hat{\rho}_2 \end{bmatrix} \ . \end{aligned} \tag{3.2.7}$$

The symbol $\doteq$ denotes the operator is represented by a matrix. The reduced density matrix is written as a block matrix in the second line. Here, $\hat{\rho}_2$ represents a two-hole-two-hole matrix with matrix elements

$$\rho_{ij}^{kl} = \sum_{a<b} t_{ij}^{ab} t_{kl}^{ab} \ . \tag{3.2.8}$$

The indexes satisfy $i < j$ and $k < l$. The dimension of matrix $\hat{\rho}_2$ is $D \equiv N(N-1)/2$ for a system with N fermions. As a check, we see that

$$\mathrm{Tr}\,\hat{\rho}_2 = \sum_{i<j} \rho_{ij}^{ij} = t^2 \ , \tag{3.2.9}$$

and we indeed have $\mathrm{Tr}\,\hat{\rho}_{\mathrm{H}} = 1$. For what follows, I rewrite

$$\hat{\rho}_2 = t^2 \hat{\sigma} \ , \tag{3.2.10}$$

where $\hat{\sigma}$ is a density matrix, with $\mathrm{Tr}\,\hat{\sigma} = 1$.

To quantify the entanglement of $\hat{\rho}_{\mathrm{H}}$, the Rényi entropies S_α (1.3.3) and the von Neumann entropy S_1 (1.3.4) are used. The necessary part $\mathrm{Tr}\,\hat{\rho}_H^\alpha$ is obtained as

$$\begin{aligned} \mathrm{Tr}\,\hat{\rho}_{\mathrm{H}}^\alpha &= \mathrm{Tr}\left(\frac{1}{(1+t^2)^\alpha} \begin{bmatrix} 1 & 0 \\ 0 & \hat{\rho}_2^\alpha \end{bmatrix} \right) \\ &= (1+t^2)^{-\alpha} \left(1 + t^{2\alpha}\,\mathrm{Tr}\,\hat{\sigma}^\alpha\right) \ . \end{aligned} \tag{3.2.11}$$

From here on, the parameter α is restricted to $\alpha \geq 1$. Then,

$$\begin{aligned} S_\alpha &= \frac{1}{1-\alpha} \ln\left[(1+t^2)^{-\alpha}\left(1 + t^{2\alpha}\,\mathrm{Tr}\,\hat{\sigma}^\alpha\right)\right] \\ &= \frac{t^{2\alpha}\,\mathrm{Tr}\,\hat{\sigma}^\alpha - \alpha t^2}{1-\alpha} + \mathcal{O}(t^4) + \mathcal{O}(t^{4\alpha}) \ . \end{aligned} \tag{3.2.12}$$

The condition $t^2 \ll 1$ is used in the second line, that $\ln(1+x) = x + \mathcal{O}(x^2)$ with small x.

For $\alpha \to 1$, the L'Hopital rule is used and Eq. (3.2.12) becomes

$$S_1 = t^2 \left[1 - \mathrm{Tr}\left(\hat{\sigma}\log\hat{\sigma}\right) - \log t^2\right] + \mathcal{O}(t^4) \ . \tag{3.2.13}$$

The matrix $\hat{\sigma}$ has dimension D. Thus, $0 \leq -\,\mathrm{Tr}(\hat{\sigma}\log\hat{\sigma}) \leq \log D$. Here, the minimum arises when all but one eigenvalue of $\hat{\sigma}$ vanishes, while the maximum arises when all eigenvalues are equal.

For $\alpha > 1$, Eq. (3.2.12) is further simplified as

$$S_\alpha = \frac{\alpha}{\alpha - 1} t^2 + \mathcal{O}(t^{2\alpha}) + \mathcal{O}(t^4) \quad \text{for } \alpha > 1, \tag{3.2.14}$$

for $t^2 \ll 1$. Here, as $\hat{\sigma}$ is not a pure state density matrix, we have $\mathrm{Tr}(\hat{\sigma}^\alpha) < 1$. More precisely, the bounds is given as $D^{1-\alpha} \leq \mathrm{Tr}(\hat{\sigma}^\alpha) \leq 1$ (Subramanian and Hsieh, 2021) for $\alpha > 1$. We see the omission of $\mathcal{O}(t^{2\alpha})$ is valid for sufficiently large index α, then Rényi entropies become independent of the matrix (3.2.10).

Furthermore, I apply the limit $t^2 \to 0$ to Eq. (3.2.12) and Eq. (3.2.13), with which the interactions are arbitrarily small, and get the asymptotic behavior as

$$S_\alpha \to \begin{cases} -t^2 \log t^2 & \text{for } \alpha = 1 \text{ and } t^2 \to 0 \ , \\ \\ \dfrac{\alpha}{\alpha - 1} t^2 & \text{for } \alpha > 1 \text{ and } t^2 \to 0 \ . \end{cases} \tag{3.2.15}$$

Note that the asymptotic results are independent of the matrix $\hat{\sigma}$ in Eq. (3.2.10). The derivation clarifies that the limits $\alpha \to 1$ and $t^2 \to 0$ do not commute. If we change the order, matrix dependence will still exist.

3.2.2 Particle Numbers Fluctuation

The number operator for the particles in the hole space is

$$\begin{aligned} \hat{N}_\mathrm{H} &= \sum_{i=1}^{N} \hat{a}_i^\dagger \hat{a}_i \\ &\doteq \begin{bmatrix} N & 0 \\ 0 & N-2 \end{bmatrix} . \end{aligned} \tag{3.2.16}$$

This matrix representation has the same structure and dimensions as the reduced density matrix $\hat{\rho}_\mathrm{H}$ (3.2.7), with the basis as two-hole states in the second block and with the basis

state $|\rangle$ in the first block. The expectation of the number operator is calculated as

$$\begin{aligned}\langle N_{\rm H}\rangle &\equiv {\rm Tr}(\hat{\rho}_{\rm H}\hat{N}_{\rm H}) \\ &= \frac{N+(N-2)t^2}{1+t^2} \\ &= N-2t^2+\mathcal{O}(t^4)\ ,\end{aligned} \tag{3.2.17}$$

and the expectation of the number operator square is

$$\begin{aligned}\langle N_{\rm H}^2\rangle &\equiv {\rm Tr}(\hat{\rho}_{\rm H}\hat{N}_{\rm H}^2) \\ &= \frac{N^2+(N-2)^2t^2}{1+t^2} \\ &= N^2-4t^2(N-1)+\mathcal{O}(t^4)\ .\end{aligned} \tag{3.2.18}$$

Here in the third line of (3.2.17) and Eq. (3.2.18), the expansion $1/(1+x)=1-x+\mathcal{O}(x^2)$ for small x is used.

Then, the particle-number fluctuation is

$$\begin{aligned}(\Delta N_{\rm H})^2 &\equiv \langle N_{\rm H}^2\rangle-\langle N_{\rm H}\rangle^2 \\ &= 4t^2+\mathcal{O}(t^4)\ \ ,\end{aligned} \tag{3.2.19}$$

which gives a relation $t^2 \approx (\Delta N_{\rm H})^2/4$. Combine this relation with Rényi entropies (in Eqs. (3.2.12) and Eqs. (3.2.13) and their asymptotic expressions (3.2.15)), we can see that Rényi entropies are functions of the particle-number fluctuation. These expressions extend the pioneering results (Klich, 2006) to finite systems of interacting fermions.

Also, let's consider the depletion number of the reference state

$$\begin{aligned}\delta N_{\rm H} &\equiv N-\langle N_{\rm H}\rangle \\ &= 2t^2+\mathcal{O}(t^4)\ ,\end{aligned} \tag{3.2.20}$$

which is simple to calculate in many-body systems. We can find the relation between the entanglement entropy and the depletion number as

$$\frac{1}{4}(\Delta N_{\mathrm{H}})^2 \approx \frac{1}{2}(\delta N_{\mathrm{H}}) \approx t^2 \ . \tag{3.2.21}$$

The corrections to this relation are higher powers of δN_{H} or $(\Delta N_{\mathrm{H}})^2$ or t^2.

The proportionality between the entropy and the particle-number fluctuation breaks down when one includes higher powers of T_2 in the ground state. Our analytical results (3.2.12), (3.2.13), and (3.2.15), combined with (3.2.21) generalize the result (Klich, 2006) to weakly interacting finite Fermi systems.

3.3 Entanglement in Nuclear Systems

This section provides the numerical results of the pairing model in Subsec. 3.3.1 and the neutron matter in Subsec. 3.3.2. Both calculations are based on the CCD method, introduced in Subsec. 3.1.1.

3.3.1 Pairing Model

The Hamiltonian of a pairing model is

$$\begin{aligned} \hat{H} &= \delta \sum_{p\sigma} (p-1) \hat{a}^\dagger_{p\sigma} \hat{a}_{p\sigma} \\ &\quad - \frac{1}{2} g \sum_{pq} \hat{a}^\dagger_{p+} \hat{a}^\dagger_{p-} \hat{a}_{q-} \hat{a}_{q+} \ , \end{aligned} \tag{3.3.1}$$

where the doubly degenerate orbitals are labeled with index $p = 1, 2, \ldots, \Omega/2$ and spin states $\sigma = \pm$. Here $\Omega/2$ is the number of orbitals. I restrict the model to a half-filled pairing model in the numerical calculation, which means the total number of particles is $\Omega/2$ as well (i.e., $\Omega/4$ pairs). Each orbital is equally spaced, with the spacing parameter δ. In what follows, $\delta = 1$ is set without losing generality, and all energies (and the coupling strength parameter g) are measured in units of δ.

The Hamiltonian contains two parts: the kinetic energy of each particle and two-body interactions that excite a pair of particles in the same orbital at a time. The pairing model is exactly solvable (Dukelsky et al., 2004). Therefore, it is a wonderful test case for studying entanglement. The exact results of eigenvalues and eigenstates can be obtained from directly diagonalizing the Hamiltonian, for a relatively small basis. For a sufficiently small coupling strength g, the CCD approximation can accurately solve the pairing model; see Fig. (1.5) and Tab. (1.13) in Ref. (Lietz et al., 2017).

Following the standard procedures introduced in Subsec. 3.1.1, the amplitude equations are given as Eq. (3.1.21). Following the code given in the Python notebook (T. Papenbrock, 2018), the amplitudes can be obtained iteratively.

After obtaining amplitudes from the CCD method with the ground state ansatz (3.1.17), we then compute the reduced density matrix (3.2.7) (which is actually based on the approximated CCD wavefunction (3.2.3)), the corresponding von Neumann entropy S_1 (1.3.1), the Rényi entropy S_2 (1.3.3) and the particle-number fluctuation $(\Delta N_{\mathrm{H}})^2$ (3.2.19). The results are shown in the Fig. 3.2.

Fig. 3.2 shows the relation bewteen entanglement entropies S_1 (full markers) and S_2 (hollow markers) with respect to $(\Delta N_{\mathrm{H}})^2$. And their analytical relation (given in Eq. (3.2.14) and Eq. (3.2.15), combined with Eq. (3.2.21)) are shown as the dash-dotted and dashed lines. Rényi entropy with different α shows a similar results pattern while monotonically decreasing with respect to α, so only S_1 and S_2 will be shown in the results. Results with different coupling strengths ($g = 10^{-3}, 0.01, 0.1, 0.2, 0.5$) are denoted by differently colored and shaped markers. Within a coupling strength g, the half-filled pairing models with one to twelve pairs of particles are calculated, and the results are denoted by identical markers. The method to identify the number of pairs for a specific marker, one can derive from the fact that S_α and $(\Delta N_{\mathrm{H}})^2$ increase with an increasing number of pairs.

From the Fig. 3.2, one can see that the analytical results agree with numerical results for sufficiently weak interactions (small t^2), i.e., sufficiently small values of $(\Delta N_{\mathrm{H}})^2$. The agreement is further examined in Fig. 3.3, which provides the absolute differences between analytical results and numerical results (normalized by the numerical results) as a function of $(\Delta N_{\mathrm{H}})^2$. We can see, for S_1, the analytical result is probably only reached asymptotically

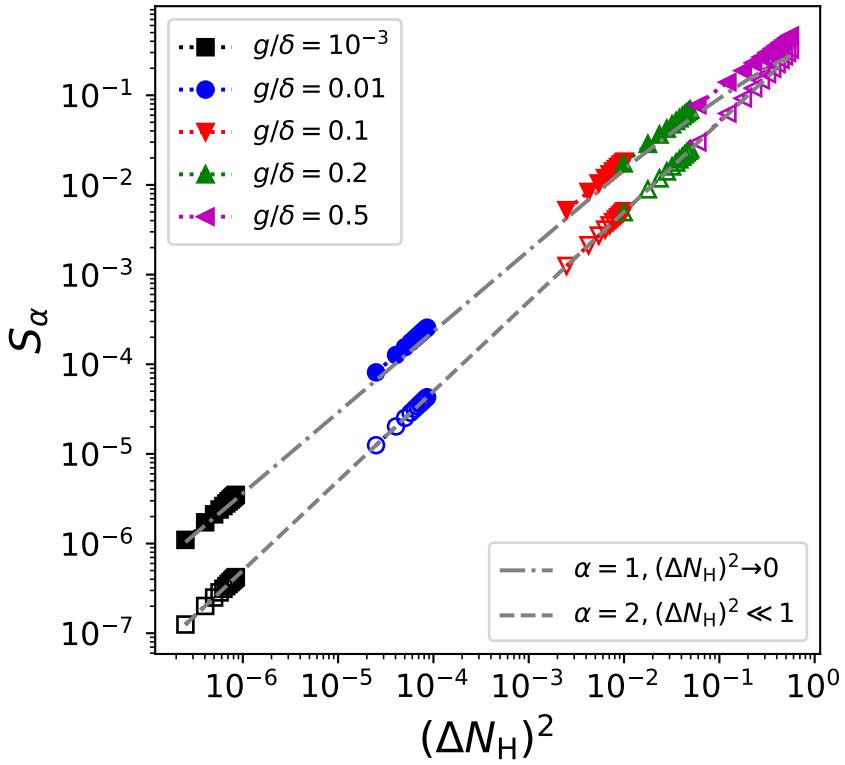


Figure 3.2: Von Neumann entropies S_1 (full markers) and Rényi entropies S_2 (hollow markers) of the reduced hole-space density matrix ρ_{H} versus the particle-number fluctuation $(\Delta N_{\mathrm{H}})^2$ of the hole space for the half-filled pairing model, with $\delta = 1.0$ and different couplings g as indicated. The dash-dotted and dashed lines show analytical results for $\alpha = 1$ and $\alpha = 2$, respectively, and they are valid for values of t^2 as indicated. The color and shape of the markers indicate the coupling strength, and for a given coupling, identical markers show the results for one to twelve pairs. The entropy increases with the number of pairs and with increasing coupling strength. The figure is taken from Ref. (Gu et al., 2023), which I co-authored.

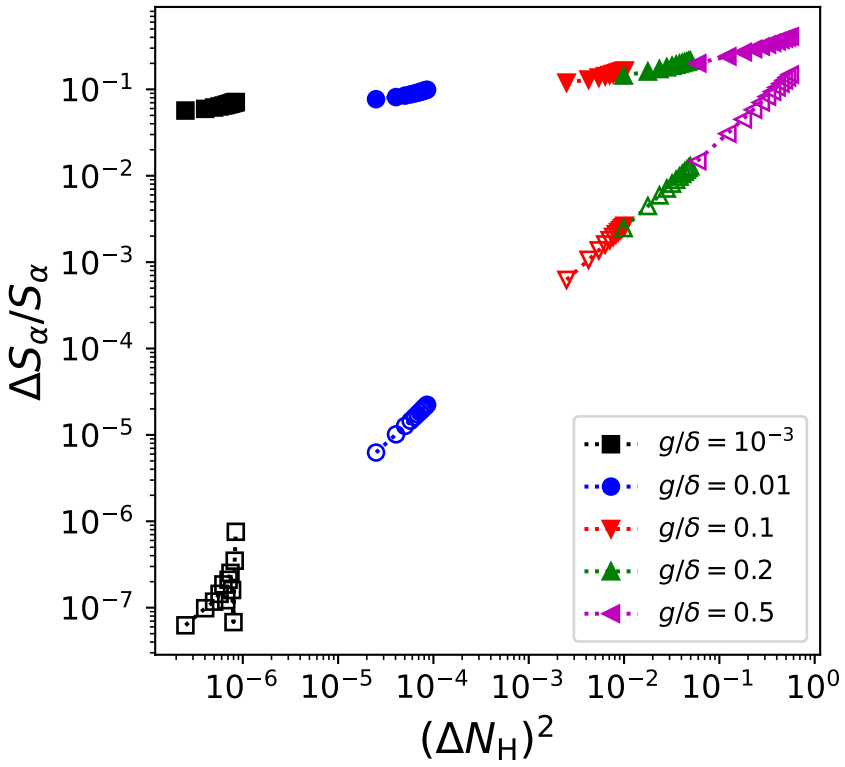


Figure 3.3: Absolute differences between numerical and analytical Rényi entropies for S_1 (full markers) and S_2 (hollow markers), normalized by the numerical entropy, versus the particle-number fluctuation $(\Delta N_{\mathrm{H}})^2$ of the hole space for the half-filled pairing model, with $\delta = 1.0$ and different couplings g as indicated. The color and shape of the markers indicate the coupling strength, and for a given coupling, identical markers show the results for one to twelve pairs. The figure is taken from Ref. (Gu et al., 2023), which I co-authored.

for $(\Delta N_{\mathrm{H}})^2 \to 0$. For S_2, the value of the absolute difference is as predicted of order S_2^2, shown in Eq. (3.2.14). Here, I apply the argument that the order of S_2 is similar to the order of $(\Delta N_{\mathrm{H}})^2$ which is proportional to t^2. We can see the deviations for S_2 results when $(\Delta N_{\mathrm{H}})^2 \to 0$, and this is explained as a result of the machine precision limit.

As we can see, t^2 is an important quantity as it links the relation between entanglement entropy and particle-number fluctuation. Figuring out the scaling problem of quantity t^2 will lead us to the scaling problem of entanglement entropy. Here, I provide the analytical discussion about t^2. For sufficiently small interaction, the CCD amplitudes t_{ij}^{ab} are well approximated by the MBPT2 results, given as

$$t_{ij}^{ab} \approx \frac{\langle ab|\hat{v}|ij\rangle}{\varepsilon_{ij}^{ab}} \ . \tag{3.3.2}$$

This approximation has been introduced in Subsec. 3.1.1 as a starting point for iteration calculation of amplitudes.

Then we have,

$$\begin{aligned} t^2 &= \frac{1}{4}\sum_{i=1}^{\frac{N}{2}}\sum_{a=\frac{N}{2}+1}^{\frac{\Omega}{2}} \frac{g^2}{4\delta^2(i-a)^2} \\ &\approx \frac{g^2}{16\delta^2}\sum_{i=1}^{\frac{N}{2}}\left[\int_{\frac{N}{2}+1}^{\frac{\Omega}{2}} \frac{1}{(i-a)^2}da\right] \\ &\approx \frac{g^2}{16\delta^2}\int_1^{\frac{N}{2}}\left[\frac{1}{i-\frac{\Omega}{2}} - \frac{1}{i-\frac{N}{2}-1}\right]di \\ &= \frac{g^2}{16\delta^2}\log\frac{N(\Omega-N)}{2(\Omega-2)} \\ &\approx \frac{g^2}{16\delta^2}\log\frac{N}{4} \ , \end{aligned} \tag{3.3.3}$$

where $N = \Omega/2$ for half-filled pairing model. In the second and the third line, the Euler–Maclaurin formula $\sum_{i=m}^{n} f(i) \approx \int_m^n f(x)dx$ is used to estimate the sums by the integrals. In the last line, the equation is valid when $N \gg 1$. More precise analytical results are given as

$$t^2 = \frac{g^2}{16\delta^2}\left[\frac{2}{N^2} + \frac{1}{4(N-1)^2} - \frac{1}{N-1} + \log\frac{N^2}{4(N-1)} + \frac{5}{4}\right] \ , \tag{3.3.4}$$

by using

$$\sum_{i=m}^{n} f(i) \approx \int_{m}^{n} f(x)dx + \frac{f(n)+f(m)}{2} \ .$$

Comparing both analytical results, the approximation (3.3.3) introduces an error of order $\mathcal{O}(N^0)$, which is negligible when $N \gg 1$.

I introduce the relative error of t^2 as

$$\varepsilon = \frac{\left| t^2 - \frac{g^2}{16\delta^2} \log \frac{N^2}{4(N-1)} \right|}{t^2} \ , \tag{3.3.5}$$

and show the result in Fig. 3.4. We can see that, for sufficiently small coupling strengths, Eq. (3.3.2) is valid. For $g = 0.1$, the metric nssd for t^2 is nssd(0.1) = 2.34 (nssd is defined in Eq. (2.5.3), with $v^{(e)}$ as the numerical results of t^2 and $v^{(t)}$ as the results calculated from MBPT2), which means the difference is larger than 20%. Therefore, for $\alpha \geq 2$, we have $S_\alpha \propto \log(N)$ for week interactions, and this agrees with expectations for a Fermi system in one dimension (Leschke et al., 2014).

3.3.2 Neutron Matter

The Hamiltonian of neutron matter is defined as

$$\hat{H} = \hat{H}_0 + \hat{H}_I = \sum_{i=1}^{N} \hat{t}_0 \left(r_i\right) + \sum_{i<j}^{N} \hat{v} \left(r_{ij}\right) \ . \tag{3.3.6}$$

This is a simple model of neutron matter with N neutrons, which only considers two-body interactions. The Hamiltonian consists of the kinetic energy $\hat{t}_0$ and the Minnesota potential $\hat{v}$ (Thompson et al., 1977). The Minnesota potential has a repulsive term and attractive short-range terms (in a $\exp(-r^2)$ format with respect to radial coordinates).

We formulate the neutron matter in discrete momentum states $|\vec{k}\rangle = |k_x, k_y, k_z\rangle$ of a cubic box with periodic boundary conditions. The discrete momentums are given as

$$k_n = \frac{2\pi n}{L} \ , \tag{3.3.7}$$

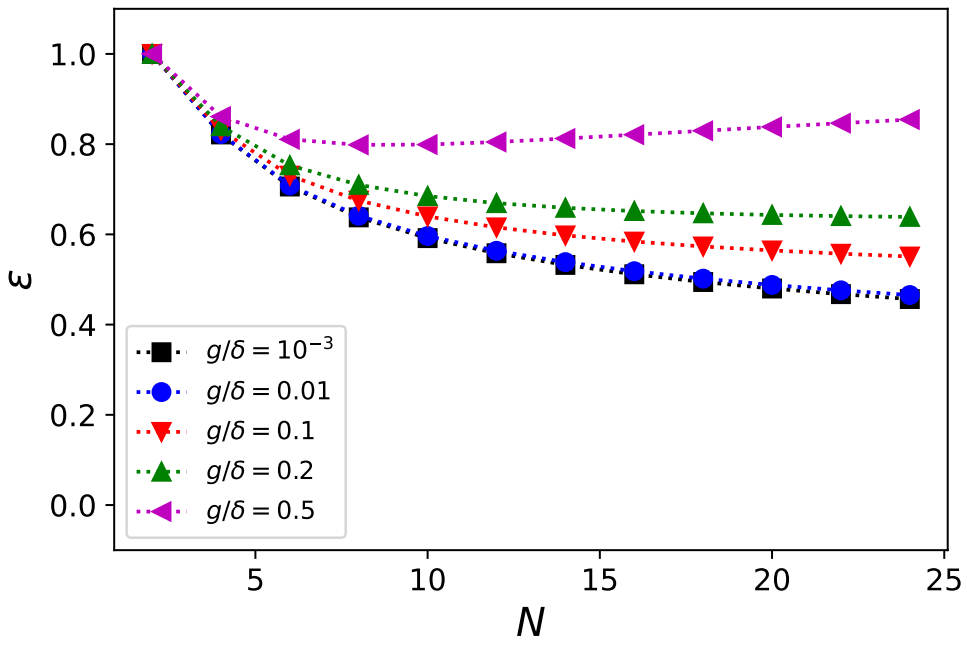


Figure 3.4: Relative error of the approximated t^2 value as a function of the number of particles, with $\delta = 1.0$ and $g = 1e-4, 1e-3, 1e-2, 1e-1, 2e-1, 5e-1$. The figure is taken from Ref. (Gu et al., 2023), which I co-authored.

with $n = 0, \pm 1, \ldots \pm N_{\max}$. Here, the size of the box is $L = (N/\rho)^{1/3}$ with ρ the density of neutron matter. The density is set to be the saturation density $\rho_0 \approx 0.08$ fm^{-3} in this calculation. $N_{\max}$ indicates the maximum number of possible discrete momentum, then the size of basis states grows as $(2N_{\max}+1)^3$, with the spin degeneracy for each momentum state as $g_s = 2$.

With this basis, the reference

$$|\Phi\rangle = \prod_{i=1}^{N} = \hat{a}_i^\dagger |0\rangle$$

is obtained by filling out the basis with the lowest momentums (below the Fermi level), and therefore the momentum space are partitioned into hole space (states below the Fermi level) and particle space (states above the Fermi level). The normal ordered Hamiltonian based on this reference is written as

$$\hat{H}_{\mathrm{N}} = \sum_{pq} f_q^p \left\{\hat{a}_p^\dagger \hat{a}_q\right\} + \frac{1}{4}\sum_{pqrs} \left\langle \vec{k}_p \vec{k}_q | \hat{v} | \vec{k}_r \vec{k}_s \right\rangle \left\{\hat{a}_p^\dagger \hat{a}_q^\dagger \hat{a}_s \hat{a}_r\right\} \ , \tag{3.3.8}$$

with

$$f_q^p = \left\langle \vec{k}_p | \hat{t_0} | \vec{k}_q \right\rangle + \sum_i \left\langle \vec{k}_p \vec{k}_i | \hat{v} | \vec{k}_q \vec{k}_i \right\rangle \ ,$$

The operators $a_p^\dagger$ and a_p create and annihilate a neutron in momentum state $|\vec{k}_p\rangle$, respectively. Reference energy is defined as

$$E_{\mathrm{ref}} = \sum_i \left\langle \vec{k}_i | t_0 | \vec{k}_i \right\rangle + \frac{1}{2}\sum_{i,j} \left\langle \vec{k}_i \vec{k}_j | v | \vec{k}_i \vec{k}_j \right\rangle \ , \tag{3.3.9}$$

In the two-body interaction term, the momentum is conserved, $\vec{k}_p + \vec{k}_q = \vec{k}_r + \vec{k}_s$ that forbids single-particle excitations. The calculation is based on the CCD method, and the neutron matter systems with $N = 14$, 38, 54, 66, and 114 (magic numbers) are calculated.

Ref. (Hagen et al., 2014a) calculated the neutron matter with the CCD approximation, which only uses the particle-particle and hole-hole ladders ($\mathrm{CCD_{ladd}}$). It shows results from $\mathrm{CCD_{ladd}}$ are less accurate but very close to the results from the CCD, and it shows a good

agreement between results of $\mathrm{CCD}_{\mathrm{ladd}}$ and virtually exact results from the auxiliary field diffusion Monte Carlo (AFDMC) method. In this calculation, this simplified version is used, and matrix elements of the effective Hamiltonian $e^{-\hat{T}_2} H_{\mathrm{N}} e^{-\hat{T}_2}$ are

$$\begin{aligned}
\bar{H}_{ij}^{ab} &= \left\langle \vec{k}_a \vec{k}_b | v | \vec{k}_i \vec{k}_j \right\rangle \\
&+ P(ab) \sum_c f_c^b t_{ij}^{ac} \\
&- P(ij) \sum_k f_j^k t_{ik}^{ab} \\
&+ \frac{1}{2} \sum_{cd} \left\langle \vec{k}_a \vec{k}_b | v | \vec{k}_c \vec{k}_d \right\rangle t_{ij}^{cd} \\
&+ \frac{1}{2} \sum_{kl} \left\langle \vec{k}_k \vec{k}_l | v | \vec{k}_i \vec{k}_j \right\rangle t_{kl}^{ab} \ .
\end{aligned} \tag{3.3.10}$$

Compared to the amplitudes equation of the CCD in Eq. (3.1.21), Eq. (3.3.10) contains only the first five terms. Solving the equation $\bar{H}_{ij}^{ab} = 0$ yields the amplitudes t_{ij}^{ab} and the calculation follows the CCD calculations of neutron matter in Ref. (Lietz et al., 2017), with the codes in Python notebook (T. Papenbrock, 2018).

Fig. 3.5 shows the correlation energy per neutron as a function of neutron number. The correlation energy is defined as the difference between the CCD energy (3.1.13) and the reference energy (3.3.9). Different colored and shaped markers denote the momentum space sizes $N_{\max}$. We see that the correlation energy depends weakly on neutron number and becomes approximately constant for large model space $N_{\max} = 5$. The results for $N = 54$ disagree with the statement and exhibit peaks. This results from the finite-size effects, which can be reduced by using twist-averaged boundary conditions (Gros, 1996; Lin et al., 2001; Hagen et al., 2014a).

For $N_{\max} = 5$, the CCD energies are 9.5, 8.2, 8.3, 9.1, 9.6 MeV for $N = 14$, 38, 54, 66, 114 respectively. These energies are close to results from more sophisticated theories with three-nucleon forces included (giving 9-10 MeV per neutron) (Hebeler et al., 2013), and they are very close to results from theory with nucleon-nucleon forces only (giving about 8.7 MeV per neutron) (Hebeler and Schwenk, 2010).

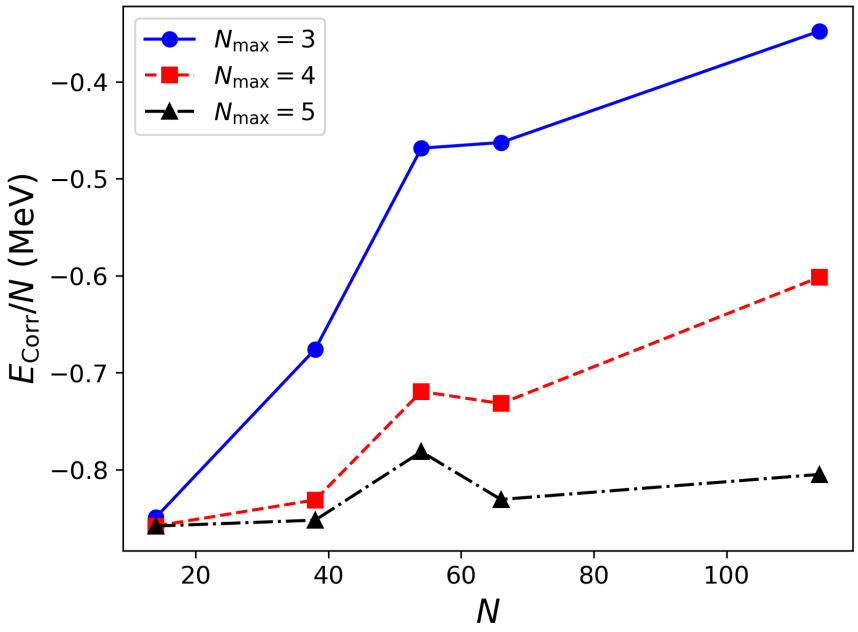


Figure 3.5: Correlation energy per neutron as a function of the neutron number $N = 14$, 38, 54, 66, 114 with different basis sizes $N_{\max}$. The figure is taken from Ref. (Gu et al., 2023), which I co-authored.

Tab. 3.1 gives the results of t^2 Eq. (3.2.6) for different $N_{\max}$, that $t^2 \ll 1$ is only satisfied for $N \lesssim 66$. Since the analytical results are constrained to weak interactions, only those neutron matter systems with $N \leq 66$ are considered for entanglement entropy discussion.

Figure 3.6 shows Rényi entropies S_α of neutron matter as a function of the neutron number N. Figure 3.7 shows the S_α as a function of the particle number fluctuations $(\Delta N_{\mathrm{H}})^2$ of the hole space. In both figures, Rényi entropies with $\alpha = 1$, 2, 4, and 8 are given. The size of momentum space is $N_{\max} = 5$. Entanglement entropies grow linearly with respect to the neutron number (and $N = 54$ is again an outlier), which indicates entanglement entropy satisfies a volume law for neutron matter in momentum space. Also, we can see the relation between entanglement entropies, and particle number fluctuation is approximately linear.

3.4 Summary

This chapter studies entanglement entropies of many-body nuclear systems and their scaling laws. The space partition separates the whole Hilbert space into hole space and particle space. The former and latter contain states below and above the Fermi level, respectively. The Fermi level is defined by filling the particles into single-particle states with the lowest energies.

This chapter shows the analytical results of Rényi entropy S_α (1.3.3) (von Neumann entropy (1.3.1) S_1 as a special case of Rényi entropy), the particle number fluctuation of hole space and the depletion number of the reference states. The analytical calculations are based on CCD approximation (3.2.3). The analytical Rényi entropy S_1 and S_α (with $\alpha > 1$), for weak interaction ($t^2 \ll 1$), are given in Eq. (3.2.13) and Eq. (3.2.14), respectively. And their asymptotic behaviors when $t^2 \to 0$ are given in Eq. (3.2.15), which gives us $S_1 \to t^2 \log t^2$ and $S_\alpha \propto t^2$ (with $\alpha > 1$). The analytical results of particle number fluctuation and depletion number of hole space are given in Eq. (3.2.19) and Eq. (3.2.20). The relation is $\frac{1}{4}(\Delta N_{\mathrm{H}})^2 \approx \frac{1}{2}(\delta N_{\mathrm{H}}) \approx t^2$. Therefore, the linear relation between S_α (with $\alpha > 1$) and $(\Delta N_{\mathrm{H}})^2$ is obtained, for systems with sufficiently small interactions.

This chapter shows the numerical results of the pairing model, based on the CCD method, and the results are shown in Fig. 3.2, which shows the agreement with the analytical results

Table 3.1: Numerical values for t^2 for different neutron matter models $N = 14$, 38, 54, 66, 114 with different basis size $N_{\max}$.

	$N = 14$	$N = 38$	$N = 54$	$N = 66$	$N = 114$
$N_{\max} = 3$	0.106	0.298	0.246	0.475	1.239
$N_{\max} = 4$	0.106	0.322	0.299	0.557	1.431
$N_{\max} = 5$	0.106	0.324	0.308	0.581	1.565

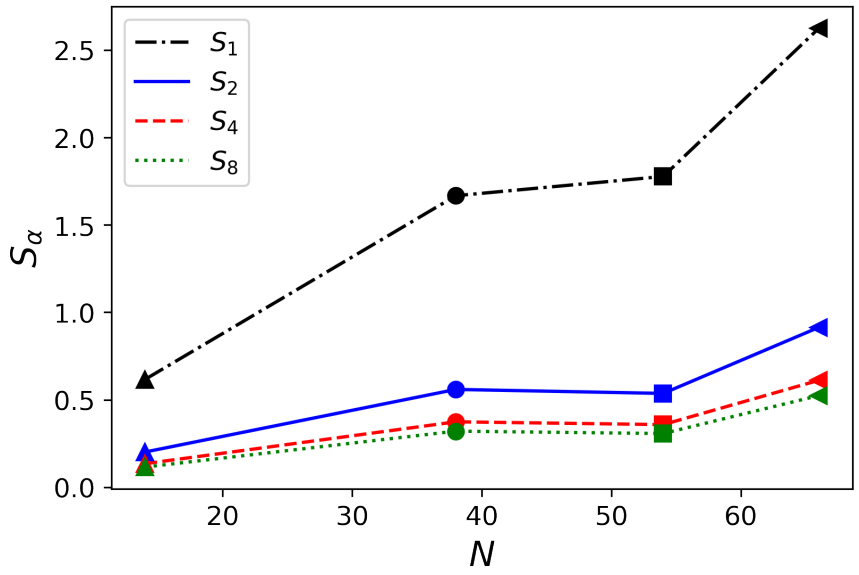


Figure 3.6: Entanglement entropy versus the neutron numbers $N = 14$ (triangle_up), $N = 38$ (circle), $N = 54$ (square), $N = 66$ (triangle_left), $N_{\max} = 5$ of momentum space. The figure is taken from Ref. (Gu et al., 2023), which I co-authored.

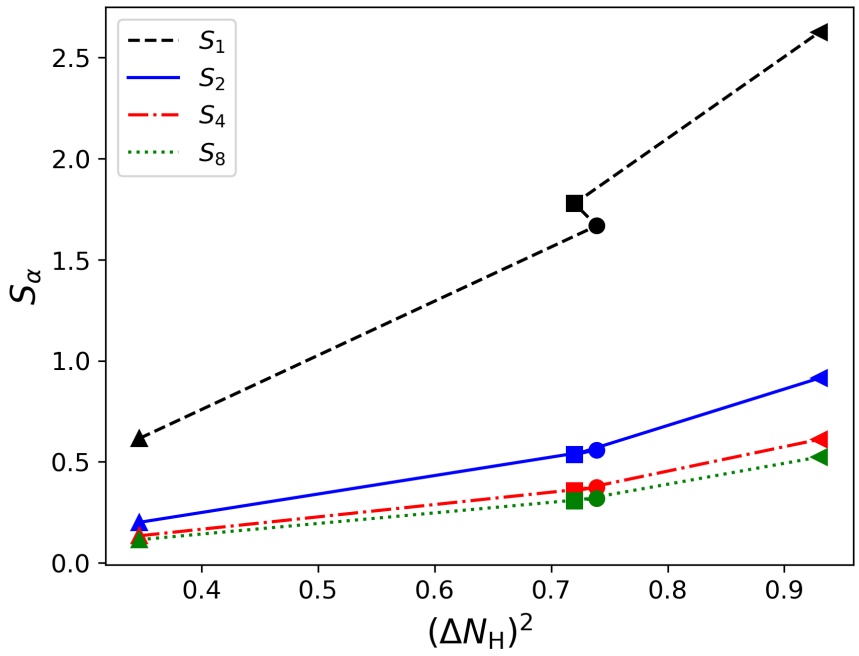


Figure 3.7: Entanglement entropy versus the particle number fluctuation with $N = 14$ (triangle up), $N = 38$ (circle), $N = 54$ (square), $N = 66$ (triangle left), $N_{\mathrm{max}} = 5$ of momentum space. The figure is taken from Ref. (Gu et al., 2023), which I co-authored.

$(\Delta N_{\mathrm{H}})^2 \propto S_\alpha$. Also, the analytical discussion of the quantity t^2 (3.3.3) is given based on the MBPT2 (3.3.2). Its numerical results (shown in Fig. 3.4) indicate $S_\alpha \propto \ln N$ for $\alpha > 2$, which satisfies the area law for Fermi system in one dimension.

The numerical results of the neutron matter (with neutron number $N = 14$, 38, 54, 66, and 114) are given. The neutron matter model is less realistic, as it only contains two-body interactions using the Minnesota potential. The calculation is based on a CCD approximation method (which only considers ladder diagrams) in momentum space. The results are shown in Fig. 3.5 and Fig. 3.6, and they show that S_α is approximately proportional to the neutron number and $(\Delta N_{\mathrm{H}})^2$. The latter results are less accurate than that of the pairing model. This is because the size of the $\hat{T}_2$ amplitudes is sizable, i.e., the condition $t^2 < 1$ is satisfied but not the condition $t^2 \ll 1$. The results indicate that the entanglement entropy of neutron matter scales as a volume law instead of an area law. Reference (Gu et al., 2023) also provides the numerical calculation of finite nuclei (for closed-shell nuclei ^{4}He, ^{16}O, ^{40}Ca, and ^{100}Sn) with the CCSD method. The results show that the depletion number approximately linearly grows with the mass number, which indicates a volume law.

To summarize, for a nuclear many-body system with sufficiently weak interactions, a volume law is preferred to describe the scaling of entanglement entropy.

Chapter 4

Summary and Outlook

In summary, this dissertation reports the preliminary application of quantum computing and quantum information in nuclear physics in two specific aspects, including the excited state preparation quantum algorithms and a discussion about the scaling laws of entanglement entropies in nuclear systems.

In this dissertation, I show details of the time-dependent method and the LCU-based method and their implementations on a quantum processor unit with a simple model of $n(p,d)\gamma$ reaction. The results show both methods are practicable and feasible. As the efficiency of both methods is constrained by the success probability, I am interested in utilizing the amplitude amplification technique, a general technique that can enhance quantum algorithms, to increase the success probability of both methods by using $O(1/\sqrt{P_s})$ additional unitary gates.

In this dissertation, the toy models are used to test the algorithms due to the limited performance of quantum processors, and the physics systems studied are initialized in the ground states. For further investigation, it is interesting to study more realistic physics problems and to combine the state preparation algorithms with algorithms that help us project the quantum systems to the ground states.

I also show the entanglement entropies of many-body nuclear systems and argue that a volume law is preferred to describe the scaling of entanglement entropy for a nuclear many-body system with sufficiently weak interactions. This dissertation focuses on the spherical states of quantum systems. For future work, it is interesting to extend the study

of deformed reference states, investigate how much entanglement the symmetry projection would give, and further explore the potential of quantum information as a guiding tool in our understanding of nuclear physics.

Bibliography

5qubit backed: IBM Q team (2020). IBM Vigo backend specification v1.0.2. Retrieved from https://quantum-computing.ibm.com. viii, ix, x, xi, 14, 15, 43, 58, 59, 60, 61

Abrams, D. S. and Lloyd, S. (1997). Simulation of many-body fermi systems on a universal quantum computer. *Physical Review Letters*, 79(13):2586. 3

Adelberger, E. G., García, A., Robertson, R. G. H., Snover, K. A., Balantekin, A. B., Heeger, K., Ramsey-Musolf, M. J., Bemmerer, D., Junghans, A., Bertulani, C. A., Chen, J.-W., Costantini, H., Prati, P., Couder, M., Uberseder, E., Wiescher, M., Cyburt, R., Davids, B., Freedman, S. J., Gai, M., Gazit, D., Gialanella, L., Imbriani, G., Greife, U., Hass, M., Haxton, W. C., Itahashi, T., Kubodera, K., Langanke, K., Leitner, D., Leitner, M., Vetter, P., Winslow, L., Marcucci, L. E., Motobayashi, T., Mukhamedzhanov, A., Tribble, R. E., Nollett, K. M., Nunes, F. M., Park, T.-S., Parker, P. D., Schiavilla, R., Simpson, E. C., Spitaleri, C., Strieder, F., Trautvetter, H.-P., Suemmerer, K., and Typel, S. (2011). Solar fusion cross sections. ii. the¡mml:math xmlns:mml="http://www.w3.org/1998/math/mathml" display="inline"¿¡mml:mi¿p¡/mml:mi¿¡mml:mi¿p¡/mml:mi¿¡/mml:math¿chain and cno cycles. *Reviews of Modern Physics*, 83(1):195–245. 47

Arute, F., Arya, K., Babbush, R., Bacon, D., Bardin, J., Barends, R., Biswas, R., Boixo, S., Brandao, F., Buell, D., Burkett, B., Chen, Y., Chen, J., Chiaro, B., Collins, R., Courtney, W., Dunsworth, A., Farhi, E., Foxen, B., Fowler, A., Gidney, C. M., Giustina, M., Graff, R., Guerin, K., Habegger, S., Harrigan, M., Hartmann, M., Ho, A., Hoffmann, M. R., Huang, T., Humble, T., Isakov, S., Jeffrey, E., Jiang, Z., Kafri, D., Kechedzhi, K., Kelly, J., Klimov, P., Knysh, S., Korotkov, A., Kostritsa, F., Landhuis, D., Lindmark, M., Lucero, E., Lyakh, D., Mandrà, S., McClean, J. R., McEwen, M., Megrant, A., Mi, X., Michielsen, K., Mohseni, M., Mutus, J., Naaman, O., Neeley, M., Neill, C., Niu, M. Y., Ostby, E., Petukhov, A., Platt, J., Quintana, C., Rieffel, E. G., Roushan, P., Rubin, N., Sank, D., Satzinger, K. J., Smelyanskiy, V., Sung, K. J., Trevithick, M., Vainsencher, A., Villalonga, B., White, T., Yao, Z. J., Yeh, P., Zalcman, A., Neven, H., and Martinis, J. (2019). Quantum supremacy using a programmable superconducting processor. *Nature*, 574:505–510. 4

Atzori, M. and Sessoli, R. (2019). The second quantum revolution: Role and challenges of molecular chemistry. *Journal of the American Chemical Society*. 7

Babbush, R., Berry, D. W., and Neven, H. (2019). Quantum simulation of the sachdev-ye-kitaev model by asymmetric qubitization. *Phys. Rev. A*, 99:040301. 56

Backes, S., Murakami, Y., Sakai, S., and Arita, R. (2023). Dynamical mean-field theory for the hubbard-holstein model on a quantum device. *Physical Review B*, 107(16). 4

Bai, D. and Ren, Z. (2022). Entanglement generation in few-nucleon scattering. *Phys. Rev. C*, 106:064005. 9

Barenco, A., Bennett, C. H., Cleve, R., DiVincenzo, D. P., Margolus, N., Shor, P., Sleator, T., Smolin, J. A., and Weinfurter, H. (1995). Elementary gates for quantum computation. *Phys. Rev. A*, 52:3457–3467. 5, 14, 29, 53

Barthel, T., Chung, M.-C., and Schollwöck, U. (2006a). Entanglement scaling in critical two-dimensional fermionic and bosonic systems. *Physical Review A*, 74(2). 10

Barthel, T., Dusuel, S., and Vidal, J. (2006b). Entanglement entropy beyond the free case. *Phys. Rev. Lett.*, 97:220402. 10

Bartlett, R. J. and Musiał, M. (2007). Coupled-cluster theory in quantum chemistry. *Rev. Mod. Phys.*, 79:291–352. 64

Batista, C. D. and Ortiz, G. (2001). Generalized jordan-wigner transformations. *Physical Review Letters*, 86(6):1082–1085. 6

Beane, S. R., Kaplan, D. B., Klco, N., and Savage, M. J. (2019). Entanglement suppression and emergent symmetries of strong interactions. *Phys. Rev. Lett.*, 122:102001. 9

Benavides-Riveros, C. L., Lathiotakis, N. N., and Marques, M. A. L. (2017). Towards a formal definition of static and dynamic electronic correlations. *Phys. Chem. Chem. Phys.*, 19:12655–12664. 2

Bishop, R. F. (1991). An overview of coupled cluster theory and its applications in physics. *Theoretical Chemistry Accounts: Theory, Computation, and Modeling (Theoretica Chimica Acta)*, 80:95–148. 64

Boguslawski, K. and Tecmer, P. (2014). Orbital entanglement in quantum chemistry. *International Journal of Quantum Chemistry*, 115(19):1289–1295. 9

Boguslawski, K., Tecmer, P., Legeza, Ö., and Reiher, M. (2012). Entanglement measures for single- and multireference correlation effects. *The Journal of Physical Chemistry Letters*, 3(21):3129–3135. 9

Bravyi, S., Gosset, D., and König, R. (2018). Quantum advantage with shallow circuits. *Science*, 362(6412):308–311. 4

Bravyi, S. B. and Kitaev, A. Y. (2002). Fermionic quantum computation. *Annals of Physics*, 298(1):210–226. 5

Bremner, M. J., Mora, C., and Winter, A. (2009). Are random pure states useful for quantum computation? *Phys. Rev. Lett.*, 102:190502. 8

Brun, T., Devetak, I., and Hsieh, M.-H. (2006). Correcting quantum errors with entanglement. *Science*, 314(5798):436–439. 7

Bulgac, A., Kafker, M., and Abdurrahman, I. (2022). Measures of complexity and entanglement in fermionic many-body systems. *arXiv e-prints*, page arXiv:2203.04843. 9

Buluta, I. and Nori, F. (2009). Quantum simulators. *Science*, 326(5949):108–111. 3

Buscemi, F. (2012). All entangled quantum states are nonlocal. *Phys. Rev. Lett.*, 108:200401. 10

Cao, Y., Romero, J., Olson, J. P., Degroote, M., Johnson, P. D., Kieferová, M., Kivlichan, I. D., Menke, T., Peropadre, B., Sawaya, N. P. D., Sim, S., Veis, L., and Aspuru-Guzik, A. (2019). Quantum chemistry in the age of quantum computing. *Chemical Reviews*, 119(19):10856–10915. 4

Carlson, J., Savage, M. J., Gerber, R., Antypas, K., Bard, D., Coffey, R., Dart, E., Dosanjh, S., Hack, J., Monga, I., Papka, M. E., Riley, K., Rotman, L., Straatsma, T., Wells, J., Avakian, H., Ayyad, Y., Bass, S. A., Bazin, D., Boehnlein, A., Bollen, G., Broussard, L. J., Calder, A., Couch, S., Couture, A., Cromaz, M., Detmold, W., Detwiler, J., Duan, H., Edwards, R., Engel, J., Fryer, C., Fuller, G. M., Gandolfi, S., Gavalian, G., Georgobiani, D., Gupta, R., Gyurjyan, V., Hausmann, M., Heyes, G., Hix, W. R., Ito, M., Jansen, G., Jones, R., Joo, B., Kaczmarek, O., Kasen, D., Kostin, M., Kurth, T., Lauret, J., Lawrence, D., Lin, H.-W., Lin, M., Mantica, P., Maris, P., Messer, B., Mittig, W., Mosby, S., Mukherjee, S., Nam, H. A., Navrátil, P., Nazarewicz, W., Ng, E., O'Donnell, T., Orginos, K., Pellemoine, F., Petreczky, P., Pieper, S. C., Pinkenburg, C. H., Plaster, B., Porter, R. J., Portillo, M., Pratt, S., Purschke, M. L., Qiang, J., Quaglioni, S., Richards, D., Roblin, Y., Schenke, B., Schiavilla, R., Schlichting, S., Schunck, N., Steinbrecher, P., Strickland, M., Syritsyn, S., Terzic, B., Varner, R., Vary, J., Wild, S., Winter, F., Zegers, R., Zhang, H., Ziegler, V., and Zingale, M. (2022). Nuclear physics exascale requirements review: An office of science review sponsored jointly by advanced scientific computing research and nuclear physics, june 15 - 17, 2016, gaithersburg, maryland. 3

Childs, A. M., Kothari, R., and Somma, R. D. (2017). Quantum algorithm for systems of linear equations with exponentially improved dependence on precision. *SIAM Journal on Computing*, 46(6):1920–1950. 26

Childs, A. M. and Wiebe, N. (2012). Hamiltonian simulation using linear combinations of unitary operations. 12(11–12):901–924. 25, 26, 30

Čížek, J. (1966). On the Correlation Problem in Atomic and Molecular Systems. Calculation of Wavefunction Components in Ursell-Type Expansion Using Quantum-Field Theoretical Methods. *J. Chem. Phys.*, 45(11):4256–4266. 64

Čížek, J. (2007). *On the Use of the Cluster Expansion and the Technique of Diagrams in Calculations of Correlation Effects in Atoms and Molecules*, pages 35–89. John Wiley & Sons, Inc. 64

Čížek, J. and Paldus, J. (1971). Correlation problems in atomic and molecular systems III. Rederivation of the coupled-pair many-electron theory using the traditional quantum chemical methods. *International Journal of Quantum Chemistry*, 5(4):359–379. 64

Coester, F. and Kümmel, H. (1960). Short-range correlations in nuclear wave functions. *Nuclear Physics*, 17(0):477 – 485. 64

Coleman, P. (2015). *Introduction to Many-Body Physics*. Cambridge University Press. 6

Crawford, T. D. and Schaefer, H. F. (2007). An introduction to coupled cluster theory for computational chemists. *Reviews in Computational Chemistry*, 14:33–136. 67

Cremer, D. (2013). From configuration interaction to coupled cluster theory: The quadratic configuration interaction approach. *Wiley Interdisciplinary Reviews: Computational Molecular Science*, 3. 66

Daley, A. J., Bloch, I., Kokail, C., Flannigan, S., Pearson, N., Troyer, M., and Zoller, P. (2022). Practical quantum advantage in quantum simulation. *Nature*, 607:667 – 676. 4

Dalzell, A. M., McArdle, S., Berta, M., Bienias, P., Chen, C.-F., Gilyén, A., Hann, C. T., Kastoryano, M. J., Khabiboulline, E. T., Kubica, A., Salton, G., Wang, S., and Brandão, F. G. S. L. (2023). Quantum algorithms: A survey of applications and end-to-end complexities. 4

Derby, C. and Klassen, J. (2020). Low weight fermionic encodings for lattice models. *arXiv: Quantum Physics*. 5

Deutsch, D. (1989). Quantum computational networks. *Proceedings of the Royal Society of London. Series A, Mathematical and Physical Sciences*, 425:73–90. 5

Deutsch, D., Barenco, A., and Ekert, A. (1995). Universality in quantum computation. *Proceedings of the Royal Society of London. Series A: Mathematical and Physical Sciences*, 449(1937):669–677. 5

Deutsch, I. H. (2020). Harnessing the power of the second quantum revolution. *PRX Quantum*, 1:020101. 7

Ding, L., Knecht, S., and Schilling, C. (2023). Quantum information-assisted complete active space optimization (qicas). *The Journal of Physical Chemistry Letters*, 14(49):11022–11029. 9

Dowling, J. P. and Milburn, G. J. (2003). Quantum technology: The second quantum revolution. *Philosophical Transactions: Mathematical, Physical and Engineering Sciences*, 361(1809):1655–1674. 7

Dukelsky, J., Pittel, S., and Sierra, G. (2004). Colloquium: Exactly solvable richardson-gaudin models for many-body quantum systems. *Rev. Mod. Phys.*, 76:643–662. 81

Dumitrescu, E. F., McCaskey, A. J., Hagen, G., Jansen, G. R., Morris, T. D., Papenbrock, T., Pooser, R. C., Dean, D. J., and Lougovski, P. (2018). Cloud Quantum Computing of an Atomic Nucleus. *ArXiv e-prints*. 4, 117

Duperrouzel, C., Tecmer, P., Boguslawski, K., Barcza, G., Legeza, Ö., and Ayers, P. (2015). A quantum informational approach for dissecting chemical reactions. *Chemical Physics Letters*, 621:160–164. 9

Einstein, A., Podolsky, B., and Rosen, N. (1935). Can quantum-mechanical description of physical reality be considered complete? *Phys. Rev.*, 47:777–780. 7

Eisert, J., Cramer, M., and Plenio, M. B. (2010). Colloquium: Area laws for the entanglement entropy. *Rev. Mod. Phys.*, 82:277–306. 9, 10, 63, 72

Ekert, A. and Jozsa, R. (1998). Quantum algorithms: entanglement–enhanced information processing. *Philosophical Transactions of the Royal Society of London. Series A: Mathematical, Physical and Engineering Sciences*, 356(1743):1769–1782. 8

Endo, S., Benjamin, S. C., and Li, Y. (2018). Practical quantum error mitigation for near-future applications. *Phys. Rev. X*, 8:031027. 117

Endo, S., Cai, Z., Benjamin, S. C., and Yuan, X. (2021). Hybrid quantum-classical algorithms and quantum error mitigation. *Journal of the Physical Society of Japan*, 90(3):032001. 7

Faba, J., Martín, V., and Robledo, L. (2021). Correlation energy and quantum correlations in a solvable model. *Phys. Rev. A*, 104:032428. 10

Feynman, R. P. (1982). Simulating physics with computers. *International journal of theoretical physics*, 21(6/7):467–488. 3

Fradkin, E. (1989). Jordan-wigner transformation for quantum-spin systems in two dimensions and fractional statistics. *Phys. Rev. Lett.*, 63:322–325. 6

Georgi, H. (1993). Effective field theory. *Annual Review of Nuclear and Particle Science*, 43(1):209–252. 1

Gigena, N. and Rossignoli, R. (2015). Entanglement in fermion systems. *Phys. Rev. A*, 92:042326. 71

Gioev, D. and Klich, I. (2006). Entanglement entropy of fermions in any dimension and the widom conjecture. *Phys. Rev. Lett.*, 96:100503. 10

Gros, C. (1996). Control of the finite-size corrections in exact diagonalization studies. *Phys. Rev. B*, 53:6865–6868. 88

Gross, D., Flammia, S. T., and Eisert, J. (2009). Most quantum states are too entangled to be useful as computational resources. *Phys. Rev. Lett.*, 102:190501. 8

Gu, C., Sun, Z. H., Hagen, G., and Papenbrock, T. (2023). Entanglement entropy of nuclear systems. *Physical Review C*, 108(5). xi, xii, xiii, 4, 11, 63, 73, 74, 82, 83, 86, 89, 91, 92, 93

Hagen, G., Papenbrock, T., Ekström, A., Wendt, K. A., Baardsen, G., Gandolfi, S., Hjorth-Jensen, M., and Horowitz, C. J. (2014a). Coupled-cluster calculations of nucleonic matter. *Phys. Rev. C*, 89:014319. 87, 88

Hagen, G., Papenbrock, T., Hjorth-Jensen, M., and Dean, D. J. (2014b). Coupled-cluster computations of atomic nuclei. *Rep. Prog. Phys.*, 77(9):096302. 64

Harrow, A. W. and Montanaro, A. (2017). Quantum computational supremacy. *Nature*, 549(7671):203–209. 4

Hebeler, K., Lattimer, J. M., Pethick, C. J., and Schwenk, A. (2013). Equation of state and neutron star properties constrained by nucl. phys. and observation. *The Astrophysical Journal*, 773(1):11. 88

Hebeler, K. and Schwenk, A. (2010). Chiral three-nucleon forces and neutron matter. *Phys. Rev. C*, 82:014314. 88

Henderson, L. and Vedral, V. (2001). Classical, quantum and total correlations. *Journal of Physics A: Mathematical and General*, 34(35):6899. 8

Hergert, H. (2020). A guided tour of ab initio nuclear many-body theory. *Frontiers in Physics*, 8. 2

Herrmann, N., Arya, D., Doherty, M. W., Mingare, A., Pillay, J. C., Preis, F., and Prestel, S. (2023). Quantum utility – definition and assessment of a practical quantum advantage. In *2023 IEEE International Conference on Quantum Software (QSW)*. IEEE. 4

Holevo, A. S. (1973). Bounds for the quantity of information transmitted by a quantum communication channel. *Problemy Peredachi Informatsii*, 9:3–11. 4

Holland, E. T., Wendt, K. A., Kravvaris, K., Wu, X., Ormand, W. E., DuBois, J. L., Quaglioni, S., and Pederiva, F. (2020). Optimal control for the quantum simulation of nuclear dynamics. *Physical Review A*, 101(6). 4

Horodecki, R., Horodecki, P., Horodecki, M., and Horodecki, K. (2009). Quantum entanglement. *Rev. Mod. Phys.*, 81:865–942. 7

Huerta, L. and Zanelli, J. (1993). Bose-fermi transformation in three-dimensional space. *Phys. Rev. Lett.*, 71:3622–3624. 6

Jansen, G. R., Engel, J., Hagen, G., Navratil, P., and Signoracci, A. (2014). *Ab Initio* coupled-cluster effective interactions for the shell model: Application to neutron-rich oxygen and carbon isotopes. *Phys. Rev. Lett.*, 113:142502. 64

Johnson, C. W. and Gorton, O. C. (2022). Proton-neutron entanglement in the nuclear shell model. *arXiv e-prints*, page arXiv:2210.14338. 9

Johnson, T. H., Clark, S. R., and Jaksch, D. (2014). What is a quantum simulator? *EPJ Quantum Technology*, 1(1):10. 3

Jordan, P. and Wigner, E. P. (1928). About the Pauli exclusion principle. *Z. Phys.*, 47:631–651. 5

Jozsa, R. (2006). On the simulation of quantum circuits. 8

Jozsa, R. and Linden, N. (2003). On the role of entanglement in quantum-computational speed-up. *Proceedings of the Royal Society of London. Series A: Mathematical, Physical and Engineering Sciences*, 459(2036):2011–2032. 8

Kandala, A., Mezzacapo, A., Temme, K., Takita, M., Brink, M., Chow, J. M., and Gambetta, J. M. (2017). Hardware-efficient variational quantum eigensolver for small molecules and quantum magnets. *Nature*, 549(7671):242–246. 116

Kaplan, D. B. (2005). Five lectures on effective field theory. 1

Kaplan, D. B., Klco, N., and Roggero, A. (2017). Ground States via Spectral Combing on a Quantum Computer. *ArXiv e-prints*. 4

Kiss, O., Grossi, M., Lougovski, P., Sanchez, F., Vallecorsa, S., and Papenbrock, T. (2022). Quantum computing of the ^{6}Li nucleus via ordered unitary coupled clusters. *Phys. Rev. C*, 106:034325. 4

Klco, N., Dumitrescu, E. F., McCaskey, A. J., Morris, T. D., Pooser, R. C., Sanz, M., Solano, E., Lougovski, P., and Savage, M. J. (2018). Quantum-Classical Computations of Schwinger Model Dynamics using Quantum Computers. *ArXiv e-prints*. 4

Klich, I. (2006). Lower entropy bounds and particle number fluctuations in a fermi sea. *Journal of Physics A: Mathematical and General*, 39(4):L85–L91. 10, 79, 80

Kowalski, K. and Bauman, N. P. (2023). Quantum flow algorithms for simulating many-body systems on quantum computers. *Phys. Rev. Lett.*, 131:200601. 4

Krumnow, C., Veis, L., Legeza, Ö., and Eisert, J. (2016). Fermionic orbital optimization in tensor network states. *Physical Review Letters*, 117(21). 9

Kruppa, A. T., Kovács, J., Salamon, P., Legeza, Ö., and Zaránd, G. (2022). Entanglement and seniority. *Phys. Rev. C*, 106:024303. 9

Kruppa, A. T., Kovács, J., Salamon, P., and Legeza, Ö. (2021). Entanglement and correlation in two-nucleon systems. *Journal of Physics G: Nuclear and Particle Physics*, 48(2):025107. 9

Kümmel, H., Lührmann, K. H., and Zabolitzky, J. G. (1978). Many-fermion theory in expS- (or coupled cluster) form. *Physics Reports*, 36(1):1 – 63. 64

Lacroix, D., Balantekin, A. B., Cervia, M. J., Patwardhan, A. V., and Siwach, P. (2022). Role of non-gaussian quantum fluctuations in neutrino entanglement. *Phys. Rev. D*, 106:123006. 9

Laflorencie, N. (2016). Quantum entanglement in condensed matter systems. *Physics Reports*, 646:1–59. 9

Lee, S., Lee, J., Zhai, H., Tong, Y., Dalzell, A. M., Kumar, A., Helms, P., Gray, J., Cui, Z.-H., Liu, W., Kastoryano, M., Babbush, R., Preskill, J., Reichman, D. R., Campbell, E. T., Valeev, E. F., Lin, L., and Chan, G. K.-L. (2023). Evaluating the evidence for exponential quantum advantage in ground-state quantum chemistry. *Nature Communications*, 14(1). 4

Legeza, Ö., Veis, L., Poves, A., and Dukelsky, J. (2015). Advanced density matrix renormalization group method for nuclear structure calculations. *Phys. Rev. C*, 92:051303. 9, 71

Lepage, P. (1997). How to renormalize the schrodinger equation. 1

Leschke, H., Sobolev, A. V., and Spitzer, W. (2014). Scaling of rényi entanglement entropies of the free fermi-gas ground state: A rigorous proof. *Phys. Rev. Lett.*, 112:160403. 10, 85

Li, Y. and Benjamin, S. C. (2017). Efficient variational quantum simulator incorporating active error minimization. *Phys. Rev. X*, 7:021050. 7, 117

Lietz, J. G., Novario, S., Jansen, G. R., Hagen, G., and Hjorth-Jensen, M. (2017). Computational nuclear physics and post hartree-fock methods. *Lecture Notes in Physics*, page 293–399. 81, 88

Lin, C., Zong, F. H., and Ceperley, D. M. (2001). Twist-averaged boundary conditions in continuum quantum monte carlo algorithms. *Phys. Rev. E*, 64:016702. 88

Lu, H.-H., Klco, N., Lukens, J. M., Morris, T. D., Bansal, A., Ekström, A., Hagen, G., Papenbrock, T., Weiner, A. M., Savage, M. J., and Lougovski, P. (2019). Simulations of subatomic many-body physics on a quantum frequency processor. *Physical Review A*, 100(1). 4

Macridin, A., Spentzouris, P., Amundson, J., and Harnik, R. (2018). Electron-phonon systems on a universal quantum computer. *Phys. Rev. Lett.*, 121:110504. 4

Masanes, L. (2009). Area law for the entropy of low-energy states. *Phys. Rev. A*, 80:052104. 10

Maslov, D., Kim, J.-S., Bravyi, S., Yoder, T. J., and Sheldon, S. (2021). Quantum advantage for computations with limited space. *Nature Physics*, 17(8):894–897. 4

McArdle, S., Endo, S., Aspuru-Guzik, A., Benjamin, S. C., and Yuan, X. (2020). Quantum computational chemistry. *Rev. Mod. Phys.*, 92(1):015003. 4

Modi, K., Paterek, T., Son, W., Vedral, V., and Williamson, M. (2010). Unified view of quantum and classical correlations. *Phys. Rev. Lett.*, 104:080501. 8

Müller-Lennert, M., Dupuis, F., Szehr, O., Fehr, S., and Tomamichel, M. (2013). On quantum rényi entropies: A new generalization and some properties. *Journal of Mathematical Physics*, 54(12). 9

Nielsen, M. and Chuang, I. (2010). *Quantum Computation and Quantum Information: 10th Anniversary Edition*. Cambridge University Press. 5

O'Malley, P. J. J., Babbush, R., Kivlichan, I. D., Romero, J., McClean, J. R., Barends, R., Kelly, J., Roushan, P., Tranter, A., Ding, N., Campbell, B., Chen, Y., Chen, Z., Chiaro,

B., Dunsworth, A., Fowler, A. G., Jeffrey, E., Lucero, E., Megrant, A., Mutus, J. Y., Neeley, M., Neill, C., Quintana, C., Sank, D., Vainsencher, A., Wenner, J., White, T. C., Coveney, P. V., Love, P. J., Neven, H., Aspuru-Guzik, A., and Martinis, J. M. (2016). Scalable quantum simulation of molecular energies. *Phys. Rev. X*, 6:031007. 4

Ortiz, G., Gubernatis, J. E., Knill, E., and Laflamme, R. (2001). Quantum algorithms for fermionic simulations. *Phys. Rev. A*, 64:022319. 6

Ovrum, E. and Hjorth-Jensen, M. (2007). Quantum computation algorithm for many-body studies. 6

Pazy, E. (2023). Entanglement entropy between short range correlations and the fermi sea in nuclear structure. *Phys. Rev. C*, 107:054308. 11, 72

Plenio, M. B., Eisert, J., Dreißig, J., and Cramer, M. (2005). Entropy, entanglement, and area: Analytical results for harmonic lattice systems. *Phys. Rev. Lett.*, 94:060503. 10

Preskill, J. (2012). Quantum computing and the entanglement frontier. 4

Preskill, J. (2018). Quantum Computing in the NISQ era and beyond. *ArXiv e-prints*. 4

Preskill, J. (2021). Quantum computing 40 years later. 4

Pérez-Obiol, A., Romero, A. M., Menéndez, J., Rios, A., García-Sáez, A., and Juliá-Díaz, B. (2023). Nuclear shell-model simulation in digital quantum computers. *Scientific Reports*, 13(1). 4

Qiskit contributors (2023). Qiskit: An open-source framework for quantum computing. 7, 14

Rényi, A. (1961). On measures of entropy and information. In Neyman, J., editor, *Proceedings of the Fourth Berkeley Symposium on Mathematical Statistics and Probability, Volume 1: Contributions to the Theory of Statistics*, Proceedings of the Berkeley Symposium on Mathematical Statistics and Probability, pages 547–561, Berkeley, CA. University of California Press. 9

Robin, C., Savage, M. J., and Pillet, N. (2021). Entanglement rearrangement in self-consistent nuclear structure calculations. *Phys. Rev. C*, 103:034325. 10, 71

Roggero, A. and Carlson, J. (2019). Dynamic linear response quantum algorithm. *Phys. Rev. C*, 100:034610. 4, 13

Roggero, A., Gu, C., Baroni, A., and Papenbrock, T. (2020a). Preparation of excited states for nuclear dynamics on a quantum computer. *Phys. Rev. C*, 102:064624. x, xi, 4, 11, 13, 15, 18, 20, 21, 38, 39, 40, 41, 45, 46, 47, 59, 61, 116

Roggero, A., Li, A. C. Y., Carlson, J., Gupta, R., and Perdue, G. N. (2020b). Quantum computing for neutrino-nucleus scattering. *Phys. Rev. D*, 101:074038. 4

Schrödinger, E. (1935). Die gegenwärtige Situation in der Quantenmechanik. *Naturwissenschaften*, 23(48):807–812. 7

Setia, K., Bravyi, S., Mezzacapo, A., and Whitfield, J. D. (2019). Superfast encodings for fermionic quantum simulation. *Phys. Rev. Res.*, 1:033033. 5

Shavitt, I. and Bartlett, R. J. (2009). *Many-body Methods in Chemistry and Physics*. Cambridge University Press, Cambridge UK. 64, 67, 69, 70

Shehab, O., Landsman, K., Nam, Y., Zhu, D., Linke, N. M., Keesan, M., Pooser, R. C., and Monroe, C. (2019). Toward convergence of effective-field-theory simulations on digital quantum computers. *Phys. Rev. A*, 100:062319. 4

Shende, V. V. and Markov, I. L. (2009). On the cnot-cost of toffoli gates. *Quantum Info. Comput.*, 9(5):461–486. 33

Somma, R., Ortiz, G., Gubernatis, J. E., Knill, E., and Laflamme, R. (2002). Simulating physical phenomena by quantum networks. *Physical Review A*, 65(4). 6

Stein, C. J. and Reiher, M. (2016). Automated selection of active orbital spaces. *Journal of Chemical Theory and Computation*, 12(4):1760–1771. 9

Stein, C. J. and Reiher, M. (2017). Measuring multi-configurational character by orbital entanglement. *Molecular Physics*, 115(17–18):2110–2119. 9

Stetcu, I., Baroni, A., and Carlson, J. (2022). Variational approaches to constructing the many-body nuclear ground state for quantum computing. *Physical Review C*, 105(6). 4

Steudtner, M. and Wehner, S. (2019). Quantum codes for quantum simulation of fermions on a square lattice of qubits. *Phys. Rev. A*, 99:022308. 5

Subramanian, S. and Hsieh, M.-H. (2021). Quantum algorithm for estimating α-renyi entropies of quantum states. *Physical Review A*, 104(2). 78

Sun, Z. H., Morris, T. D., Hagen, G., Jansen, G. R., and Papenbrock, T. (2018). Shell-model coupled-cluster method for open-shell nuclei. *Phys. Rev. C*, 98:054320. 64

Szalay, S., Pfeffer, M., Murg, V., Barcza, G., Verstraete, F., Schneider, R., and Legeza, Ö. (2015). Tensor product methods and entanglement optimization for ab initio quantum chemistry. *International Journal of Quantum Chemistry*, 115(19):1342–1391. 9

T. Papenbrock (2018). The coupled cluster method. https://nucleartalent.github.io/ManyBody2018/doc/pub/CCM/html/CCM.html. Accessed: 2023-02-06. 81, 88

Temme, K., Bravyi, S., and Gambetta, J. M. (2017). Error mitigation for short-depth quantum circuits. *Phys. Rev. Lett.*, 119:180509. 7, 117

Terashima, H. and Ueda, M. (2005). Nonunitary quantum circuit. *International Journal of Quantum Information*, 03(04):633–647. 14

Thompson, D. R., Lemere, M., and Tang, Y. C. (1977). Systematic investigation of scattering problems with the resonating-group method. *Nucl. Phys. A*, 286:53–66. 85

Thouless, D. J. (1960). Stability conditions and nuclear rotations in the Hartree-Fock theory. *Nuclear Physics*, 21:225–232. 68

Tichai, A., Knecht, S., Kruppa, A. T., Legeza, Ö., Moca, C. P., Schwenk, A., Werner, M. A., and Zarand, G. (2022). Combining the in-medium similarity renormalization group with the density matrix renormalization group: Shell structure and information entropy. 10

Van den Nest, M. (2013). Universal quantum computation with little entanglement. *Physical Review Letters*, 110(6). 8

Van den Nest, M., Dür, W., Vidal, G., and Briegel, H. J. (2007). Classical simulation versus universality in measurement-based quantum computation. *Physical Review A*, 75(1). 8

Vatan, F. and Williams, C. (2004). Optimal quantum circuits for general two-qubit gates. *Physical Review A*, 69(3). 30

Vidal, G. (2003). Efficient classical simulation of slightly entangled quantum computations. *Physical Review Letters*, 91(14). 8

Weinberg, S. (1979). Phenomenological lagrangians. *Physica A: Statistical Mechanics and its Applications*, 96(1):327 – 340. 2

Whitfield, J. D., Havlíček, V. c. v., and Troyer, M. (2016). Local spin operators for fermion simulations. *Phys. Rev. A*, 94:030301. 5

Wilson, K. G. (1975). The renormalization group: Critical phenomena and the kondo problem. *Rev. Mod. Phys.*, 47:773–840. 1

Wolf, M. M. (2006). Violation of the entropic area law for fermions. *Phys. Rev. Lett.*, 96:010404. 10

Zeng, B., Chen, X., Zhou, D., and Wen, X.-G. (2015). Quantum information meets quantum matter. *Quantum Science and Technology*. 9

Zhang, D.-B., Xing, H., Yan, H., Wang, E., and Zhu, S.-L. (2021). Selected topics of quantum computing for nuclear physics*. *Chinese Physics B*, 30(2):020306. 4

Appendices

A Convention of Gates

This section briefly introduces the conventions of the quantum gates used in Chapter 2.

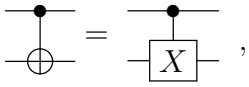
I utilize the one-qubit quantum gates X, Y and Z to represent the Pauli matrices σ_x, σ_y and σ_z respectively. The one qubit rotation gates R_x, R_y and R_z are defined as

$$\begin{aligned} R_x(\phi) \equiv e^{-i\frac{\phi}{2}X} &= \begin{pmatrix} \cos(\phi/2) & -i\sin(\phi/2) \\ -i\sin(\phi/2) & \cos(\phi/2) \end{pmatrix}, \\ R_y(\phi) \equiv e^{-i\frac{\phi}{2}Y} &= \begin{pmatrix} \cos(\phi/2) & -\sin(\phi/2) \\ \sin(\phi/2) & \cos(\phi/2) \end{pmatrix}, \\ R_z(\phi) \equiv e^{-i\frac{\phi}{2}Z} &= \begin{pmatrix} e^{-i\phi/2} & 0 \\ 0 & e^{i\phi/2} \end{pmatrix}. \end{aligned} \tag{A.1}$$

The Hadamard gate, denoted with H, is defined as

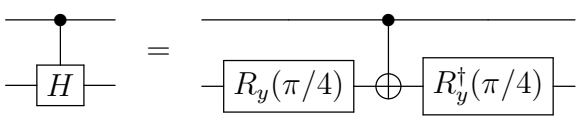
$$H = \frac{1}{\sqrt{2}} \begin{pmatrix} 1 & 1 \\ 1 & -1 \end{pmatrix}. \tag{A.2}$$

There are frequently used controlled single-qubit gates (two-qubit gates): CNOT (controlled-X), CZ (controlled-Z), and CH (controlled-H). The CNOT gate is defined as



(A.3)

with the symbol in the first line as a solid circle. Here and in what follows, a solid circle in the ancilla qubit means the target system is controlled by state $|1\rangle$; a hollow circle means the target system is controlled by state $|0\rangle$. The CH gate and its decomposition are defined as

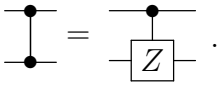


(A.4)

where I use the identity

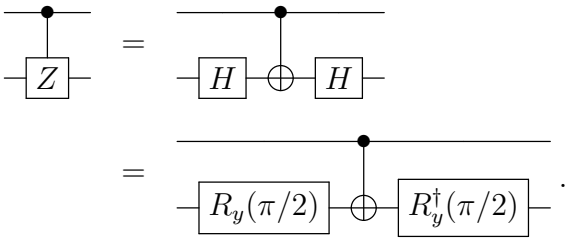
$$H = XR_y(\pi/2) = R_y^\dagger(\pi/4)XR_y(\pi/4)\ , \tag{A.5}$$

and it only requires a single CNOT gate. The CZ gate is defined as



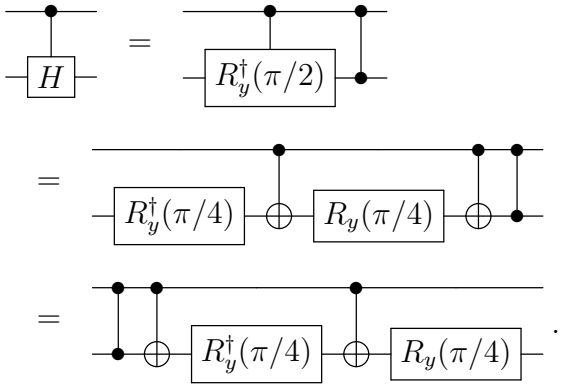
(A.6)

Its decomposition to CNOT is defined as



(A.7)

Here, I use the identity $HZH = X$ and use Eq. (A.5) in the second line. With Eq. (A.7) and the identity $H = ZR_y^\dagger(\pi/2)$, other decompositions for CH gate are available



(A.8)

The SWAP gate is used to change the states of two qubits. It is represented by the symbol



(A.9)

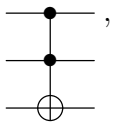
and described by the following unitary matrix

$$\text{SWAP} = \begin{pmatrix} 1 & 0 & 0 & 0 \\ 0 & 0 & 1 & 0 \\ 0 & 1 & 0 & 0 \\ 0 & 0 & 0 & 1 \end{pmatrix} , \tag{A.10}$$

and can be decomposed into

$$\text{SWAP} = \frac{\mathbb{I} \otimes \mathbb{I} + X \otimes X + Y \otimes Y + Z \otimes Z}{2} . \tag{A.11}$$

The Toffoli (CCNOT) gate, which is a three-qubit gate, is depicted as

 , (A.12)

and compactly expressed as the following unitary matrix

$$T = \begin{pmatrix} \mathbb{I} & 0 & 0 & 0 \\ 0 & \mathbb{I} & 0 & 0 \\ 0 & 0 & \mathbb{I} & 0 \\ 0 & 0 & 0 & X \end{pmatrix} , \tag{A.13}$$

and decomposed into a linear combination

$$T \;\; = \;\; (\mathbb{I} - |11\rangle \langle 11|) \otimes \mathbb{I} + |11\rangle \langle 11| \otimes X \; . \tag{A.14}$$

B Error Mitigation

This section briefly introduces the error mitigation procedures I employed in Chapter 2. For more detailed information, I refer the readers to Appendix H of Ref. (Roggero et al., 2020a). Two types of error mitigation procedures are employed: (i) readout error mitigation on the measured distributions, and (ii) zero-noise extrapolation aims to correct gate noise.

First, I review the readout-error correction scheme (see also (Kandala et al., 2017)). For each single qubit, one could design experiments and obtain the calibration matrix

$$P = \begin{pmatrix} 1-e_0 & e_1 \\ e_0 & 1-e_1 \end{pmatrix} , \tag{B.1}$$

where the parameter e_0 (e_1) are defined as the probability to wrongly measure $|1\rangle$ ($|0\rangle$) when preparing $|0\rangle$ ($|1\rangle$), respectively. The parameters e_0 and e_1 are zero in the limit of no noise, and the calibration matrix is identity.

For n qubits, in principle, one needs to perform at least 2^n measurements to build the calibration matrix. Assume that readout errors are independent for different qubits. In that case, the calibration matrix is represented as a matrix with n diagonal 2×2 blocks, and the cost of measurements can be reduced to only $2n$. For each qubit, a read-out error mitigated result $\mathbf{p} = (\mathbf{p}, \mathbf{1} - \mathbf{p})$ is obtained as

$$\mathbf{p} = P^{-1} \cdot \mathbf{p}_e \, . \tag{B.2}$$

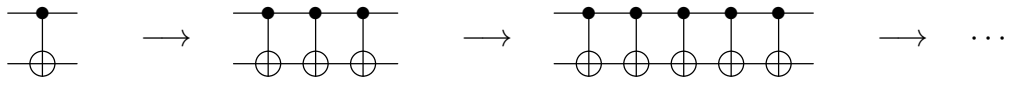
Here, $\mathbf{p}$ is the probability vector without read-out error, and $\mathbf{p}_e = (p_e, 1 - p_e)$ is the corresponding probabilities with read-out errors. The vector $\mathbf{p}_e$ is what one gets from the measurement of experiments. The inverse of the calibration matrix is

$$P^{-1} = \frac{1}{d} \begin{pmatrix} 1-e_1 & -e_1 \\ -e_0 & 1-e_0 \end{pmatrix} , \tag{B.3}$$

with $d = 1 - e_0 - e_1$.

Next, I review the approaches utilized for zero-noise extrapolation. More information can be found in Ref. (Dumitrescu et al., 2018; Li and Benjamin, 2017; Endo et al., 2018). The zero-noise extrapolation consists of two steps. First, circuits with different noise levels are implemented, and the corresponding data is collected. Second, a noise-free estimator is extracted by using a parametrization of the noise corresponding to the noise levels. The parametrization approaches consist: (i) Richardson extrapolation (Temme et al., 2017), which expands the observable as a power series in the noise, (ii) polynomial extrapolation (Li and Benjamin, 2017; Dumitrescu et al., 2018), which performs a polynomial fit, and (iii) exponential extrapolation, which utilize a simple two-point exponential fit.

Assume that the two-qubit gates, like CNOT, are the primary noise resources. To obtain results at higher noise levels, we design a series of circuits by adding pairs (the product of two CNOTs is the identity) of redundant CNOT gates for every CNOT in the original circuit:



$k = 1$ $k = 2$ $k = 3$

where k indicates the noise levels. For kth circuit, the total number of CNOT is $N_C(k) = (2k-1)N_C(1)$.

For every circuit, the observables and errors are obtained after running on the quantum devices and denoted as (O_k, E_k). O_F is denoted as the error-free extrapolate expectation value. When every CNOT gates have a failure probability p_ε, the effective failure probability will grow linearly with k, the error will grow as $\epsilon = N_C(k)p_\varepsilon$ (with Richardson extrapolation method as an example).

The observable O is expanded as a power series (or others for different extrapolation methods) in error ϵ

$$O(\epsilon) = O_F + \sum_{j=1}^{M} c_j \epsilon^j + \mathcal{O}\left(\epsilon^{M+1}\right) \ .$$

For an experiment with fixed M and k, the error-free observable O_F is obtained by inverting the polynomial expression.

Vita

Chenyi Gu was born and brought up in Zhejiang Province, China. In 2013, she attended the Ocean University of China and received a Bachelor of Science in Physics in 2017. She began her PhD journey at the University of Tennessee, Knoxville (UTK) in August 2017, joined Dr. Thomas Papenbrock's theoretical nuclear physics group in 2019, and earned her Doctor of Philosophy in physics and minor in computational science in August 2024.